

University of Kentucky

UKnowledge

Theses and Dissertations--Chemistry

Chemistry


2017

ARSENIC REMOVAL WITH A DITHIOL LIGAND SUPPORTED ON MAGNETIC NANOPARTICLES

John Hamilton Walrod II

University of Kentucky, johnwalrod@uky.edu

Author ORCID Identifier:

 <https://orcid.org/0000-0003-1875-6546>

Digital Object Identifier: <https://doi.org/10.13023/ETD.2017.314>

[Right click to open a feedback form in a new tab to let us know how this document benefits you.](#)

Recommended Citation

Walrod, John Hamilton II, "ARSENIC REMOVAL WITH A DITHIOL LIGAND SUPPORTED ON MAGNETIC NANOPARTICLES" (2017). *Theses and Dissertations--Chemistry*. 83.
https://uknowledge.uky.edu/chemistry_etds/83

This Doctoral Dissertation is brought to you for free and open access by the Chemistry at UKnowledge. It has been accepted for inclusion in Theses and Dissertations--Chemistry by an authorized administrator of UKnowledge. For more information, please contact UKnowledge@lsv.uky.edu.

STUDENT AGREEMENT:

I represent that my thesis or dissertation and abstract are my original work. Proper attribution has been given to all outside sources. I understand that I am solely responsible for obtaining any needed copyright permissions. I have obtained needed written permission statement(s) from the owner(s) of each third-party copyrighted matter to be included in my work, allowing electronic distribution (if such use is not permitted by the fair use doctrine) which will be submitted to UKnowledge as Additional File.

I hereby grant to The University of Kentucky and its agents the irrevocable, non-exclusive, and royalty-free license to archive and make accessible my work in whole or in part in all forms of media, now or hereafter known. I agree that the document mentioned above may be made available immediately for worldwide access unless an embargo applies.

I retain all other ownership rights to the copyright of my work. I also retain the right to use in future works (such as articles or books) all or part of my work. I understand that I am free to register the copyright to my work.

REVIEW, APPROVAL AND ACCEPTANCE

The document mentioned above has been reviewed and accepted by the student's advisor, on behalf of the advisory committee, and by the Director of Graduate Studies (DGS), on behalf of the program; we verify that this is the final, approved version of the student's thesis including all changes required by the advisory committee. The undersigned agree to abide by the statements above.

John Hamilton Walrod II, Student

Dr. David A. Atwood, Major Professor

Dr. Mark A. Lovell, Director of Graduate Studies

ARSENIC REMOVAL WITH A DITHIOL LIGAND SUPPORTED ON MAGNETIC
NANOPARTICLES

Dissertation

A dissertation submitted in partial fulfillment of the
requirements for the degree of Doctor of Philosophy in the
College of Arts and Sciences
at the University of Kentucky

By

John Hamilton Walrod II

Lexington KY

Director: Dr. David A. Atwood, Professor of Chemistry

Lexington KY

2017

Copyright © John Hamilton Walrod 2017

ABSTRACT OF DISSERTATION

ARSENIC REMOVAL WITH A DITHIOL LIGAND SUPPORTED ON MAGNETIC NANOPARTICLES

Exposure to arsenic (As) in water, the ubiquitous toxin that poses adverse health risks to tens of millions, is the result of both anthropogenic and geochemical mobilization. Despite recent publicity and an increased public awareness, the dangers associated with arsenic exposure rank among the top priorities of public health agencies globally. Existing sequestration applications mainly include reductions and adsorption with zero-valent metals and their oxides. The performance of adsorption media is known to preferentially favor aqueous As(V) over As(III) due to the charge of the dissolved oxyanion. Magnetic nanoparticles (MNP) have been the focus of multidisciplinary research efforts for the removal of aqueous toxic metals and metalloids since they can be magnetically separated from the treated water. This improves isolation and allows for regeneration of the MNP, reducing cost and resource consumption. This research is focused on As(III & V) sequestration through the use of synthetic ligands N,N'-bis(2-mercaptoethyl)isophthalamide (abbreviated BDTH₂) and 2,2'-(isophthaloylbis(azanaediyl))bis-3-mercaptopropanoic acid (abbreviated ABDTH₂). Additionally, As(III) sequestration with ABDTH₂ functionalized on silica core-shell MNP (ABDTH₂ MNP), magnetite MNP (ABDTH₂@MNP), and commercial silica beads (ABDTH₂ Si60) is demonstrated. Both BDTH₂ and ABDTH₂ are effective precipitation agents for the removal of As(III) through the formation of S-As covalent bonds. ABDTH₂ MNP reduced a 200 ppb As(III) batch solution to below 10 ppb at pH 5, 7, and 9. Additionally, complete removal was achieved in the presence of anions at concentrations of 200, 500, and 1000 ppb. This system was evaluated for the removal of total arsenic from industrial solutions accumulated during the production of renewable biogas in landfills. Direct precipitation with BDTH₂ and ABDTH₂ was inhibited by the complex matrix. However, batch removal with ABDTH₂@MNP was effective in removing 82% of the inorganic arsenic. Sequestration of arsenic and speciation from these industrial solutions remains a challenge.

KEYWORDS: Arsenic Removal, Magnetic, Nanoparticles, Water Filtration, Chelation

John Hamilton Walrod II

Date: 7/28/2017

ARSENIC REMOVAL WITH A DITHIOL LIGAND SUPPORTED ON MAGNETIC
NANOPARTICLES

By

John Hamilton Walrod II

Dr. David A. Atwood

Director of Dissertation

Dr. Mark A. Lovell

Director of Graduate Studies

Date: 7/28/2017

ACKNOWLEDGEMENT

I would like to thank Dr. Atwood and group members for the experiences we shared in the lab. I am very grateful to the staff at Environmental Research Training Laboratories (ERTL), Dr. Gary Jacobs and Gerald Thomas at the Center for Applied Energy Research (CAER), Dr. Nadine Kabengi at Georgia State University, and Dr. DeLong and group members from the Physics Department at UK for technical assistance operating various analytical instruments.

I would also like to thank my parents, Dr. John Hamilton Walrod and Jane Walrod, for their endearing support. I will always cherish our late night phone calls about life. I would also like to thank my wife, Jennilee Walrod, and daughter, Emma Walrod. None of this would have been possible without their love and support.

TABLE OF CONTENTS

| | |
|---|------|
| ACKNOWLEDGEMENT | iii |
| LIST OF TABLES | ix |
| LIST OF SCHEMES..... | xi |
| LIST OF FIGURES | xiii |
| LIST OF ABBREVIATIONS AND SYMBOLS | xv |
| | |
| Chapter 1 Arsenic | 1 |
| 1.1 Arsenic Sulfur Chemistry | 1 |
| 1.2 Current Remediation | 10 |
| 1.3 Limitations of Sulfhydryl Based Strategies | 19 |
| 1.4 Conclusions | 21 |
| | |
| Chapter 2 BDTH ₂ and ABDTH ₂ : Dithiol Chelating Ligands | 21 |
| 2.1 Introduction | 21 |
| 2.2 Results and Discussion..... | 25 |
| 2.2.1 Synthesis and Characterization..... | 25 |
| 2.3 Experimental | 27 |
| 2.3.1 Reagents..... | 27 |
| 2.3.2 Analytical Techniques | 27 |
| 2.4 Synthesis..... | 28 |
| 2.4.1 BDTH ₂ Synthesis..... | 28 |
| 2.4.1.1 Charcterization..... | 28 |
| 2.4.2 ABDTH ₂ Synthesis..... | 28 |
| 2.4.2.1 Characterization | 29 |
| 2.5 Conclusions | 29 |
| | |
| Chapter 3 Aqueous Arsenite Precipitation with Dithiols BDTH ₂ and ABDTH ₂ | 30 |
| 3.1 Introduction | 30 |
| 3.1.1 BDTH ₂ and ABDTH ₂ Interactions with Aqueous Arsenite | 30 |
| 3.1.2 Arsenic Leaching and Soft Metal Preferences | 32 |

| | |
|---|----|
| 3.1.3 BDTH ₂ and ABDTH ₂ Arsenate Interactions | 33 |
| 3.2 Results and Discussion..... | 35 |
| 3.2.1 BDT-As(III) and ABDT-As(III)..... | 35 |
| 3.2.3 Arsenic Leaching and Soft Metal Preferences | 42 |
| 3.2.4 BDTH ₂ and ABDTH ₂ Arsenate Interactions | 44 |
| 3.3 Experimental | 46 |
| 3.3.1 Reagents..... | 46 |
| 3.3.2 Analytical Techniques | 47 |
| 3.4 Synthesis..... | 48 |
| 3.4.1 BDT-As(III) Synthesis (1.5X BDTH ₂) | 48 |
| 3.4.1.1 Characterization | 48 |
| 3.4.2 BDT-As(III) Synthesis (Excess As) | 48 |
| 3.4.2.1 Characterization | 48 |
| 3.4.3 ABDT-As(III) Synthesis (1.5X ABDTH ₂)..... | 49 |
| 3.4.3.1 Characterization | 49 |
| 3.4.4 ABDT-As(III) Synthesis (Excess As) | 49 |
| 3.4.4.1 Characterization | 50 |
| 3.4.5 BDT-As(III) and ABDT-As(III) Soft Metal Preference Leaching..... | 50 |
| 3.4.6 BDTH ₂ and ABDTH ₂ Arsenate Interactions | 50 |
| 3.5 Conclusions | 51 |
| | |
| Chapter 4 Synthesis of ABDTH ₂ Functionalized Silica Core-Shell Magnetite Nanoparticles | 52 |
| 4.1 Introduction | 52 |
| 4.1.1 Magnetite | 53 |
| 4.1.2 Silica Core-Shell Chemistry | 56 |
| 4.1.3 APTS Attachment to Silica..... | 60 |
| 4.1.4 Silanol Interaction with Chlorotrimethylsilane | 62 |
| 4.1.5 ABDT ₂ @MNPs | 64 |
| 4.2 Results and Discussion..... | 65 |
| 4.2.1 ABDTH ₂ Core-Shell MNPs..... | 65 |

| | |
|--|---------|
| 4.2.2 Surface Stabilized ABDTH ₂ @MNP..... | 86 |
| 4.2.3 Magnetic Properties of MNPs | 88 |
| 4.3 Experimental | 92 |
| 4.3.1 Reagents..... | 92 |
| 4.3.2 Analytical Techniques | 93 |
| 4.4 Synthesis..... | 94 |
| 4.4.1 Magnetite Nanoparticles..... | 94 |
| 4.4.1.1 Characterization | 94 |
| 4.4.2 Citrate Magnetic Nanoparticles | 95 |
| 4.4.2.1 Characterization | 95 |
| 4.4.3 Silica Core-Shell Nanoparticles..... | 95 |
| 4.4.3.1 Characterization | 96 |
| 4.4.4 APTS-SiO ₂ Magnetic Nanoparticles | 96 |
| 4.4.4.1 Characterization | 97 |
| 4.4.5 Si(CH ₃) ₃ -APTS-SiO ₂ Magnetite Nanoparticles..... | 97 |
| 4.4.5.1 Characterization | 98 |
| 4.4.6 Covalent Attachment of ABDTH ₂ | 98 |
| 4.4.6.1 Characterization | 98 |
| 4.4.7 Covalent Attachment of ABDTH ₂ (TMS) | 99 |
| 4.4.7.1 Characterization | 99 |
| 4.4.8 Ionic Attachment of ABDTH ₂ | 100 |
| 4.4.8.1 Characterization | 100 |
| 4.4.9 Surface Stabilized ABDTH ₂ Magnetite Nanoparticles | 100 |
| 4.4.9.1 Characterization | 101 |
| 4.5 Conclusions | 101 |
| Chapter 5 Arsenic Removal with ABDTH ₂ Magnetic Nanocomposite..... | 102 |
| 5.1 Introduction | 102 |
| 5.2 Results and Discussion..... | 104 |
| 5.2.1 Aqueous As(III) Removal with ABDTH ₂ , ABDTH ₂ (TMS), and i-ABDTH ₂ MNPs as a Function of pH | 104 |

| | |
|--|---------|
| 5.2.2 Aqueous As(III) Removal with Mixed Sodium Anions | 108 |
| 5.2.3 Removal of Other Forms of Arsenic with ABDTH ₂ @MNPs | 113 |
| 5.2.4 Arsenic Leaching from As-ABDT MNPs | 115 |
| 5.3 Experimental | 117 |
| 5.3.1 Reagents..... | 117 |
| 5.3.2 Analytical Techniques | 117 |
| 5.4 Synthesis..... | 118 |
| 5.4.1 Aqueous As(III) Removal as a Function of pH..... | 118 |
| 5.4.2 Aqueous As(III) Removal with Mixed Sodium Anions..... | 118 |
| 5.4.3 Removal of Other Forms of Arsenic with ABDTH ₂ @MNPs | 119 |
| 5.4.4 Arsenic Leaching from MNPs..... | 119 |
| 5.5 Conclusions | 119 |
| Chapter 6 Flow Cell Calorimetry of Silica Supported ABDTH ₂ | 120 |
| 6.1 Introduction | 120 |
| 6.2 Results and Discussion..... | 122 |
| 6.2.1 Synthesis and Characterization of ABDTH ₂ -Si60..... | 122 |
| 6.2.2 Flow Cell Calorimetry with ABDTH ₂ -Si60 with Arsenite | 125 |
| 6.3 Experimental | 127 |
| 6.3.1 Reagents..... | 127 |
| 6.3.2 Analytical Techniques | 128 |
| 6.4 Synthesis..... | 129 |
| 6.4.1-Si60..... | 129 |
| 6.4.1.1 Characterization | 129 |
| 6.4.2 APTS-Si60..... | 129 |
| 6.4.2.1 Characterization | 129 |
| 6.4.3 APTS-Si60 (TMS)..... | 129 |
| 6.4.3.1 Characterization | 130 |
| 6.4.4 ABTH ₂ -Si ionic | 130 |
| 6.4.4.1 Characterization | 130 |
| 6.4.5 ABDTH ₂ -Si covalent..... | 130 |

| | |
|---|-----|
| 6.4.5.1 Characterization | 131 |
| 6.5 Conclusions | 131 |
| | |
| Chapter 7 Removal of Aqueous Arsenic from Methane Gas Production | 131 |
| 7.1 Introduction | 131 |
| 7.2. Results and Discussion..... | 135 |
| 7.2.1 Arsenic Removal from Aqueous Condensate From Methane Gas Production | 135 |
| 7.2.2 Arsenic Removal from Redissolved Aqueous Condensate | 142 |
| 7.3 Experimental | 148 |
| 7.3.1 Reagents..... | 148 |
| 7.3.2 Analytical Techniques | 148 |
| 7.4 Synthesis..... | 149 |
| 7.4.1 Determination of Arsenic in Condensate Solutions | 149 |
| 7.4.2 Arsenic Removal from Condensate Solutions with BDTH ₂ and ABDTH ₂ | 149 |
| 7.4.3 Arsenic Removal from Condensate Solutions with BDTH ₂ and ABDTH ₂ as a Function of pH..... | 149 |
| 7.4.4 Arsenic Removal from Condensate Solutions with ABDTH@MNPs | 150 |
| 7.4.5 Arsenic Removal from Redissolved Condensate – Large Scale ABDTH ₂ @MNP | 150 |
| 7.4.6 Arsenic Removal from Cameron Solutions with ABDTH ₂ @MNPs..... | 150 |
| 7.5 Conclusions | 150 |
| | |
| Chapter 8 Conclusions | 151 |
| References..... | 155 |
| Vita..... | 179 |

LIST OF TABLES

| | |
|--|-----|
| Table 1.1 ATSDR substance priority list..... | 11 |
| Table 1.2 Common arsenic adsorption materials..... | 14 |
| Table 1.3 Recent developments of chemical precipitation agents for As(III) redrawn as published..... | 17 |
| Table 3.1 Various bidentate sulfhydryl redox properties..... | 34 |
| Table 3.2 Raman shift frequencies for BDT-As(III) | 41 |
| Table 3.3 ICP-OES results for BDT-As(III) leaching | 43 |
| Table 3.4 ICP-OES results for ABDT-As(III) leaching | 43 |
| Table 3.5 ICP-OES results for aqueous arsenate and 5X mol excess of BDTH ₂ and ABDTH ₂ | 45 |
| Table 3.6 IC results for the combinations of BDTH ₂ and ABDTH ₂ with As(V) | 45 |
| Table 4.1 Magnetic saturation values of various magnetic materials..... | 54 |
| Table 4.2 A comparison of core-shell thickness and M _S | 91 |
| Table 5.1 ICP-OES results for aqueous As(III) with ABDTH ₂ MNPs (TMS)..... | 105 |
| Table 5.2 ICP-OES results for aqueous As(III) with ABDTH ₂ MNPs..... | 105 |
| Table 5.3 ICP-OES results for aqueous As(III) with i-ABDTH ₂ MNPs | 106 |
| Table 5.4 ICP-OES results for aqueous As(III) with ABDTH ₂ @MNPs..... | 106 |
| Table 5.5 ICP-OES Results for As(III) removal with ABDTH ₂ MNPs and ABDTH ₂ @MNPs at different anionic concentrations..... | 109 |
| Table 5.6 ICP-OES results for As(III) removal with ABDTH ₂ MNPs at different anionic concentrations | 110 |

| | |
|--|-----|
| Table 5.7 ICP-OES Results for As(III) removal with i-ABDTH ₂ MNPs at different anionic concentrations | 111 |
| Table 5.8 ICP-OES results for the removal of DMA and mixed As(III/V) with ABDTH ₂ @MNPs | 113 |
| Table 5.9 ICP-OES results for As leaching with ABDTH ₂ MNPs, i-ABDTH ₂ MNPs, and ABDTH ₂ @MNPs | 116 |
| Table 7.1 Common arsenic compounds present in landfill methane gas production | 133 |
| Table 7.2 ICP-OES results for the BDTH ₂ batch results at pH 7..... | 137 |
| Table 7.3 ICP-OES results for total As removal with BDTH ₂ and ABTH ₂ as a function of pH (500 mol eq.; only the batch studies at pH 10 were run in triplicate)..... | 138 |
| Table 7.4 ICP-OES results for total As removal with ABDTH ₂ @MNPs | 140 |
| Table 7.5 Results for common anions in condensate tank 2..... | 141 |
| Table 7.6 ICP-OES results for other metals in condensate (concentrations listed as ppm; 300 mg ABDTH ₂ @MNPs)..... | 142 |
| Table 7.7 ICP-OES results for total arsenic..... | 143 |
| Table 7.8 ICP-OES results for the 1g scale cameron LF solution | 144 |

LIST OF SCHEMES

| | |
|---|----|
| Scheme 1.1 Equilibrium of the zwitter ion As(cys) ₃ under neutral (left) and basic (right) conditions | 4 |
| Scheme 1.2 Formation of [As(DTE) _x] | 6 |
| Scheme 1.3 Reduction of p-ethoxyphenylarsonic acid and sulfhydryl exchange with bidentate 1,2-ethanedithiol..... | 8 |
| Scheme 1.4 Arsenate formation of inner-sphere bidentate and monodentate on iron oxide | 13 |
| Scheme 1.5 Formation of DMSA coated magnetite nanoparticles (A) and BPLP containing cysteine (B) | 15 |
| Scheme 1.6 Oxidation products of 3-methylbut-2-ene-1-thiol and dimethylsulfane | 20 |
| Scheme 2.1 Synthesis of BDTH ₂ and ABDTH ₂ | 25 |
| Scheme 3.1 BDT-Hg(II) inertness towards other soft aqueous metals..... | 32 |
| Scheme 3.2 As(V) reduction to As(III) via thiol oxidation of Cys..... | 34 |
| Scheme 3.3 BDT-As(III) and ABDT-As(III) proposed network structures, SR = BDT and ABDT | 37 |
| Scheme 3.4 Base-mediated elimination of Cys to dehydroalanine (A) and potential arsenic sulfide formation with RS ₃ As(III) chelates while heating (B) | 39 |
| Scheme 4.1 Base-promoted sol-gel syntheses of alkoxysilanes: (A) hydrolysis (B) condensation | 57 |
| Scheme 4.2 Heat treatment of silica | 59 |
| Scheme 4.3 (A) APTS in water (B) APTS in dry organic solvent with hydrated silica... | 61 |
| Scheme 4.4 Flip mechanism for APTS..... | 62 |

| | |
|--|-----|
| Scheme 4.5 Chlorotrimethylsilane pathways: (A) silanol protection (B) polymerization (C) APTS interaction | 64 |
| Scheme 4.6 Reaction pathway for the synthesis of APTS MNPs..... | 73 |
| Scheme 4.7 Synthesis of ABDTH ₂ stabilized MNPs..... | 86 |
| Scheme 6.1 Ideal proposed structures with ABDTH ₂ -Si60..... | 125 |

LIST OF FIGURES

| | |
|--|-----|
| Figure 1.1 The proposed structure of the zwitterion form of $\text{As}(\text{GS})_3$ | 3 |
| Figure 1.2 Crystal structure of $\text{As}(\text{Hdt})$ | 5 |
| Figure 1.3 Crystal structure of 1,2-bis-dithiarsolan-2ylmercapto-ethane (left) and 2-iodo-1,3,2-dithiarsolane(right) | 7 |
| Figure 1.4 Crystal structure of four-coordinate $\text{As}(\text{L1-})$ | 9 |
| Figure 1.5 Structure of arsenoplatin-1 | 10 |
| Figure 2.1 Structure of the ligand design: BDTH ₂ , and ABDTH ₂ ⁸⁸ | 23 |
| Figure 2.2 Thermodynamic 14-membered ring product with potential divalent ions | 24 |
| Figure 3.1 Several potential products with bidentate sulfhydryl ligands with aqueous $\text{As}(\text{III})$ | 31 |
| Figure 3.2 Recent examples of S-As(V) bond formation | 34 |
| Figure 4.1 Different silica silanol groups | 58 |
| Figure 4.2 Seven membered APTS ring in aqueous solution | 61 |
| Figure 4.3 TEM images of uncoated magnetite nanoparticles | 67 |
| Figure 4.4 Silica core-shell images from raw MNPs | 70 |
| Figure 4.5 TEM images of silica core-shell MNP | 72 |
| Figure 4.6 Ideal surface composition for split-view structures of ABDTH ₂ , ABDTH ₂ (TMS), and i-ABDTH ₂ MNPs | 78 |
| Figure 4.7 Dispersed ABDTH ₂ MNPs and magnetically separated ABDTH ₂ MNPs using computer hard drive magnets | 88 |
| Figure 5.1 Optimal proposed split view of ABDTH ₂ MNPs after $\text{As}(\text{III})$ removal | 103 |
| Figure 5.2 Possible Interactions of $\text{As}(\text{III})$ and $\text{As}(\text{V})$ with ABDTH ₂ @MNPs ¹⁶⁵ | 115 |

| | |
|--|-----|
| Figure 7.1 Methane generation and renewable energy cycle..... | 132 |
| Figure 7.2 Stepwise Cameron process for treating H ₂ S from biogas | 134 |
| Figure 7.3 Unfiltered condensate water from the landfill methane production site | 136 |

LIST OF ABBREVIATIONS AND SYMBOLS

General:

| | |
|--------------------|--|
| Å | angstrom, 10^{-10} meters |
| ABDTH ₂ | 2,2'-(isophthaloylbis(azanediyl))bis(3-mercaptopropanoic acid) |
| APTS | 3-(aminopropyl)triethoxysilane |
| BDTH ₂ | 1,3-benzenediamidoethanethiol |
| BET | Brunauer-Emmett-Teller |
| cm | centimeter |
| Cys | cysteine |
| DHLA | dihydrolipoic acid |
| DI 18 MΩ | (mega-ohm) deionized water |
| DLS | dynamic light scattering |
| DMA | dimethylarsinic or cacodylic acid |
| DMSA | 2,3-dimercaptosuccinic acid |
| DSC | direct scanning calorimetry |
| DTE | dithioerythritol |
| DTT | dithiothreitol |
| EA | elemental analysis |
| EDC | N-(3-dimethylaminopropyl)-N'-ethylcarboiimide |
| emu | electromagnetic unit |
| ESI | electrospray ionization |
| EtOH | ethanol |
| g | grams |
| GSH | glutathione |

| | |
|---------|--|
| GSSG | oxidized glutathione |
| h | hours |
| Hz | Hertz, s ⁻¹ |
| ICP-OES | inductively coupled plasma optical emission spectroscopy |
| IR | infrared spectroscopy |
| IC | ionic chromatography |
| kJ | kilojoules |
| LCS | laboratory control sample |
| min | minute |
| mg | milligram |
| MMA | monomethylarsonic acid |
| MNP | magnetic nanoparticle |
| mmol | millimole |
| mL | milliliter |
| MP | melting point |
| MS | mass spectrometry |
| nm | nanometer |
| NMR | nuclear magnetic resonance |
| Oe | oersted |
| ppb | parts per billion |
| ppm | parts per million |
| s | seconds |
| Si-60 | commercial grade silica beads |
| SQUID | superconducting quantum interference device |
| t | time |

| | |
|-----|--|
| TEM | transmission electron microscope |
| THF | tetrahydrofuran, C ₄ H ₈ O |
| TGA | thermogravimetric analysis |
| TMS | chlorotrimethylsilane |

For infrared (IR) spectra:

| | |
|------------------|------------------|
| br | broad |
| cm ⁻¹ | wavenumbers |
| IR | Infrared Spectra |
| s | strong |
| vs | very strong |
| w | weak |

For nuclear magnetic resonance (NMR) spectra:

| | |
|---|--------------------------------------|
| δ | chemical shift, in parts per million |
| d | doublet |
| m | multiplet |
| q | quartet |
| s | single |

Chapter 1 Arsenic

1.1 Arsenic Sulfur Chemistry

There are numerous examples in nature that demonstrate the high binding affinity of sulfur (S) and arsenic (As). The S-As bond energy is $397.5 \text{ kJ mol}^{-1}$.¹ For example, several mineral forms of arsenic found naturally have the element bonded to sulfur as in realgar ($\alpha\text{-As}_4\text{S}_4$) and orpiment (As_2S_3).²⁻³ Aqueous mobilized inorganic arsenite, as $\text{As}(\text{OH})_3$ or As(III), from these natural sources is known as arsenous acid.³ Arsenous acid exists predominantly as $\text{As}(\text{OH})_3$ in acidic and moderately alkaline solutions. In aqueous solutions between pH 5-9 arsenous acid is oxidized to arsenic acid, H_3AsO_4 , at redox levels between 200-500 mV.⁴ The 1st pKa for $\text{As}(\text{OH})_3$ is 9.11, which is ironic given the toxicity of the element.⁵ Arsenous acid behaves more like a simple Brønsted acid.⁵ Higher substituted coordinate complexes with arsenous acid are rare.⁶⁻⁸ Similar ions with electronic configurations $nd^{10}(n+1)s^2(n+1)p^0$ adopt trigonal coordination geometries. Thus proposed bonding in arsenous acid with trigonal pyramidal geometries is comprised predominantly by electronic donation of ligands into the p orbitals of As(III).⁵ The weak Lewis acidity of the two s-electrons in arsenous acid react similar to a closed shell and are generally not involved in bond formation. Energetic stabilization of the 4s-electrons in As(III) is not due to relativistic effects that help explain the “inert pair effect” seen with heavier elements such as mercury or bismuth.⁹ The energetic stabilization results from the presence of the 3d row and shielding. However, arsenous acid is capable of both Lewis acidity and basicity.⁷

Arsenic is known to form structures with sulfhydryl compounds as $\text{As}(\text{SR})_3$, $\text{As}(\text{SR})_2\text{X}$, and $\text{As}(\text{SR})\text{X}_2$ which typically adopt trigonal pyramidal coordination

geometries.¹⁰⁻¹³ However, there are few reported single-crystal X-ray structures of $\text{As}(\text{OH})_3$ with small biologically significant molecules and derivatives in aqueous solutions. These molecules include the amino acids cysteine (Cys) and methionine (Met), and the antioxidants glutathione (GSH) and dihydrolipoic acid (DHLA).¹⁴ Recent structural database searches confirm the absence of structures. In comparison structures with these residues bound to proteins and enzymes with active site preference for $\text{As}(\text{III})$ are more common, but typically have lower coordination due to the steric constraint present in tertiary and quaternary structure.¹⁵⁻²¹ For example, the structure of an $\text{As}(\text{III})$ S-adenosylmethionine methyltransferase contained an $\text{As}(\text{III})$ atom with trigonal pyramidal geometry coordinated by two thiolates (S-As: 2.2 Å) from cysteine residues and a chloride anion.²² Additionally, there are numerous structural examples of organic molecules or ligands with S- $\text{As}(\text{III})$ bonds formed in anhydrous solvents starting from various $\text{As}(\text{III})$ alkyl and halide precursors.^{8, 23-25} For example, DHLA formed a bidentate cyclic complex when mixed with phenylarsonic acid in THF producing crystals suitable for X-ray analysis.²⁶ Due to the primary goal of this project, the predominant focus of this section is the review of S- $\text{As}(\text{III})$ interactions in aqueous solutions or aqueous mixtures such as EtOH- H_2O .

The metabolism of arsenic involves the redox cycle between $\text{As}(\text{III})$ and $\text{As}(\text{V})$ followed by methylation to mono-, di- and trimethylated derivatives.²⁷⁻³⁰ Biologically, GSH is the most notable example of intracellular bonding with $\text{As}(\text{III})$.³¹ GSH is a major component of the intracellular redox cycle and typically one of the more concentrated antioxidants (~5mM).³² The ratio of reduced GSH to oxidized GSSG is an indicator of oxidative stress. Complex formation with $\text{As}(\text{III})$ occurs through thioester bonds from

sulfhydryl groups present on the Cys residues on the ligand (Figure 1.1).^{11, 33-34} Also, GSH reduces As(V) to As(III) through the formation of the oxidized disulfide GSSG.³³ Additional GSH can then bond to the produced As(III). The single-crystal X-ray structure for the As(GS)₃ complex is not known with arsenous acid. GSH also formed a 1:2 complex with phenyldichloroarsine which suggests that sulfhydryl groups are inefficient substitution reactants with the C-As(III) bond in aqueous solution.³⁵ Furthermore, demethylation does not occur with GSH and mono- and dimethylarsinic in aqueous solution.³³ A more thorough review of sulfhydryl redox chemistry in aqueous solutions is included in section 1.3.

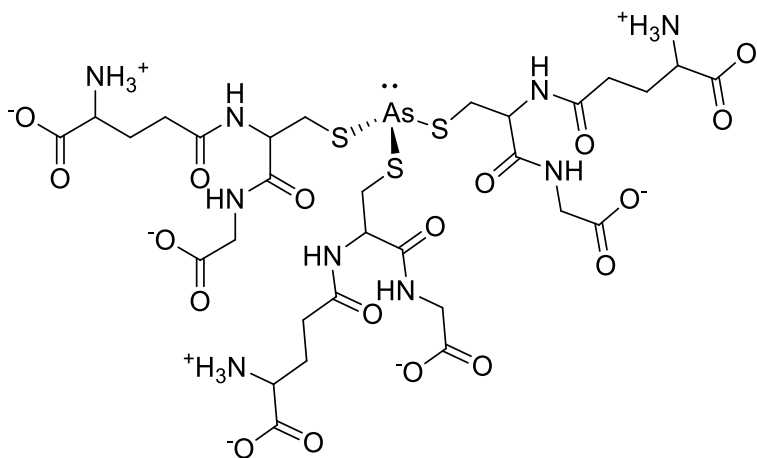
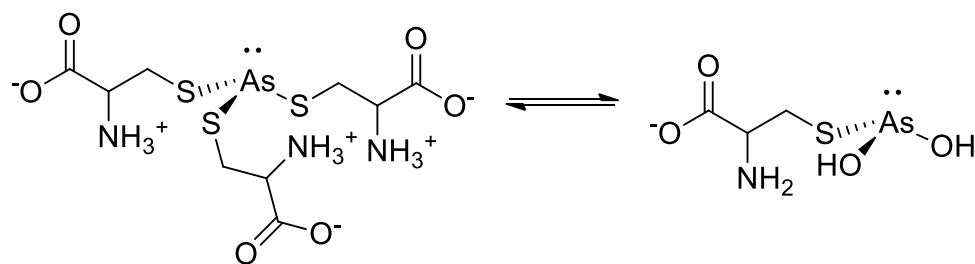


Figure 1.1 The proposed structure of the zwitterion form of As(GS)₃

The amino acid Cys also adopts the tris bonding arrangements with arsenous acid forming As(Cys)₃.³⁶ Both GSH and Cys complexes are dependent on pH.^{11,5} The formation constants measured by potentiometric and spectroscopic data reveal the following: As(Cys)₃, log K = 29.84(6); As(Cys)(OH)₂, log K = 12.01(9); As(GS)₃, log K = 32.0(6); and As(GS)(OH)₂, log K = 10(3).¹¹ In alkaline conditions, above pH 10,

hydroxide ions were capable of displacing the S-As(III) bond releasing free thiolate.¹¹ Scheme 1.1 shows the proposed structure from the reaction between Cys and As(OH)₃ and the equilibrium with pH.¹¹ Other derivatives characterized with coordination as As(Cys)(OH)₂ and As(GS)(OH)₂ in alkaline conditions support this equilibrium.^{5, 11} The combination of Cys and As(OH)₃ both in pH neutral solutions did not result in a pH change.¹¹ Proton dissociation does not precede attack by thiolate groups in the formation of As(Cys)₃. The coordination of sulfhydryl groups to As(III) occurred concomitantly with the sulfhydryl proton transfer to a hydroxyl group of the oxy acid forming a mole of water. Thus it has been proposed that the mechanism involves simultaneous As-S bond formation and elimination of water.¹¹ The lack of single-crystal X-ray structures of As(Cys)₃ may be due to the different polymeric phases, orthorhombic and monoclinic, of L-cysteine.³⁷ Additionally, extensive hydrogen bonding can lead to disordered networks of potential structures.



Scheme 1.1 Equilibrium of the zwitterion As(Cys)₃ under neutral (left) and basic (right) conditions¹¹

Arsenous acid also formed similar compounds when treated with the isomers dithioerythritol (DTE) and dithiothreitol (DTT) forming [As(H₃DTE)].^{5, 38} Figure 1.2 shows the resulting crystal structure. Here the ligand contains polydentate chelating atoms and can form bidentate and tridentate complexes as a function of pH.

Crystallographic data revealed the following bond distances and angles: As-S1, 2.2524(4) Å; As-S2, 2.2579(4) Å; As-O1, 1.8200(8) Å; S1-As-S2, 100.1 °; S1-As-O1, 90.1 °; S2-As-O1, 96.0 °; As-S1-C1, 94.5 °; As-S2-C4, 99.3 °. Displacement of the S-As(III) bond occurred with increased pH by either hydroxide or alkoxy groups. With excess ligand, dimerization and displacement of all oxy acid linkages to As(III) formed. Scheme 1.3 shows the resulting structures from the addition of excess ligand and arsenous acid.

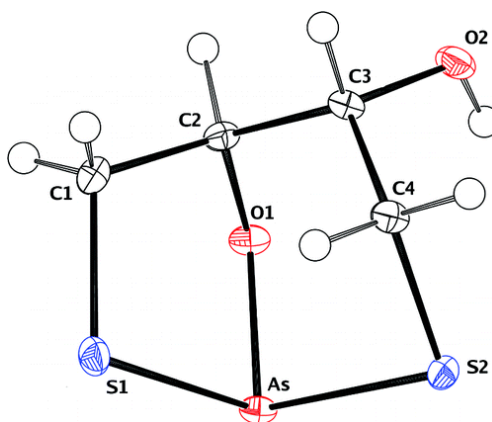
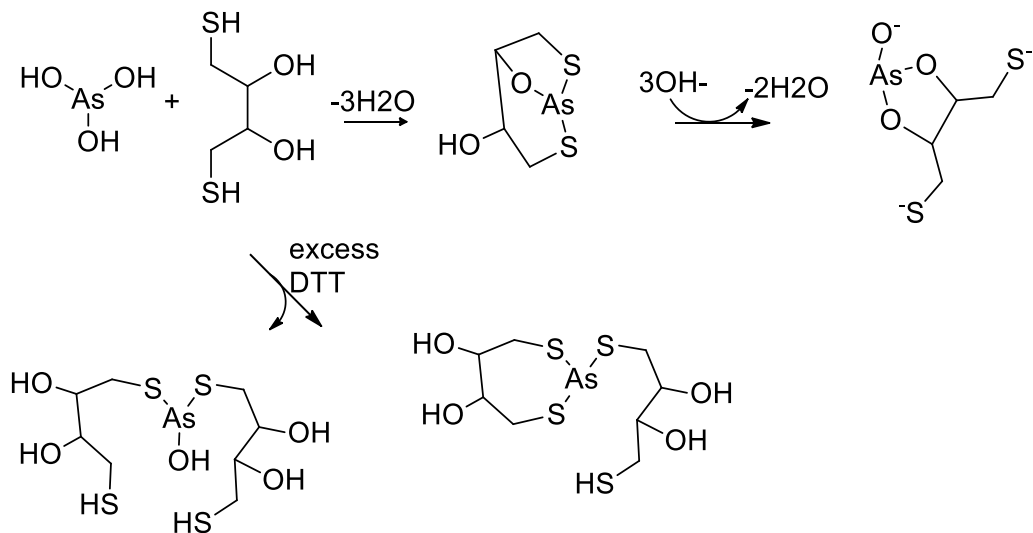


Figure 1.2 Crystal Structure of As(Hdt)

Reprinted with permission from Kolozsi, A.; Lakatos, A.; Galbács, G.; Madsen, A. Ø.; Larsen, E.; Gyurcsik, B., A pH-Metric, UV, NMR, and X-ray Crystallographic Study on Arsenous Acid Reacting with Dithioerythritol. *Inorg. Chem.* **2008**, 47 (9), 3832-3840. **d. Copyright 2017 American Chemical Society.**



Scheme 1.2 Formation of $[\text{As}(\text{DTE})_x]^{5, 13}$

Chelates with only bidentate sulfhydryl groups can also form mixtures of cyclic structures with As(III). For example, 1,2-ethanedithiol formed various monodentate and bidentate structures when mixed with different As(III) halides. These structures include the following: 2-chloro-1,3,2-dithiarsolane, 2-iodo-1,3,2-dithiarsolane, 2-chloro-1,3,2-dithiarsenane, 2-iodo-1,3,2-dithiarsenane.¹³ Here the S-As(III) bonds were relatively stable in acidic medium, but redistribution under basic conditions occurred similar to previous molecules containing S-As(III) bonds in aqueous solutions.^{5, 11} Dimeric structures formed by replacement of the axial halide with S-As(III) bonds linking the similar 5-membered ring structures. Figure 1.3 shows the crystal structure of 1,2-bis-dithiarsolan-2-ylmercapto-ethane and 2-iodo-1,3,2-dithiarsolane. The S-As(III) and S-C bond lengths for 1,2-bis-dithiarsolan-2-ylmercaptoethane compare similarly to other structures ranging from 2.23-2.26 Å and 1.81-1.84 Å, respectively. The S1-As1-S2, S2-As1-S3, and S1-As1-S3 bond angles in 1,2-bis-dithiarsolan-2-ylmercaptoethane were

93.24(6), 94.33(6), and 102.15(6) °. The I-As(III) bonds lengths in the complexes were longer, ranging from 2.6502-2.6036 Å.

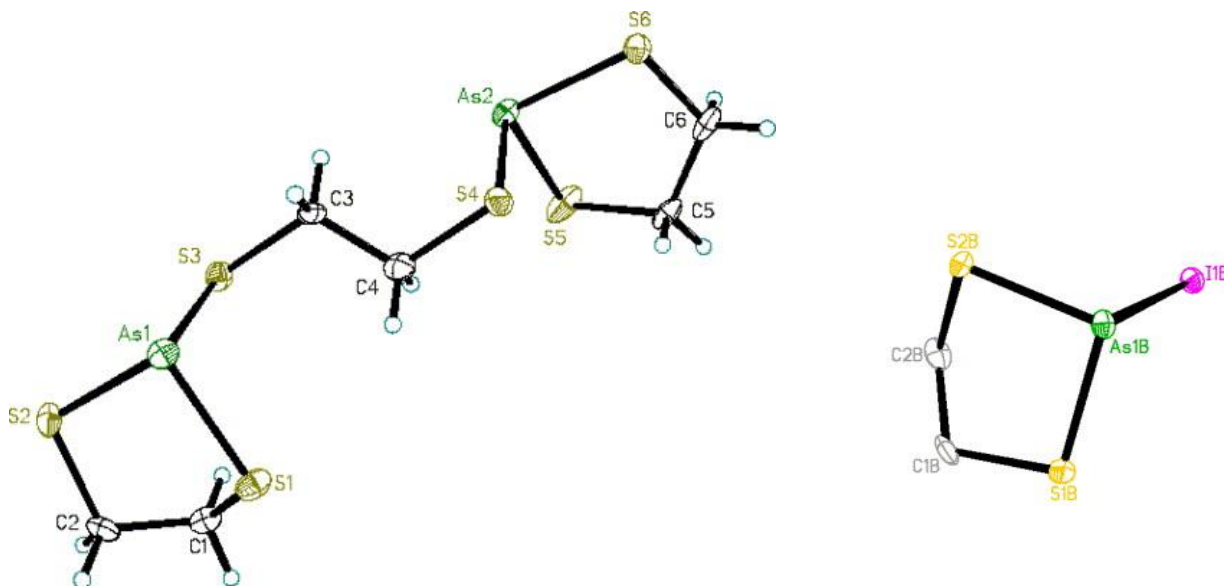
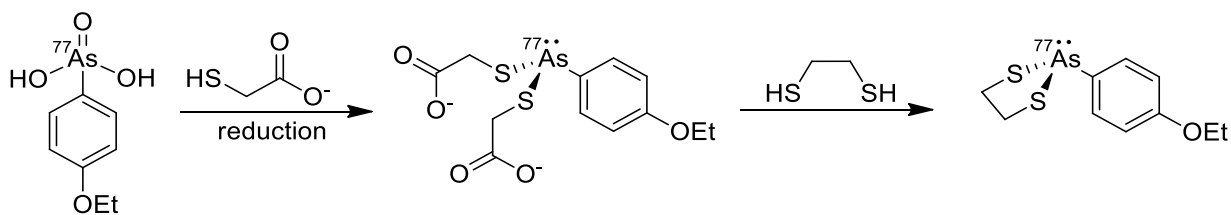


Figure 1.3 Crystal structure of 1,2-bis-dithiarsolan-2ylmercapto-ethane (left) and 2-iodo-1,3,2-dithiarsolane(right)

Reprinted with permission from Shaikh, T. A.; Bakus Ii, R. C.; Parkin, S.; Atwood, D. A., Structural characteristics of 2-halo-1,3,2-dithiarsenic compounds and tris-(pentafluorophenylthio)-arsen. *J. Organomet. Chem.* **2006**, 691 (9), 1825-1833, **with permission from Elsevier**

The S-As(III) bond is dynamic and reversible with other sulfhydryl atoms through exchange reactions.^{14, 34} For example, the bidentate sulfhydryl compounds DMSA and DTE displaced GSH from a (GS)₃As(III) complex. The GSH exchange was rapid (<1 min) and concomitantly resulted in oxidation to GSSG. The binding of As(III) with DMSA occurred through bidentate intramolecular, and a monodentate intermolecular coordination forming (DMSA)₃-[As₂].³⁴ These results highlight the preference of As(III)

for multidentate ligands compared to monothioles such as GSH. Interestingly, As(III) had a higher affinity for the vicinal sulfhydryl groups in DMSA compared to the bidentate sulfhydryl groups four carbons apart in DTE. Similarly, the bidentate 1,2-ethanedithiol displaced the monodentate mercaptoacetate groups in a radioactive dithioarylarsonic- $^{77}\text{As(III)}$ complex with trigonal pyramidal geometry.¹⁴ Here excess mercaptoacetate reduced the [^{77}As]arylarsonic acid with a concomitant bond formation which ultimately had less affinity for $^{77}\text{As(III)}$ than the bidentate ligand. Structures containing $^{77}\text{As(III)}$ are rare but may lead to potential use in radiopharmaceuticals. Structural data of the $^{77}\text{As(III)}$ complex with both 1,2-ethanedithiol and 1,3-ethanedithiol showed similar S-As(III) bond lengths (~ 2.2 Å) to other structures.⁵ The S-As-S bond angles, 92.62(3) and 100.95(6)°, were quite different for the 1,2 and 1,3-alkyl derivatives and both contained C-As(III) bonds measured at 1.961(2) and 1.958(6) Å, respectively.¹³



Scheme 1.3 Reduction of p-ethoxyphenylarsonic acid and sulfhydryl exchange with bidentate 1,2-ethanedithiol

Four-coordinate As(III) compounds are rare with molecules containing sulfhydryl groups.^{6, 24} For example As(III) formed a four-coordinate complex with the N,S-containing benzothiazoline ligand, (L1H)- 2-(pyridine-2-yl)-2,3-dihydrobenzothiazole.³⁹ Figure 1.4 displays two orientations of the crystal structures. The bond distances for this product were the following: As-I1, 2.737(2) Å; As-S1, 2.292(2) Å; As-N1, 1.846(5) Å;

As-N2, 2.411(6) Å. This four-coordinate As(III) complex is unique. The equatorial plane contained N1, I1, and the arsenic lone pair, with the axial positions as S1 and N2 atoms. This distorted trigonal bipyramidal structure with the two s-electrons in the equatorial plane is expected from VSEPR bond theory with a central element with ML₄E coordination.

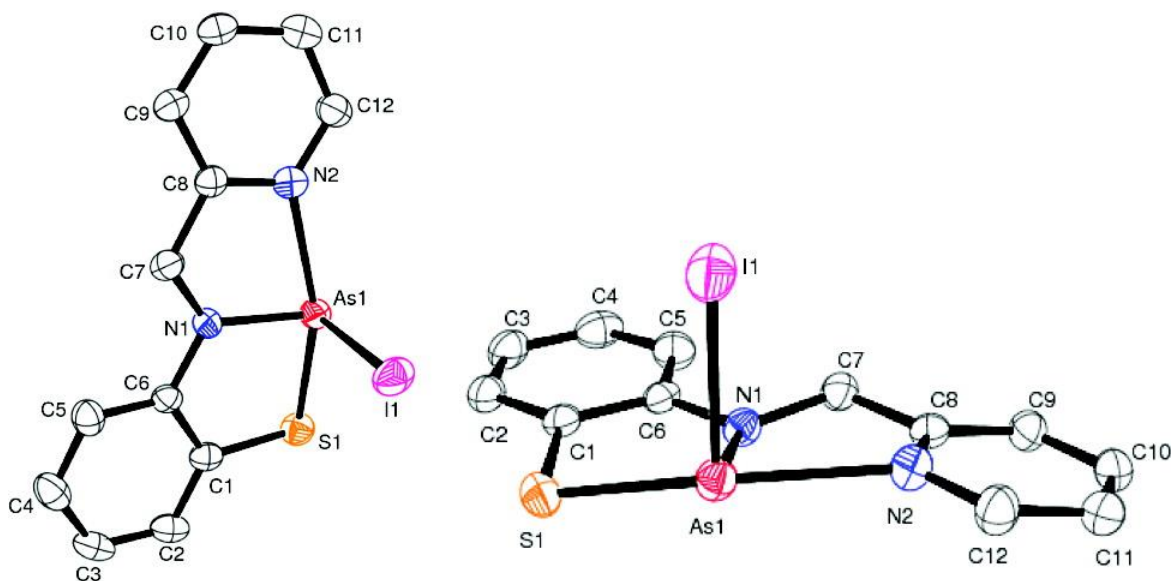


Figure 1.4 Crystal structure of four-coordinate As(L1-)

Reprinted with permission from Ezeh, V. C.; Patra, A. K.; Harrop, T. C., Four-Coordinate As^{III}-N,S Complexes: Synthesis, Structure, Properties, and Biological Relevance. *Inorg. Chem.* **2010**, *49* (6), 2586-2588. **Copyright 2017 American Chemical Society.**

There are other exotic examples of arsenous acid with more than three groups bound to As(III) that do not include sulfhydryl groups. Figure 1.5 shows a recent series of arsenoplatins that contained a five coordinate As(III) center with both Lewis acidity (O→As) and basicity (As →Pt).⁷ Arsenoplatins were formed by combining cis-platinum and arsenous acid in a water-nitrile mixture. The geometry of As(III) is a distorted trigonal

bipyramidal with a stable As(III)-Pt(II) bond (2.2687(4) Å). The equatorial plane contained Pt(II) and two hydroxy groups, and the axial plane contained alkoxides from propionitrile. The closest derivative of these arsenoplatins is found in a palladium complex formed with arsenous acid, $[\text{Mo}_3(\text{Pd}(\text{As}(\text{OH})_3)\text{-S}_4(\text{H}_2\text{O})_6\text{Cl}_3)_2\text{Cl}_2\cdot\text{C}_{36}\text{H}_{36}\text{N}_{24}\text{O}_{12}\cdot\text{H}_2\text{O}_{19}]$, with the lone pair of As(III) coordinating to Pd(II) (2.368(3) Å) with distorted tetrahedral geometry.⁴⁰ The coordination chemistry of arsenous acid is an underexplored area due in part to the lack of complexes suitable for X-ray characterization. For example, in 2013 there were only three complexes characterized by single-crystal X-ray containing $\text{As}(\text{OH})_3$ with Lewis basicity. Each of these complexes with arsenous acid formed by the reaction with a divalent metal ion.⁴¹

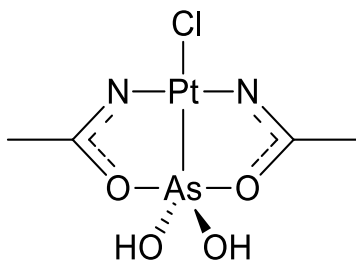


Figure 1.5 Structure of arsenoplatin-1

1.2 Current Remediation

Exposure to arsenic in drinking water, the ubiquitous toxin that poses adverse health risks to tens of millions, is the result of both anthropogenic and geochemical mobilization linked to skin, liver, lung, and bladder cancers. This systemic poisoning in humans is due to the interaction with DHLA, Cys residues, GSH, and S-adenosylmethionine (SAM) biomethylation pathways.^{11, 2-12} As(III) is the more toxic

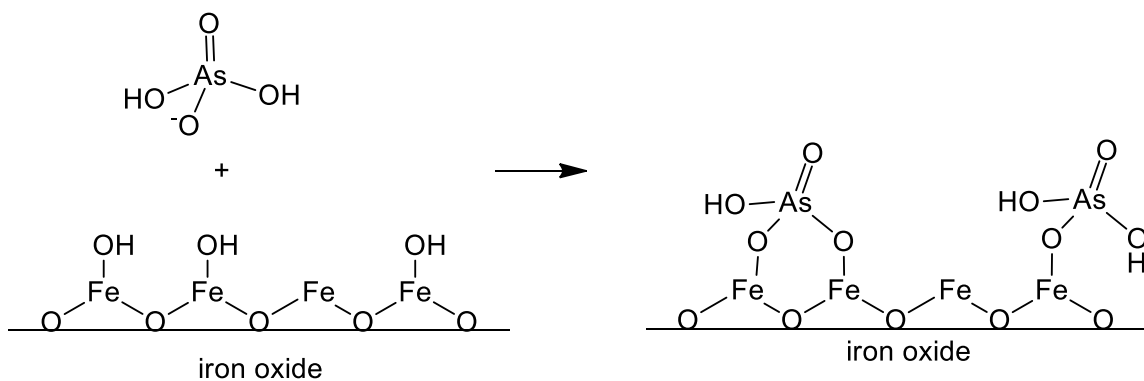
form of aqueous inorganic arsenic and is more difficult to capture with traditional sequestration technologies.² The toxicity of arsenic compounds follows the order: arsenite > arsenate > monomethylarsenic (MMA) > dimethylarsenic (DMA).⁴² However, there is some debate that trivalent methylarsenicals are more potent cytotoxicants than inorganic As(III).⁴³ Coincidentally methylation was proposed as a detoxification pathway due to the stability and inertness of trimethylarsine oxide. Table 1.1 lists the Agency for Toxic Substances and Disease Registry (ATSDR) 2015 substance priority list. The list includes a summation point system from the culmination of frequency, toxicity, and risk of human exposure to each element or chemical, and is not a list of the most toxic overall.

Table 1.1 ATSDR Substance Priority List

| 2015 Rank | Substance Name | Total Points | 2013 Rank |
|-----------|------------------------------|--------------|-----------|
| 1 | Arsenic | 1671.6 | 1 |
| 2 | Lead | 1529.4 | 2 |
| 3 | Mercury | 1458.6 | 3 |
| 4 | Vinyl Chloride | 1358.9 | 4 |
| 5 | Polychlorinated Biphenyls | 1345.1 | 5 |
| 6 | Benzene | 1327.6 | 6 |
| 7 | Cadmium | 1318.8 | 7 |

| | | | |
|----|-------------------------------------|--------|----|
| 8 | Benzo(A)Pyrene | 1304.4 | 8 |
| 9 | Polycyclic Aromatic Hydrocarbons | 1279.1 | 9 |
| 10 | Benzo(B)Fluoranthene | 1249.7 | 10 |

Arsenous acid commonly has a neutral charge in natural groundwater below pH 9, making it difficult to remove by ion-exchange filtration.³ In comparison arsenic acid is negatively charged at pH 7 ($pK_{a1} = 2.19$, $pK_{a2} = 6.94$, and $pK_{a3} = 11.5$). Ion-exchange is better for the removal of arsenate, but competition with other anions such as phosphates which have naturally high concentrations results in lower than desired results. Competition from various cations and anions will be further discussed in subsequent chapters. Examples of sequestration media include various iron oxides, activated carbon, silica, alumina, and other metal oxides that function primarily as adsorption media.^{42, 44-45} Adsorption has been the traditional approach for water treatment methods due to ease of operation and the sheer number of different materials with high adsorption performance.⁴⁶⁻⁴⁸ Removal can occur through both inner-sphere (chemisorption) and outer-sphere (physisorption) by ligand-exchange reactions and electrostatic or hydrogen bonding interactions, respectively.^{44, 47} For example, Scheme 1.4 shows arsenic acid is capable of both monodentate and bidentate complex formation at the surface of iron oxide.⁴⁹⁻⁵⁰



Scheme 1.4 Arsenate formation of inner-sphere bidentate and monodentate on iron oxide

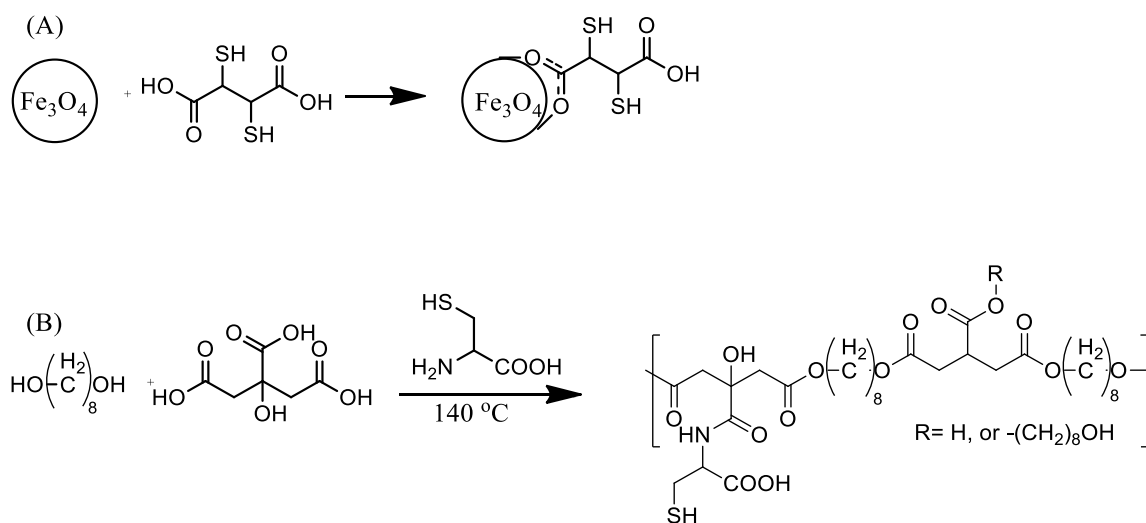
These materials are usually charge specific towards contaminants and are not capable of differentiating valence.⁴⁷ Interference in the capture of As(III) and As(V) by ions in solution is a common problem.⁵⁰⁻⁵¹ Also, leaching becomes a serious issue beyond equilibrium conditions. Unfortunately, the performance of adsorption media is far more efficient removing As(V) compared to As(III).⁵² As an example of the specific nature of traditional adsorbents, magnetite and activated carbon were more effective towards adsorption of As(V) compared to As(III).¹⁰ Additionally, arsenous acid was less tightly bound to aluminum hydroxides compared to As(V).⁵³ The combination of various oxides and adsorption materials is another option for arsenic removal. For example, composite iron matrix (CIM) adsorbents combined with sand, gravel, and charcoal are the active components in SONOS filters.⁵³ Similarly, Kanchan Arsenic FiltersTM contain various stages of brick chips, iron oxide, sand, and gravel that are cheap solutions for arsenic removal. However, these cheap solutions are not always effective remediation strategies for removing arsenic below safe levels from tube wells.⁵⁴ Table 1.2 lists various adsorbents and their loading capacities of As(III) and As(V).

Table 1.2 Common Arsenic Adsorption Materials

| Material | pH | Inorg. As | Initial Conc. (mg/L) | Dosage (Sorbent/Vol.) | Max. Removal (mg As / g sorb.) | Ref. |
|-------------------------------|-----------|------------------|--------------------------------|---------------------------------|--|-------------|
| Akagenéite | 7 | As(V) | 5-20 | 0.5 g/L | 120 | 55 |
| Alumina (meso.) | 5 | As(V) | 1500 | 0.1g/20mL | 121 | 56 |
| Carbon (black) | 4 | As(V) | 100 | 50mg/50L | 150-160 | 57 |
| Goethite | 9 | As(V) | 60 | 1.6g/L | 4 | 58 |
| Silica w/ Fe ⁺³ | 6 | As(V) | 1500 | 50mg/100mL | 120 | 59 |
| TiO ₂ | 7 | As(III) | 80 | 1g/L | 32.4 | 60 |
| Carbon w/ Fe ⁺³ | 7.85 | As(III) | 4.925 | 0.09g/30mL | 5.96 | 61 |
| Goethite | 9 | As(III) | 30 | 1.6g/L | 22 | 62 |
| Iron (Fe(O)OH) | 9 | As(III) | 20 | 1.6g/L | 28 | 62 |
| Fe ⁰ | 7 | As(III) | 0.15 | 20mg/20mL | 3.5 | 63 |

| | | | | | | |
|--------------------------------|---|---------|-------|-------|---|----|
| Fe ₃ O ₄ | 7 | As(III) | 0.500 | 1g/2L | 1 | 64 |
| (MNPs) | | | | | | |

Functionalized solid support media containing small alky sulfhydryl groups or derivatives can enhance the removal of As(III) and similar “soft” metals compared to bare oxides. Molecularly imprinted polymers and other hybrid media have gained attention for potential As(III) and As(V) removal applications that have been engineered with sulfhydryl groups to exploit the covalent S-As(III) bonding interactions.⁶⁵⁻⁷⁰ For example, Fe₃O₄ nanoparticles coated with DMSA and 3-(mercaptopropyl)triethoxysilane have high affinities for “soft” metals such as Hg(II).⁷¹⁻⁷³ Similarly, biodegradable photo-luminescent polymers (BPLP) containing cysteine are capable of aqueous removal of toxic metals and metalloids.⁷⁴ An example illustration of some of these materials is shown in Scheme 1.5.



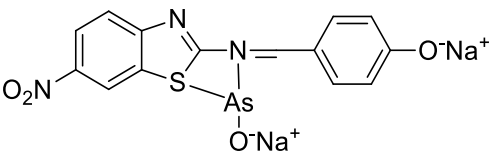
Scheme 1.5 Formation of DMSA coated magnetite nanoparticles (A) and BPLP containing cysteine (B)

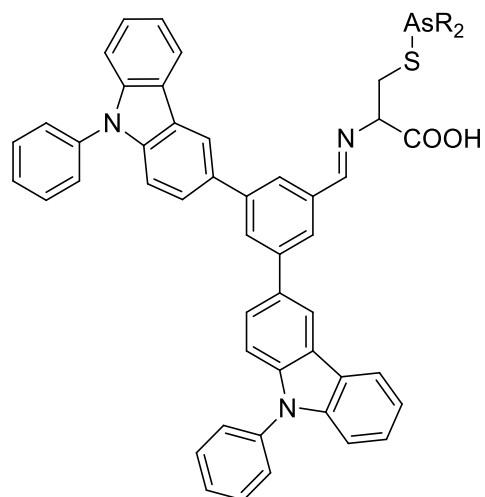
The oxidation of As(III) to As(V) is a pretreatment option for removing As(III) from contaminated groundwater. Co-precipitation or flocculation and filtration are necessary after oxidation. Natural oxidation of arsenite in surface water is typically a slow process without an additive oxidant such as ozone; the rate of As(III) to As(V) is $10^9 \text{ mol day}^{-1}$.² Electrochemical and high-energy processes (gamma radiation and ultraviolet) are effective for the oxidation. However, their long-term costs have shortcomings. Chemical oxidants include: chlorine (Cl_2), ozone, sodium hypochlorite (NaOCl), chlorine dioxide (ClO_2), potassium permanganate (KMnO_4), high-valence iron compounds (K_2FeO_4), and manganese oxides.⁷⁵⁻⁷⁶ Certain drawbacks exist for such chemical pretreatment oxidations. Chlorine is a good chemical oxidant of As(III) but produces a bad taste and odor of the resultant water. Potassium permanganate produces no adverse products but may discolor the water.

In contrast to the numerous examples of solid materials, examples of efficient precipitation chelates for aqueous As(III) containing organic ligands with sulfhydryl groups or other moieties are rare. The lack of reagents was the founding reason for investigating new compounds containing “soft” sulfhydryl groups in the Atwood group dating back nearly two decades. Table 1.3 shows recent examples of chemical precipitation chelates for aqueous As(III). Several new colorimetric and fluorescence-enhanced chemical precipitation reagents have been effective at As(III) sequestration. For example, a recent benzothiazole Schiff base colorimetric probe for aqueous As(III)/(V) performed efficiently at low ppb concentrations.⁷⁷ Here, coordination of both the S and N atom to As(III) resulted in a concentration-based probe. Similarly, a recent Schiff base with an intramolecular hydrogen bonding induced chelation-enhanced fluorescence probe

with cell permeability effectively bound As(III) at low ppb concentrations.⁷⁸ Also, an aggregation-induced emission (AIE) chromophore with increased optical properties resulting from binding to As(III) based on cysteine and carbazole efficiently flocculated with applied emission.⁷⁹ Excellent selective emission was observed even in the presence of various cations (Hg^{2+} , Pb^{2+} , Cd^{2+} , etc.) and various anions. However, the exact nature of selective As(III) binding enhancement emission is poorly understood, but the $\text{S}_3\text{As(III)}$ trigonal pyramidal structure likely enhances emission compared to the linear S-M-S bonds typical of divalent metal ions. Table 1.3 lists other recent cysteine derivatives and Schiff base chemical precipitation chelates with similar reactivity with As(III).

Table 1.3 Recent developments of chemical precipitation agents for As(III) redrawn as published

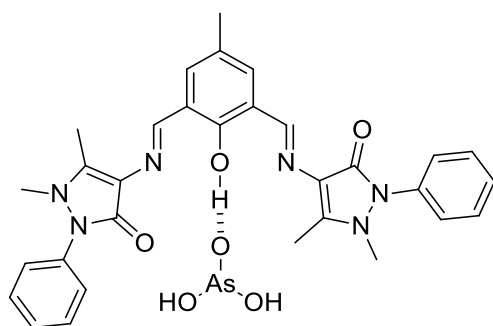
| Compound | As Species | Solvent | Ref. |
|---|---------------|----------------------|------|
|  | As(III)/As(V) | H_2O | 77 |



As(III)

H₂O/THF

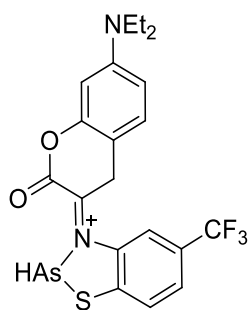
79



As(III)

H₂O

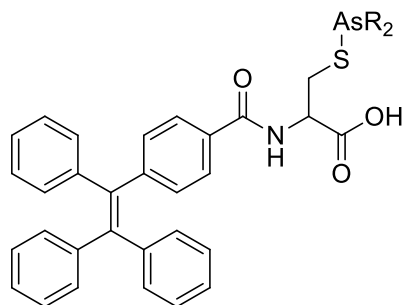
78



As(III)

H₂O/THF

39



As(III)

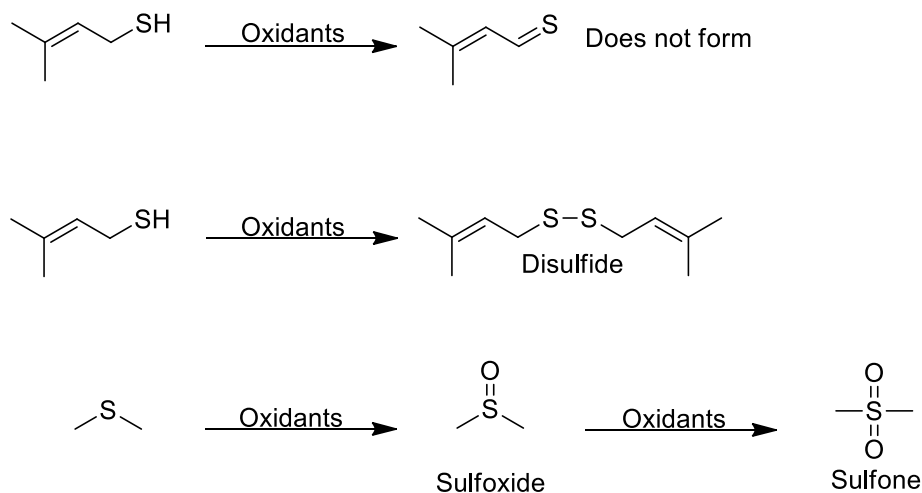
H₂O/THF

80

1.3 Limitations of Sulfhydryl-Based Strategies

Current organic functionalized materials aimed at the sequestration of aqueous arsenite typically employ sulfhydryl compounds. This is a selective treatment approach for “soft” ions in aqueous solution.⁷¹ However, several drawbacks limit sequestration from a technology that only relies on sulfhydryl reactivity.

There are many differences between alcohol and sulfhydryl functional groups regarding reactivity. Primary alcohols can oxidize to form aldehydes as RCOH. In comparison, the oxidation of primary sulfhydryl groups to thioaldehydes or thials, as RCSH, is rare due to increased reactivity making isolation difficult. Increased stability of thioaldehydes can be achieved by adding steric bulk, but natural oxidation in water is not the predominant product.⁸¹ Disulfide does form in natural oxidizing conditions; the S-S bond energy is 425.3 kJ mol⁻¹.⁸² This is a fundamental difference in reactivity compared to alcohols. Alcohol oxidation to the corresponding peroxide as ROOR is not normally observed. The S-S bond is twice as strong as the O-O bond in peroxides; the RO-OR bond energy is ~200 kJ mol⁻¹.⁸³ Additionally, oxidation to sulfenate (RSOH), sulfinate (RSO₂H), sulfoxide, and sulfonate (RSO₃H) derivatives are possible. For example, the disulfide bond was oxidized to sulfonates in the presence of Cu(II) ions in aerobic aqueous solution.⁸⁴ Here the oxidation of disulfide occurred through coordination of sulfur to Cu(II) followed by nucleophilic attack by an oxygen atom of water to the disulfide.⁸⁵ Scheme 1.5 shows examples of sulfhydryl oxidation products.



Scheme 1.6 Oxidation products of 3-methylbut-2-ene-1-thiol and dimethylsulfane

There are several different strategies to limit unwanted disulfide formation on solid materials containing grafted sulfhydryl groups. Low graft densities may lower intraparticle disulfide formation between sulfhydryl groups in the vicinity. The molecular geometry of the sulfhydryl ligand can be designed to restrict intramolecular disulfide formation.⁸⁶ However, interparticle or intermolecular formation can still produce linked disulfide in oxidizing conditions. Limiting applications with solutions in highly oxidizing conditions and avoiding long-term suspensions in solution may slow disulfide formation. Chemical reduction of disulfides is another pathway. For example, DTT is a powerful reducing agent of disulfides due to the stability of the oxidized cyclic six-membered ring. However, reducing agents are expensive. Finally, “soft” metal preferences with sulfhydryl applications can limit removal. A more thorough review of “soft” metal preferences is included in Chapter 3. These limitations are different from typical adsorption based removal strategies where generally ions having a greater charge at specific pH levels dominate binding. Importantly, these limitations from oxidation are

less of an issue in the areas where arsenous acid is most troublesome. The high concentrations of arsenous acid in wells located in southeast Asia typically occur in reducing aqueous solutions.⁸⁷

1.4 Conclusions

This research is focused on aqueous arsenite sequestration using a synthetic ligand based on a molecular architecture proven effective for chelating “soft” metal ions. The ligand should be capable of removing As(III) from aqueous solutions as a direct precipitation chelate and functionalized on solid supports. Direct chelation will be optimized by a detailed analysis of the reaction conditions. Also, the ligand will be linked to magnetite nanoparticles or MNPs, silica core-shell MNPs, and commercial grade silica beads. This research will explore synthetic routes for low-cost MNPs that possess small size distributions, high magnetization, and low environmental impact. Additionally, MNPs coated with thin layers of non-toxic silica, surface attached organosilanes, and the ligand using established literature procedures should allow for the removal of As(III). The performance of this system to remove As(III) will be investigated through aqueous batch and flow studies. The thermodynamics of arsenic removal and an industrial application removing arsenic from biogas solutions are detailed.

Chapter 2 BDTH₂ and ABDTH₂: Dithiol Chelating Ligands

2.1 Introduction

The design and synthesis of the bidentate sulfhydryl compound 2,2'-(isophthaloylbis(azanaediyl))bis(3-mercaptopropanoic acid), abbreviated as ABDTH₂,

was developed through a lineation of different bidentate sulfhydryl-containing molecules capable of forming covalent metal to sulfur bonds developed during the past two decades.⁸⁸⁻⁹⁴ Bidentate 2-aminoethanethiols have very high bimodal affinities towards both “soft” and “hard” ions with the sulfhydryl and amine groups, respectively.⁹⁵ Here, the sulfhydryl groups constitute the core functionality of the ligand forming “tweezer” like bidentate chelate modes through cyclization with “soft” ions such as Hg(II).⁸⁸ The acid-free analog abbreviated as BDTH₂, N,N'-bis(2-mercaptoethyl)isophthalamide, is an effective precipitation chelate. BDTH₂ forms covalent bonds with mercury, cadmium, lead, and selenium.^{93-94,96} For example, BDTH₂ removed 99.9 % of a 50 ppm aqueous Pb(II) solution and 99.97% of an aqueous Hg(II) solution by precipitation, respectively.⁸⁹ Also, BDTH₂ effectively removed toxic metal ions from acid mine drainage and gold ore leachate in high yields.⁹⁰ In comparison, BDTH₂ precipitates Se(IV) from aqueous solution at pH 1. In more alkaline solutions elemental Se forms due to the oxidation of BDTH₂.⁹⁴ BDTH₂ precipitates the aqueous metals from solution where filtration of the chelate allows for easy isolation of the desired metal. The insolubility of the formed chelate is necessary for any effective chemical precipitation agent. Figure 2.1 shows the structure of ABDHT₂, BDTH₂, and the core design.

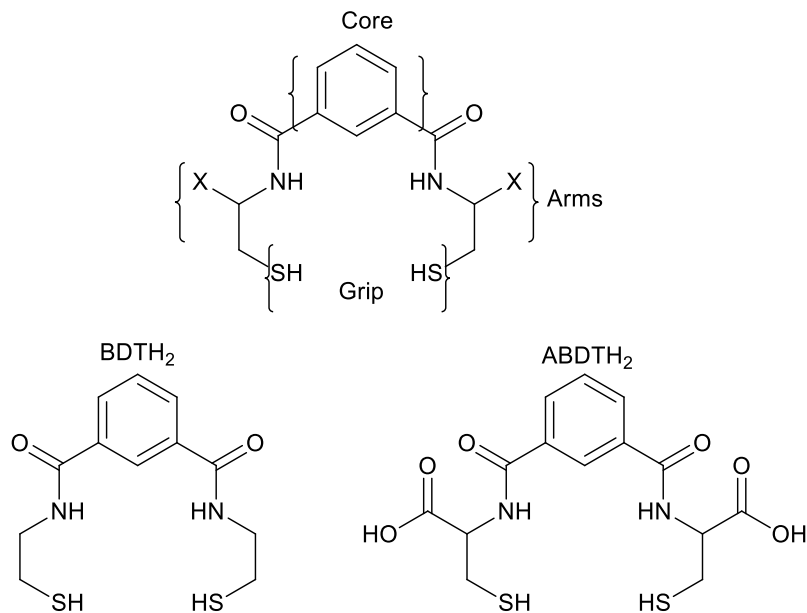


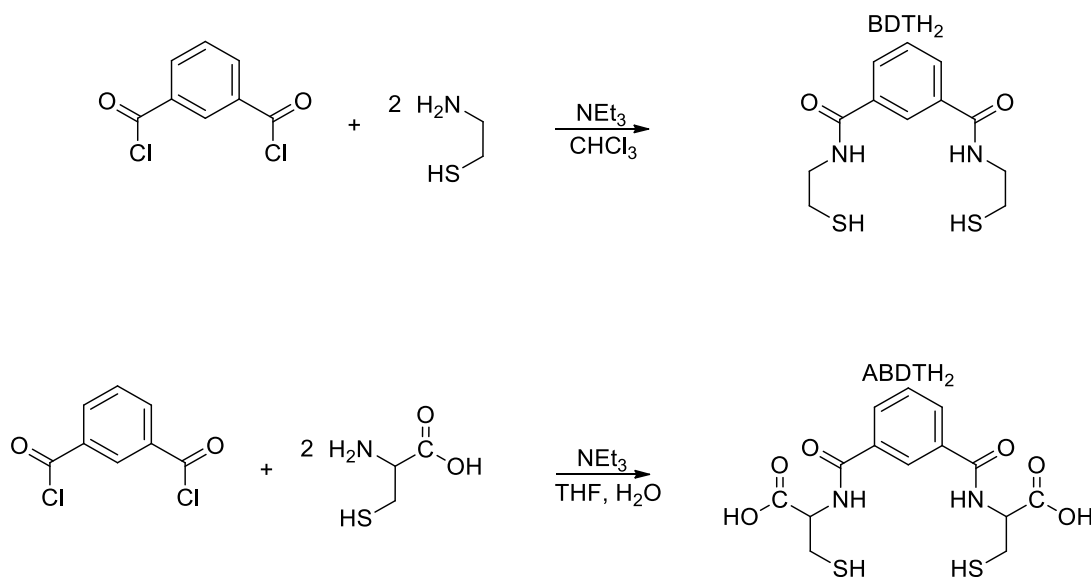
Figure 2.1 Structure of the ligand design: BDTH₂, and ABDTH₂⁸⁸

ABDTH₂ contains two Cys residues linked to the aromatic core via amide bond formation of the N-residue of Cys. The preferential interaction of the “soft” sulfhydryl groups allows for the same functionality as BDTH₂ with one major added benefit. The two carboxylic acid residues (the origin of “A” in ABDTH₂) allow for additional functionality of the ligand to solid supports containing either amine or alcohol functional groups through formation of amide or ester bonds. In theory, the ligand should interact similarly to Cys with coordination of the sulfur atoms to As(III). The core chemistry of As(Cys)₃ formation and related analogs with arsenous acid are discussed in Chapter 1.1. However, compared to Cys, BDTH₂ is more resistant to intramolecular and intermolecular dithiol formation. For example, a multi-month study with BDTH₂ stirring in EtOH open to air did not result in significant dithiol oxidation. Thus the utility and half-life of ABDTH₂ should be improved compared to similar alkyl sulfhydryl compounds with greater solubility in water.

2.2 Results and Discussion

2.2.1 Synthesis and Characterization

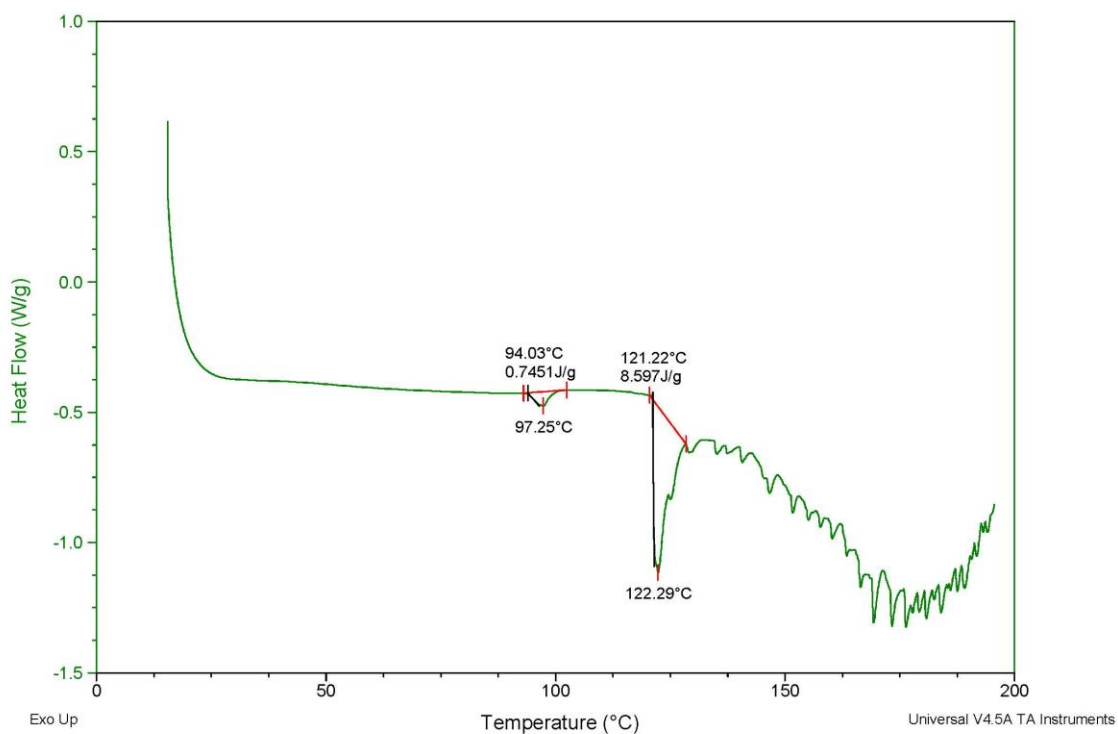
BDTH₂ was prepared by condensation of isophthaloyl chloride with cysteamine hydrochloride following the literature method.⁹² ABDTH₂ was obtained as a slightly yellow foaming solid upon reacting isophthaloyl chloride with L-cysteine using the sterically hindered base triethylamine in a THF-H₂O co-solvent according to Scheme 2.1. The reaction has been shown to be scalable to above 100 g.



Scheme 2.1 Synthesis of BDTH₂ and ABDTH₂

The melting point (MP) of ABDTH₂ was previously reported in the range 105-109 °C. However, a recent analysis of ABDTH₂ with direct scanning calorimetry (DSC) revealed a small endothermic peak at approximately 94.03-97.25 °C corresponding to 0.745 J g⁻¹. This endothermic peak was due to the loss of a small amount of residual THF or water in the as-prepared solid. Further heating revealed a sharp endothermic peak at an

onset temperature of 121.22°C corresponding to 8.587 J g⁻¹. This endothermic peak was assigned to the actual melting point of ABDTH₂. This temperature compares to the MP of BDTH₂; the literature BDTH₂ MP is 133-135 °C.⁹² Decomposition of ABDTH₂ occurred with further heating past 130 °C.



Graph 2.1 DSC results for as-synthesized ABDTH₂

Infrared spectroscopy (IR) reveals a broad peak from nearly 3400 to 2400 cm⁻¹ due to the presence of the carboxylic acid groups. Bands corresponding to aromatic C-H, methylene C-H, acid carbonyl (C=O), amide carbonyl, and N-H bending were located at 3060, 2972, 1720, 1625, and 1578 cm⁻¹, respectively. Importantly, a sharp peak was observed at 2559 cm⁻¹ corresponding to the free thiol groups present on ABDTH₂ which

is comparable to the thiol band of BDTH₂ located at 2560 cm⁻¹. ESI (electrospray ionization) mass spectrum contained a molecular ion peak located at 373 m/z (C₁₄H₁₆N₂O₆S₂), and confirmed the structure of ABDTH₂. The ¹H NMR (400 MHz) spectrum in DMSO-*d*₆ contained signals at δ 7.60, 8.06, and 8.41 ppm corresponding to the aromatic protons. The thiol peak was located at δ 2.60 ppm, while the amide NH, methylene CH at α and β carbons were located at δ 8.90, 2.90, and 4.50 ppm, respectively. The characterization data from IR, GC-MS, DSC, and NMR all compare similarly with BDTH₂.

2.3 Experimental

2.3.1 Reagents

All the reactions were carried out at room temperature under nitrogen protection. The following reagents and solvents were obtained commercially and used as received: L-cysteine hydrochloride (98%), cysteamine hydrochloride (>98%), triethylamine (>99.5%), and isophthaloyl chloride (>99%) from Sigma-Aldrich; Omnitrace hydrochloric acid (HCl) from EMD; DMSO-*d*₆ (99.9%) and CDCl₃-*d*₁ (99.9%) from Cambridge Isotope Laboratories Inc.; solvents from PHARMCO-AAPER; water was distilled and deionized (18 MΩ cm).

2.3.2 Analytical Techniques

DSC was performed on a TA Q-20. ¹H NMR of BDTH₂ and ABDTH₂ were produced in CDCl₃-*d*₁ and DMSO-*d*₆ using tetramethylsilane (TMS) as an internal standard on a Varian INOVA instrument at room temperature at an operating frequency of 399.78 MHz with a pulse of 71.2°. MS was obtained on a Finnegan LTQ instrument. IR spectra were

obtained on Nicolet Avatar 370 DTGS IR spectrophotometer (Thermo Electron Corporation). MP values were recorded on a MEL-TEMP instrument from Laboratory Devices.

2.4 Synthesis

2.4.1 BDTH₂ Synthesis

Triethylamine (156 mL, 114 g, 1.13 mol) was added to a stirring solution of cysteamine hydrochloride (63.85 g, 559.8 mmol) in CHCl₃ (600 mL). The resulting clear solution was stirred for 5 min. Isophthaloyl chloride (37.52 g, 184.44 mmol) in CHCl₃ (100 mL) was added dropwise to the reaction and stirred for 12 h. The solution was divided into two equal parts and each washed with 10 % aq. HCl (50 mL; 200 mL total). The organic extracts were combined and dried over Na₂SO₄ before the solvent was removed under vacuum to produce BDTH₂ as a white solid (22.05 g, 42% yield).⁹²

2.4.1.1 Characterization

MP: 135-137°C; IR: 3247 (secondary NH), 3066 (m, aromatic C-H), 2962 (m, methylene C-H), 2560 (m, S-H), 1647 (s, amide (C=O)), 1541 (NH); ¹H NMR (DMSO-*d*₆, 400 MHz): δ (ppm) - 2.47 [t, 2H, SH], 2.70 [t, 4H, CH₂], 3.48 [q, 4H, CH₂], 7.58 [t, 1H, ArH], 7.94 [d, 2H, ArH], 8.32 [s, 1H, ArH], 8.80 [s, 2H, NH]; MS (+ESI): 285 (C₁₂H₁₆N₂O₂S₂).

2.4.2 ABDTH₂ Synthesis

Triethylamine (114 mL, 83.5 g, 826 mmol) was added to a stirring solution of L-cysteine (100.2 g, 826 mmol) in water (800 mL, DI). The resulting clear solution was stirred for 5 min. Isophthaloyl chloride (80.0 g, 394 mmol) in THF (800 mL) was then added

dropwise to the reaction and stirred for 12 h. The solution was divided into two equal parts and each extracted with ethyl acetate (400 mL; 800 mL total). The ethyl acetate extracts were combined and dried over Na₂SO₄ before the solvent was removed under vacuum to produce ABDTH₂ as a light yellow solid (113 g, 76% yield).

2.4.2.1 Characterization

MP: 105-109°C; DSC: small endotherm 97-101°C (loss of solvent), 121°C sharp endotherm (MP), 130°C (decomposition); IR: 3337 (broad, acid OH and secondary NH), 3066 (m, aromatic C-H), 2962 (m, methylene C-H), 2568 (m, S-H), 1734 (s, acid (C=O)), 1647 (s, amide (C=O)), 1533 (NH); ¹H NMR (DMSO-*d*₆, 400 MHz): δ (ppm) - 2.60 [t, 2H, SH], 2.90 [m, 4H, CH₂], 4.50 [m, 2H, CH], 7.60 [t, 1H, C₆H₄], 8.06 [d, 2H, C₆H₄], 8.41 [s, 1H, C₆H₄], 8.90 [d, 2H, NH]; MS (+ESI): 373 (C₁₄H₁₆N₂O₆S₂).

2.5 Conclusion

Both the acid-free derivative BDTH₂ and Cys derivative ABDTH₂ capable of covalent metal bonding to As(III) were synthesized through amide bond formation with N-cysteamine and N-Cys residues with isophthalic acid chloride, respectively. They were characterized by DSC, IR, MS, and ¹H NMR in good agreement confirming the structure. Subsequent chapters discuss the use of both ligands for the precipitation of various forms of arsenic. Also, ABDTH₂ is compatible with solid support composites through the carboxylic acid groups and as a surface passivating ligand. In this way, solid support remediation will be enhanced by the covalent removal of arsenic species through S-As bonds compared to simple adsorption removal.

Chapter 3 Aqueous Arsenite Precipitation with Dithiols BDTH₂ and ABDTH₂

3.1 Introduction

This chapter will explore the combination of both BDTH₂ and ABDTH₂ for the removal of arsenous acid, As(OH)₃, and evaluate the structural characteristics of possible BDT-As(III) and ABDT-As(III) precipitates. Additionally, the aqueous leaching of BDT-As(III) and ABDT-As(III) precipitates will be examined containing other “soft” toxic metal cations and ion-free solutions. Finally, both BDTH₂ and ABDTH₂ will be evaluated as potential chelate ligands for the removal of arsenic acid, AsO₄H₃.

3.1.1 BDTH₂ and ABDTH₂ Interactions with Aqueous Arsenite

Both BDTH₂ and ABDTH₂ can form covalent S-As(III) bonds through the bidentate sulfhydryl groups. Structures with a varying degree of As-S_x bonds are possible.^{5-6, 12-13, 33} Figure 3.1 shows several examples, structures (a-e), of some of the possible combinations of As(III) and a bidentate sulfhydryl compound, HS₂R. Structure (a) consists of only one sulfhydryl group bonded as As(H₁S₂R)(OH)₂ with an additional free sulfhydryl. Structure (b) contains both bidentate sulfhydryl groups bonding as As(H₂S₂R)(OH). Structure (c) contains both intramolecular bidentate sulfhydryl groups bonding and an additional sulfhydryl from HS₂R as As(H₂S₂R₁)(H₁S₂R₂) with an additional free sulfhydryl. Structure (d) contains two separate HS₂R with both monodentate bonding as As(H₁S₂R)₂(OH) with two free sulfhydryl groups. Lastly, structure (e) contains three HS₂R each with monodentate bonding as As(H₁S₂R)₃ with three additional free sulfhydryl groups. Structure (b) represents the optimal geometry for both BDTH₂ and ABDTH₂ for covalent removal of As(III) without the possibility of additional bonding to other As(III) atoms. The 14-membered cyclic structure with

another pendant hydroxide is proposed as the main bonding arrangement expected due to the bond angles of the ligands when combined in a 1:1 ratio.^{88,94} More complexity is possible when combined with ratios greater than 1:1 with any structure other than (b). As a result, growing networks of oligomeric and polymeric bonding to random As(III) atoms from multiple sulfhydryl groups may form. Structures (a), (c), (d), and (e) are all capable of this random network formation.

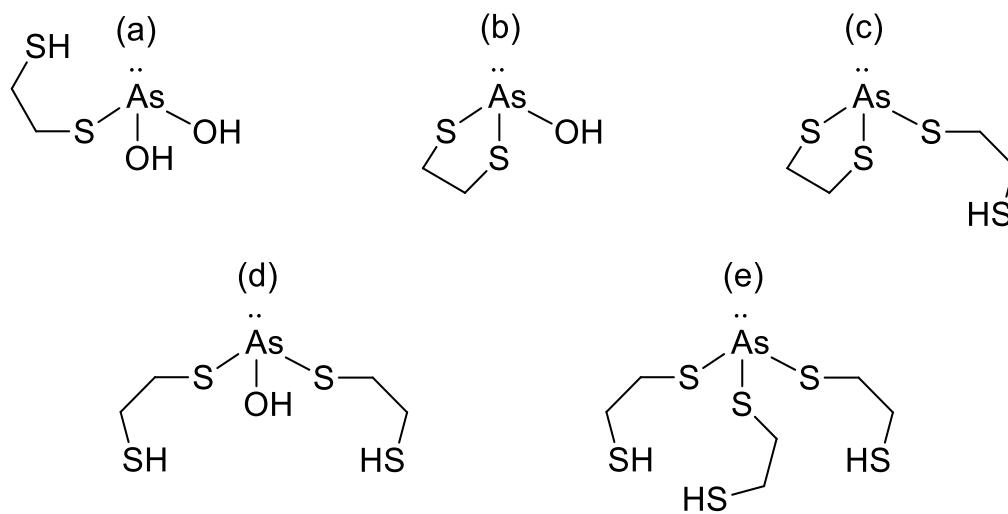


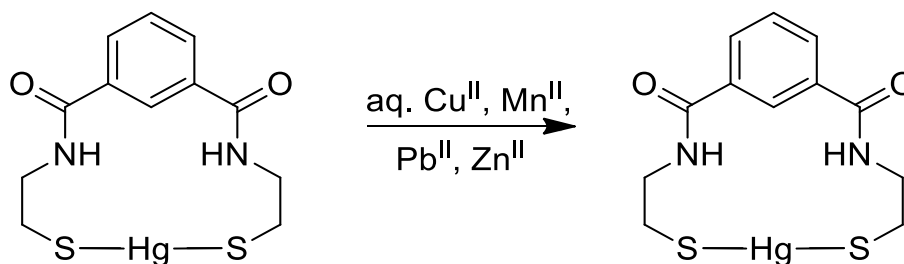
Figure 3.1 Several potential products with bidentate sulfhydryl ligands with aqueous As(III)

This section will explore the combination of BDTH₂ and ABDTH₂ with aqueous As(III). A complete characterization of their precipitation products in peer-reviewed literature is incomplete. New insights from the interaction of ABDTH₂ with As(III) will hopefully prove that the ligand is capable of covalent S-As(III) removal both as a chemical precipitation chelate and when supported on solid supports through the

carboxylic acid groups. Any potential interactions of the acid groups with As(III) may interfere with the ability of the ligand for further functionalization.

3.1.2 Arsenic Leaching and Soft Metal Preferences

Wastewater, both agricultural and industrial, and contaminated natural waters may contain a variety of toxic metals and metalloids. For example, aqueous As, Cd, Hg, and Pb solutions are all potential acute risk toxins resulting from ingestion.⁴² Common to each toxin is their placement on the hard-soft-acid-base (HSAB) concept by Pearson as “soft” metals where $\text{Hg(II)} > \text{Pb(II)} > \text{Cd(II)} > \text{As(III)}$.⁹⁸ General reactivity follows that sulfhydryl groups have a higher affinity towards metals with increasing softness.⁹⁸ For example, ROS_2^- selectivity is $\text{Hg(II)} > \text{Cu(II)} > \text{Cd(II)} > \text{Zn(II)}$.⁹⁹ Also, BDT-Hg(II) mixed with other “soft” metals Cd(II), Cu(II), Mn(II), Pb(II), and Zn(II) does not result in S-Hg(II) bond displacement (Scheme 3.1).¹⁰⁰ Moreover, formation constants with thiol-containing peptides (TCP) mixed with aqueous Hg(II), Cd(II), and Pb(II) support this trend.¹⁰¹ However, at low molar concentrations of Hg(II) and high concentrations of other soft metals this trend of binding is not always kinetically favored.¹⁰²



Scheme 3.1 BDT-Hg(II) inertness towards other soft aqueous metals

Sulfhydryl groups act as highly competitive binding sites for As(III) in a wide range of environmental systems. As an example, the sulfhydryl groups present on a model adsorbent (Ambersep GT74 resin) had nearly identical affinities for aqueous As(III) when mixed with ferrihydrite ($\text{Fe}(\text{OH})_3$) at pH 7.¹⁰³ Also, the formed RS-As(III) bonds were stable to oxidation ($t_{1/2} = 318$ days). There is a need to identify “soft” metal preferences that may exist for potential sulfhydryl chelating compounds in areas where increased arsenic concentrations, specifically As(III), are problematic. This section will determine potential arsenic leaching from BDT-As(III) and ABDT-As(III) complexes when mixed with ion-free and mixed metal ions at concentrations typical of acute risk of exposure (100-200 ppb). These soft metal ions include Cd, Hg, and Pb.

3.1.3 BDTH₂ and ABDTH₂ Arsenate Interactions

The metabolic pathway of As(V) in humans continues to be a contentious area of research.⁴³ The difference in reactivity between free sulfhydryl groups and As(III) and As(V) behave as predicted by Pearson’s hard-soft-acid-base (HSAB) concept.⁹⁸ Contrary to this trend, Figure 3.2 displays several recent examples that contain S-As(V) bonds found in nature. Dimethylarsinothioyl glutathione (A) contains a RS-As(V) bond found in cabbage extract.¹⁰⁴ This was the first example, in 2007, of a biologically important molecule with S-As(V) bond formation via thiolate activation. Also, arsenic exposure can lead to excretion of (B) dimethyl-monothioarsinic acid (DMMTAs(V)) and (C) dimethyldithioarsinic acid (DMDTAs(V)) in human urine.¹⁰⁵⁻¹⁰⁶

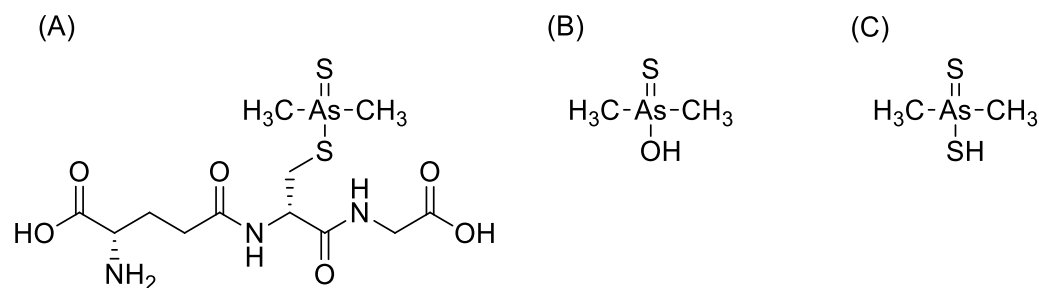
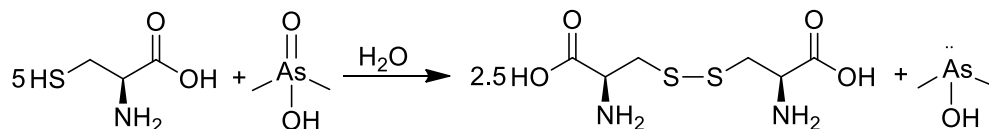


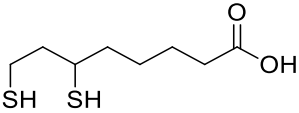
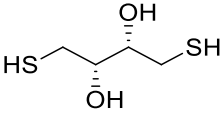
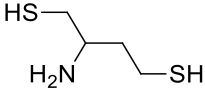
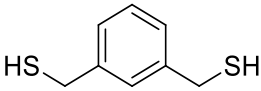
Figure 3.2 Recent examples of S-As(V) bond formation

“Hard” anions can also influence sulfhydryl groups through redox reactions.¹⁰⁷ For example, both Cys and GSH reduce As(V) to As(III) concomitant with oxidation to cystine and GSSG (Scheme 3.2) in aqueous solution, respectively.^{17, 33} This quantitative reduction required 5 mol equivalents of Cys.¹⁷ The oxidation of many bidentate sulfhydryl compounds to the corresponding disulfide are useful as potent reducing agents.⁹⁷ Table 3.1 lists the redox properties of other bidentate sulfhydryl compounds. The redox properties of every sulfhydryl group are in comparison to GSH. GSH is the “gold standard” due to its ubiquitous concentration biochemically.¹⁰⁸ Each example in Table 3.1 oxidizes to an intramolecular disulfide except for phenylenedimethanethiol which forms a cyclic dimer, and shares similarities in structure to both BDTH₂ and ABDTH₂.



Scheme 3.2 As(V) reduction to As(III) via dithiol oxidation of Cys

Table 3.1 Various bidentate sulfhydryl redox properties

| Compound | Structure | Potential (V) | pH | Ref. |
|------------------------------|---|---------------|----|------|
| dihydrolipoic acid (DHLA) |  | -0.288 | 7 | 109 |
| dithiothreitol (DTT) |  | -0.327 | 7 | 109 |
| dithiobutylamine (DTBA) |  | -0.317 | 7 | 97 |
| 1,3-phenylenedimethanethiol |  | -0.275 | 7 | 109 |

This section will explore the possible interactions of both BDTH₂ and ABDTH₂ with arsenic acid. Identification of potential covalent S-As(V) bond formation, reduction of As(V) to As(III), and oxidation of the sulfhydryl groups to dithiols will be accessed in detail. Here both BDTH₂ and ABDTH₂ will be used with 5 equivalent mol excess compared to As(V).

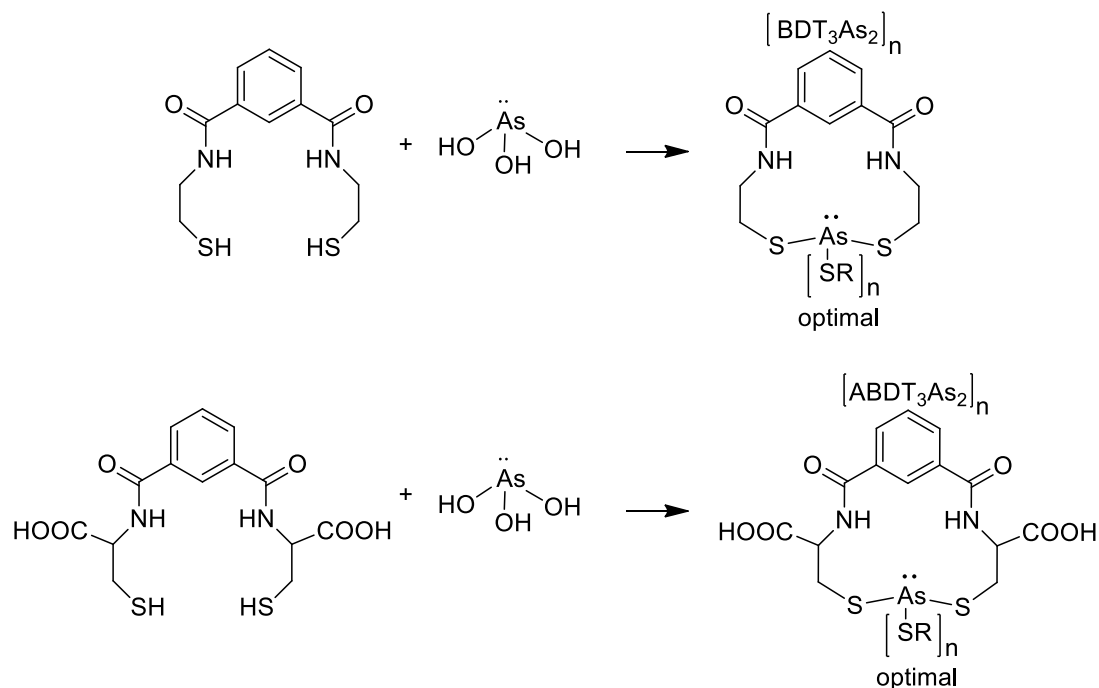
3.2 Results and Discussion

3.2.1 BDT-As(III) and ABDT-As(III)

The combination of aqueous As(III), as As(OH)₃, with BDTH₂ and ABDTH₂ was explored with excess amounts of As(III). A white solid formed immediately upon the

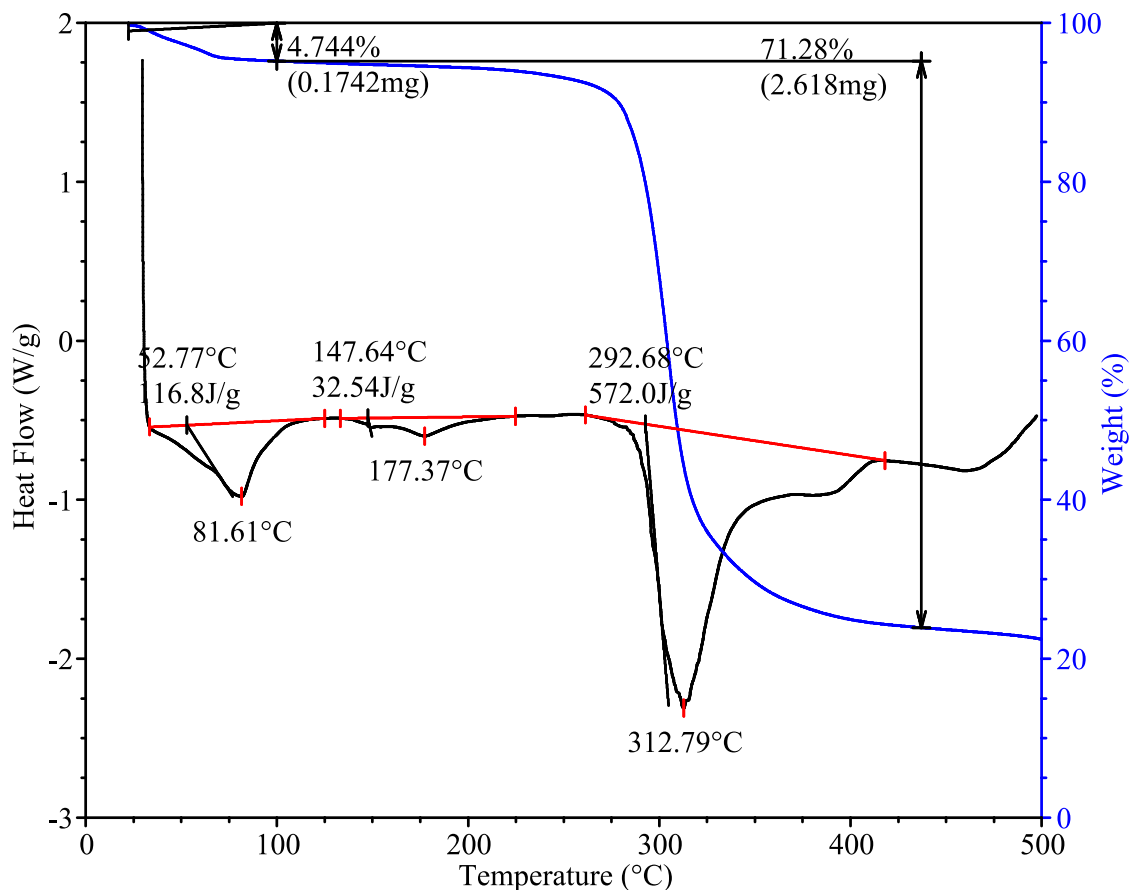
addition of small aliquots of each dissolved in EtOH. Both formed amorphous precipitates (determined by powder X-ray diffraction) and are not soluble in any common organic solvent suitable for ^1H NMR analysis. Here the insolubility contrasts with both the $\text{As}(\text{Cys})_3$ and $\text{As}(\text{GS})_3$ complexes that were slightly soluble in water.³⁴ This attempt was exhausted after trying several suggested special solvent derivatives with no success. Elemental analysis of the BDTH_2 and ABDTH_2 precipitation product shows the S:As ratio was 3.2 and 3.3, respectively. Thus this supports the formation of derivatives of $[\text{BDT}_3\text{As}_2]_n$ and $[\text{ABDT}_3\text{As}_2]_n$ shown in Scheme 3.3. In comparison both DTT, DMSA, and 1,3-propanedithiol also formed L_3As_2 structures with $\text{As}(\text{III})$.^{13, 34}

Both BDTH_2 and ABDTH_2 were very effective towards the removal of aqueous $\text{As}(\text{III})$. The yield was 87% based on the structure of $[\text{BDT}_3\text{As}_2]_n$ and 82% based on the structure of $[\text{ABDT}_3\text{As}_2]_n$. Oligomeric formation of $[\text{BDT}_3\text{As}_2]_n$ and $[\text{AsBDT}_3\text{As}_2]_n$ might explain insolubility in common organic solvents. Scheme 3.1 shows multiple derivative pathways that can form extensive networks. The insolubility of both in water and the possible oligomeric product may hinder complete sequestration. However, this does not rule out adsorption as another possible removal pathway. These results compare to other sulfhydryl ligands that have high affinity towards aqueous $\text{As}(\text{III})$ listed in Table 1.3. Combinations with different mol ratios of ligand to $\text{As}(\text{III})$ were also evaluated. However, the S:As ratio was always determined to be >3 . The optimized bidentate structure with a pendant hydroxide was never isolated from these reactions with both BDTH_2 and ABDTH_2 . Structure determination of the precipitates with direct probe GC-MS led to decomposition and formation of arsenic sulfides (As_4S_4 , As_4S_3 , and As_4S_2 etc.) and ligand backbone for both BDT- $\text{As}(\text{III})$ and ABDT- $\text{As}(\text{III})$ products.



Scheme 3.3 BDT-As(III) and ABDT-As(III) proposed network structures, SR = BDT and ABDT

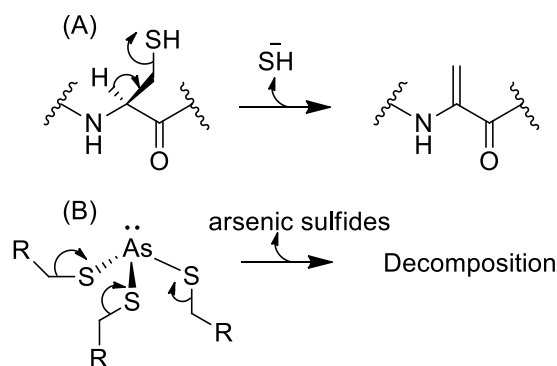
The DSC (Graph 3.1) for BDT-As(III) had a small endothermic peak at 82 °C with $\Delta H = 16.8 \text{ J g}^{-1}$ (EtOH & H₂O), and a small endothermic peak at 177 °C with $\Delta H = 32.5 \text{ J g}^{-1}$ (melting point). Decomposition of the precipitate occurred with additional heating at 313 °C with $\Delta H = 572 \text{ J g}^{-1}$. The decomposition temperature is close to the known literature melting point for As₂S₃ and As₄S₄ at 310 and 307 °C, respectively. In comparison, the melting point of BDTH₂ mixed with aqueous Se(IV) occurred at 180-183 °C.⁹⁴ The TGA (Graph 3.1) curve had a small mass loss of 4.74% from dehydration and was stable until decomposition. The thermal stability of the BDT-As(III) product compares similarly to other oligomeric covalent solids such as metal organic frameworks, MOFs.



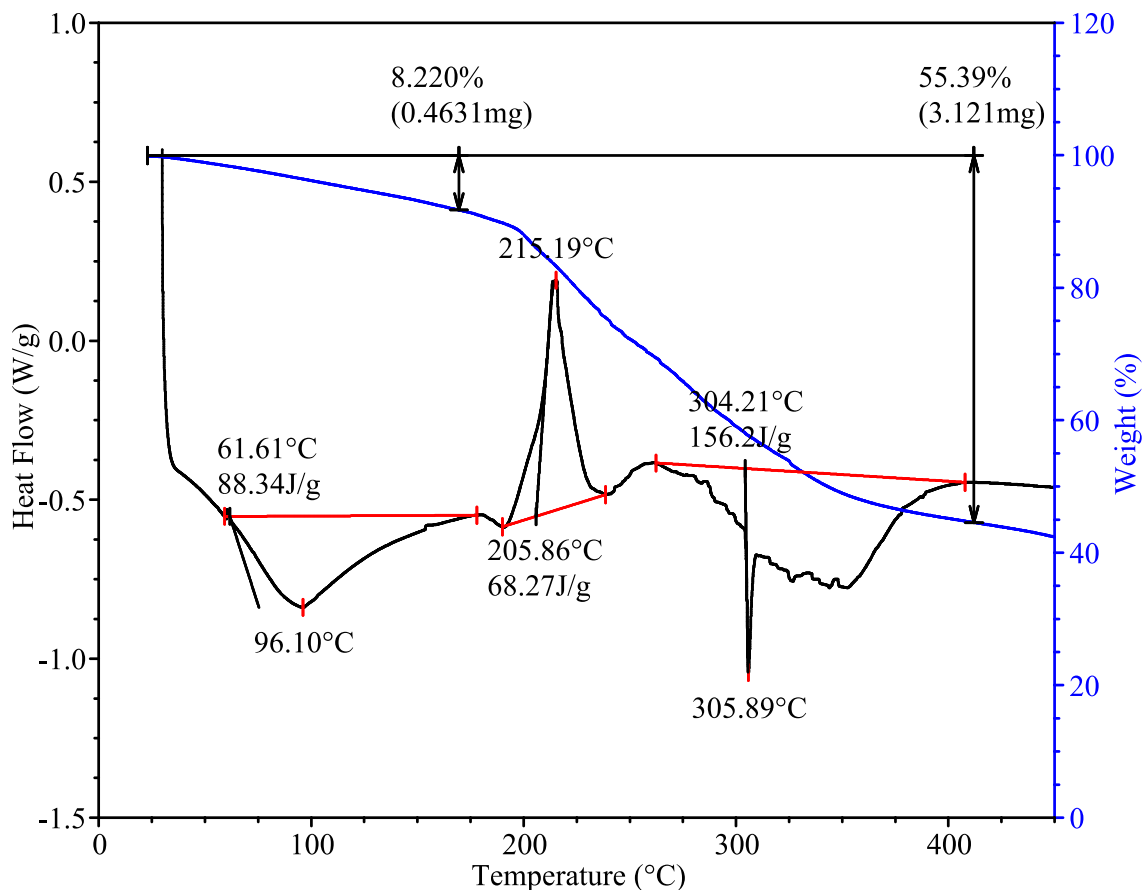
Graph 3.1 DSC (black) and TGA (blue) for BDT-As(III) precipitate

The DSC for the ABDT-As(III) precipitate had a small broad endotherm at 96 °C (EtOH and H₂O) followed by a sharp exothermic peak at 215 °C with $\Delta H = 68 \text{ J g}^{-1}$ (Graph 3.2). Interestingly, the precipitate turned red at this temperature when taking the melting point. This exotherm may represent the crystallization or formation of As(III)-trisulfide as As₂S₃ or As₄S₄, a red-colored solid, followed by subsequent reorganization or decomposition of the ABDT backbone. The precipitate decomposed at 306 °C corresponding to $\Delta H = 156 \text{ J g}^{-1}$. This thermal stability compares similarly with the decomposition temperature of the BDT-As(III) product at 313 °C. There is a general lack

of studies comparing the thermal stability of $RS_x\text{-As(III)}$ chelates based on the structure of L-Cys with DSC. Interestingly, the addition of bidentate carboxylic acids compared to BDTH₂ may help promote the exothermic peak at 215 °C. The C-S bond in L-Cys is more labile compared to the backbone in cysteamine with BDTH₂. Scheme 3.4 shows the base activated formation of dehydroalanine. The acidity of the chiral C-H helps promote elimination of SH⁻. Similar unpublished results with ABDTH₂ and ester derivatives also formed similar exothermic peaks when complexed with Hg, Cd, and Pb. The TGA (Graph 3.2) showed the product is stable with slow dehydration up until 200 °C followed by a large mass loss during decomposition. No crystalline phases were detected with X-ray diffraction following isothermal heating above 200 °C in an attempt to show As₂S₃ formation.



Scheme 3.4 Base-mediated elimination of Cys to dehydroalanine (A) and potential arsenic sulfide formation with $RS_3\text{As(III)}$ chelates while heating (B)



Graph 3.2 DSC (black) and TGA (blue) results for ABDT-As(III) precipitate

Table 3.2 lists the significant Raman frequencies for the BDT-As(III) and ABDT-As(III) products supporting the formation of covalent As(III)-S bonds.^{110,111} The region of 350-450 cm^{-1} is usually assigned to the vibrational modes for As(III)-S bonds.¹¹⁰ A strong sulfhydryl SH absorption at 2548 cm^{-1} in BDTH₂ is not observed in the BDT-As(III) product. Importantly, the BDT-As(III) product contained a strong absorption at 383 and 362 cm^{-1} corresponding to As(III)-S bond formation and lacks disulfide S-S oxidation near 510 cm^{-1} , respectively.⁹⁴ The small bands for C-S stretching at 651 and 632 cm^{-1} are preserved in the BDT-As(III) product with slight broadening at 637 cm^{-1} .

ABDTH₂ had two moderate S-H stretching vibrations at 2559 and 2426 cm⁻¹, respectively. The peak at 2426 cm⁻¹ is due to SH···O stretching.¹¹² The peak at 2559 cm⁻¹ is the normal SH stretching vibration for sulfhydryl groups but may include bands from SH···S. Importantly, the S-H absorptions are not observed in the ABDT-As(III) precipitate. Also, there is no band supporting disulfide S-S formation located near 510 cm⁻¹.⁹⁴ Absorption for the As(III)-S bond was at 375 and 352 cm⁻¹, respectively. The small broad band for C-S stretching is preserved at 640 and 635 cm⁻¹, respectively. Thus both the BDT-As(III) and ABDT-As(III) products support the removal of As(III) through the formation of covalent S-As(III) bonds.

Table 3.2 Raman shift frequencies for BDT-As(III) and ABDT-As(III)

| Bond Type | BDTH ₂ (cm ⁻¹) | BDT-As (cm ⁻¹) | ABDTH ₂ (cm ⁻¹) | ABDT-As (cm ⁻¹) |
|-----------|---------------------------------------|----------------------------|---|--------------------------------|
| S-H | 2548 | - | 2559, 2426 | - |
| S-S | - | - | - | - |
| S-C | 651 | 638 | 640 | 635 |
| S-As | - | 383, 362 | - | 375, 352 |

These results compare similarly to other precipitation products with As(III). For example, a Cys-rich biomaterial combined with arsenous acid contained S-As(III) absorptions in the range 340-420 cm⁻¹.¹¹¹ Also, As(III) precipitated with L-Cys showed S-As(III) bond absorptions in the range of 401-369 cm⁻¹.¹¹¹ The density functional theory (DFT) predicted absorptions for the O-As(III) bond at 600, 609, and 633 cm⁻¹ were not

observed.¹¹¹ The latter may be present, but there was overlap due to the proximity of the S-C band at 638 and 635 cm^{-1} in BDT-As(III) and ABDT-As(III), respectively.

3.2.3 Arsenic Leaching and Soft Metal Preferences

Both BDT-As(III) and ABDT-As(III) were stirred in aqueous solutions to determine the stability of their S-As(III) bonds. Also, each was evaluated for leaching in the presence of other “soft” metal ions. The concentrations were chosen to represent extremely hazardous levels to humans (100-200 ppb). For example, the safe limits for Hg, Cd, and Pb set by the World Health Organization (WHO) are 6, 3, and 10 ppb, respectively. Table 3.3 shows elemental analysis results for the leaching studies with BDTH-As(III). The limit of detection for each element was 10 ppb. The S-As bonds in BDT-As(III) were stable in ion-free aqueous solutions. After a 24 h batch leaching study, only 2.9% of the available arsenic leached into solution. BDT-As(III) also demonstrated that stability involves a dynamic equilibrium with other “soft” ions in solution. For example, the Hg(II) concentration was below the detection limit after stirring for 12 h. With increased time all of the available other “soft” ion concentrations were below the detection limit. These results highlight that BDTH₂ is a viable option for the removal of As(III), but may lead to leaching if exposed to high concentrations of these other ions.

Table 3.3 ICP-OES results for BDT-As(III) leaching

| Time (h) | Hg (nmol) | % Rem. | Cd (nmol) | % Rem. | Pb (nmol) | % Rem. | As (μ mol) | % Leach |
|--------------------|--------------|-----------|--------------|-----------|--------------|-----------|--------------------|------------|
| T ₀ mol | 49.36 | | 97.8 | | 43.89 | | 311 | - |
| 12 | BDL | 100 | 10.4 | 89 | 26.03 | 41 | 11.0 | 3.5 |
| 24 | BDL | 100 | BDL | 100 | BDL | 100 | 10.3 | 3.3 |
| 24 ion-free | - | | - | | - | | 9.1 | 2.9 |

The S-As(III) bonds in BDT and ABDT showed similar stability. Table 3.4 shows the elemental analysis results for ABDT-As(III) leaching in ion-free and mixed “soft” ions in aqueous solution. Arsenic leaching was slightly higher in ABDT compared to BDT. Also, exchange reactions with ABDT were faster with the other “soft” ions. All of the available metal concentrations were below the detection limit after 12 h. None of the other metal concentrations increased after removal. It should be noted there is a possibility that error in the % As leach from both of these studies includes physically adsorbed As(III). Adsorbed As(III) may flag a false positive for leaching.

Table 3.4 ICP-OES results for ABDT-As(III) leaching

| Time (h) | Hg (nmol) | % Rem. | Cd (nmol) | % Rem. | Pb (nmol) | % Rem. | As (μ mol) | % Leach |
|--------------------|--------------|-----------|--------------|-----------|--------------|-----------|--------------------|------------|
| T ₀ mol | 49.36 | - | 97.8 | - | 43.89 | - | 211 | - |
| 12 | BDL | 100 | BDL | 100 | BDL | 100 | 14.58 | 7 |

| | | | | | | | | |
|-------------|-----|-----|-----|-----|-----|-----|-------|-----|
| 24 | BDL | 100 | BDL | 100 | BDL | 100 | 18.59 | 8.8 |
| 24 ion-free | - | | - | | - | | 15.39 | 7.2 |

These results are indicative of the trends other sulfhydryl-containing groups have towards “soft” metals.⁹⁹ For example, BDTH₂ has a preference for Hg(II) in aqueous solution.¹⁰⁰ The dynamic equilibrium of sulfhydryl groups for other “soft” ions in solution is a disadvantage of using a system that only relies on sulfhydryl chemistry. Determining the half-life of bond stability for applications involving water filtration is practically worthless if not established in real-world conditions.¹⁰³ However, all of these “soft” metals are known carcinogens in humans. Specificity for a single ion is a limitation by itself. Thus these results highlight that both BDTH₂ and ABDTH₂ are useful chemical precipitation chelates for the removal of various “cocktails of death”.¹¹³

3.2.4 BDTH₂ and ABDTH₂ Arsenate Interactions

Both BDTH₂ and ABDTH₂ (5 eq.) dissolved in EtOH were combined with aqueous sodium arsenate (5 ppm). Unlike the results with arsenous acid, there was no immediate precipitation after each addition. The resulting solution turned murky off-white in color over time. The latter is possibly due to the insolubility of both BDTH₂ and ABDTH₂ in water. Table 3.5 lists the elemental analysis results with ICP-OES of the aqueous phase showing very little removal of total arsenic. The removal yields are so low for both BDTH₂ and ABDTH₂ that experimental error from dilution may be a factor. Thus there is a significant discrepancy in reactivity between the different oxidation states of arsenic for both compounds. Analysis of the recovered solids by IR and ¹HNMR also

supports no interaction of the sulfhydryl groups with As(V). Also, there was no change in the melting points of both BDTH₂ and ABDTH₂ following recovery.

Table 3.5 ICP-OES results for aqueous arsenate and 5X mol excess of BDTH₂ and ABDTH₂

| Sample | As (ppm) | % Removal |
|------------------------------|------------|-----------|
| Stock Solution | 4.99 ±0.04 | --- |
| 5X BDTH ₂ Excess | 4.89 ±0.02 | 2 |
| 5X ABDTH ₂ Excess | 4.85 ±0.03 | 3 |

One drawback for using ICP-OES is the non-discriminant correlation of total element concentrations. The arsenic still present in solution could be reduced As(III) which is the product for both Cys and GSH when mixed with arsenic acid. Table 3.6 lists the removal of arsenate results with anionic exchange chromatography (IC). IC results confirm that most of the total arsenic present in the aqueous phase is As(V). The original As(V) concentration remained nearly unchanged with BDTH₂. ABDTH₂ did show some significant reduction in As(V) with 8% less than the stock concentration. It should be noted arsenite was undetectable with the IC and buffer in this study. Several attempts at identifying arsenite retention on the column by spiking effluent were undetectable.

Table 3.6 IC results for the combinations of BDTH₂ and ABDTH₂ with As(V)

| Sample | Arsenate (ppm) | % Arsenate Remaining |
|--------|----------------|----------------------|
|--------|----------------|----------------------|

| | | |
|------------------------------|-------|-----|
| Stock Solution | 6.174 | --- |
| 5X BDTH ₂ Excess | 6.186 | 100 |
| 5X ABDTH ₂ Excess | 5.680 | 92 |

These results highlight the selection bias these molecules have for As(III) as chemical precipitation chelates. The oxidized forms of BDT and ABDT, either as cyclic intramolecular or intermolecular disulfide, are unknown. However, based on similar bidentate sulfhydryl compounds intermolecular seems most likely.⁸⁶ Their low solubility in water may promote resistance to dithiol formation. The exchange between disulfide S-S and metal thiolate M-S bonds is a dynamic equilibrium for a variety of metal ions. For example, copper which is an especially important biological redox metal is in equilibrium with Cu(I)-disulfide and Cu(II)-thiolate formation.¹¹⁴ Also, arsenic toxicity in humans involves the redox cycle between arsenic and sulfhydryl-disulfide groups. These results show that both BDTH₂ and ABDTH₂ behave more as predicted by HSAB theory and less as viable redox active ligands with As(V) in mixed aqueous solutions.

3.3 Experimental

3.3.1 Reagents

The following reagents and solvents were obtained commercially and used as received: sodium meta-arsenite (NaAsO₂, >98%), sodium arsenate heptahydrate (Na₂HAsO₄ · 7H₂O, >98%), mercury chloride (HgCl₂, >99.5%), cadmium chloride dihydrate (CdCl₂ · 2H₂O, >98 %), lead acetate trihydrate (Pb(CH₃COO)₂ · 3H₂O, 98%) from Sigma-Aldrich; Omnitrace hydrochloric acid (HCl) and nitric acid (HNO₃) from

EMD; DMSO-*d*₆ (99.9%) from Cambridge Isotope Laboratories Inc.; solvents from PHARMCO-AAPER; water was distilled and deionized (18 MΩ cm).

3.3.2 Analytical Techniques

DSC was measured on a TA Q-20. ¹H NMR of BDTH₂ and ABDTH₂ was produced in DMSO-*d*₆ using tetramethylsilane (TMS) as internal standard on a Varian INOVA instrument at room temperature at an operating frequency of 399.78 MHz with a pulse of 71.2 deg. Infrared spectra (IR) were obtained on a Nicolet Avatar 370 DTGS IR spectrophotometer manufactured by Thermo Electron Corporation. Raman spectra were recorded on a Thermo Scientific DXR Raman Microscope with a 532 nm laser at 0.1 mW. Thermogravimetric analysis (TGA) was obtained on a TA instrument Q5000 from 30 °C to 500 °C under nitrogen. The concentrations of total arsenic were obtained using a Varian Vista-Pro CCD Simultaneous ICP-OES at a wavelength of 188.98 nm. Yttrium internal standard was used (371.029 nm) to evaluate and/or correct for matrix effects. Laboratory control samples (LCS) were produced with diluted elemental standards in 1% HNO₃. Digestions were done with a 3:1 HCl/HNO₃ solution followed by heating for 4 h at 95 °C. Melting points were obtained on a MEL-TEMP instrument from Laboratory Devices. GC-MS obtained with ThermoFinnigan PolarisQ Ion Trap Mass Spectrometer with Solids Probe. Ion chromatography was performed on a Dionex ICS 2500 using an IonPac AS18 column preceded by an AS18 guard column with a 28 mM sodium carbonate eluent solution.

3.4 Synthesis

3.4.1 BDT-As(III) Synthesis (1.5X BDTH2)

Sodium arsenite, NaAsO₂ (0.250 g, 1.90 mmol), was dissolved in water (50 mL). A solution of BDTH₂ (0.694g, 2.54 mmol) in EtOH (50 mL) was added to the arsenite solution in small aliquots over 1 h. After each repeated addition an off-white solid precipitate formed immediately. The reaction mixture was stirred for an additional 6 h. The solution was acidified with 5% HCl and isolated by filtration. The precipitate was washed with water (200 mL) and acetone (100 mL) followed by drying under vacuum at RT. Yield = 0.546 g, 67%.

3.4.1.1 Characterization

Mp: 169-177°C; IR (cm⁻¹): 3337 (secondary NH), 3066 (m, aromatic C-H), 2962 (m, methylene C-H), 1647 (s, amide (C=O)), 1533 (NH); ICP-OES: 3.4 (sulfur:arsenic ratio).

3.4.2 BDT-As(III) Synthesis (Excess As)

Sodium arsenite, NaAsO₂ (1.09 g, 8.36 mmol), was dissolved in water (50 mL). A solution of BDTH₂ (0.501 g, 1.84 mmol) in EtOH (50 mL) was added to the arsenite solution in small aliquots over 1 h. After each repeated addition an off-white solid precipitate formed immediately. The reaction mixture was stirred for an additional 6 h, isolated by filtration, washed with water (200 mL), and acetone (100 mL), and allowed to dry in air. Yield = 0.508 g, 87%.

3.4.2.1 Characterization

DSC: small endotherm 81.56 °C $\Delta H = 28.3 \text{ J g}^{-1}$ (EtOH & H₂O), small endothermic peak 177.4 °C $\Delta H = 32.54 \text{ J g}^{-1}$ (melting point), broad endotherm 312.8 °C $\Delta H = 572 \text{ J g}^{-1}$

(decomposition); TGA: 4.7% 25-125 °C (H₂O), 71.28% 125-450 °C (decomposition); Raman (cm⁻¹): 637.8 (m, S-C), 382.8 and 361.8 (m, As-S); IR (cm⁻¹): 3337 (secondary NH), 3066 (m, aromatic C-H), 2962 (m, methylene C-H), 1647 (s, amide (C=O)), 1533 (NH); MS (+DP):427 (As₄S₄); ICP-OES: 3.2 (sulfur:arsenic ratio).

3.4.3 ABDT-As(III) Synthesis (1.5X ABDTH₂)

Sodium arsenite, NaAsO₂ (0.250 g, 1.92 mmol), was dissolved in water (50 mL). A solution of ABDTH₂ (0.947g, 2.53 mmol) in EtOH (50 mL) was added to the arsenite solution in small aliquots over 1 h. After each repeated addition, an off white solid precipitate formed within 2-5 minutes. The reaction mixture was stirred for an additional 6 h, acidified with 5% HCl, isolated by filtration, washed with water (200 mL), and acetone (100 mL), and allowed to dry in air. Yield = 0.598 g, 56%.

3.4.3.1 Characterization

Mp: 210-217 °C; IR: 3337 (broad, acid OH and secondary NH), 3066 (m, aromatic C-H), 2962 (m, methylene C-H), 1734 (s, acid (C=O)), 1647 (s, amide (C=O)), 1533 (NH); ICP-OES: 3.5 (sulfur:arsenic ratio).

3.4.4 ABDT-As(III) Synthesis (Excess As)

Sodium arsenite, NaAsO₂ (0.791 g, 6.10 mmol), was dissolved in water (50 mL). A solution of ABDTH₂ (0.501 g, 1.40 mmol) in EtOH (50 mL) was added to the arsenite solution in small aliquots over 1 h. After each repeated addition, an off-white solid precipitate formed immediately. The reaction mixture was stirred for an additional 6 h, acidified with 5% HCl, isolated by filtration, washed with water (200 mL), and acetone (100 mL), and allowed to dry in air. Yield = 0.462 g, 82%.

3.4.4.1 Characterization

DSC: broad endotherm 96.1 °C (EtOH and H₂O), sharp exotherm at 215.19 °C $\Delta H = 68.22 \text{ J g}^{-1}$, broad endotherm at 305.89 °C $\Delta H = 152 \text{ J g}^{-1}$ (decomposition); TGA: 8.22 % 30-180 °C (dehydration), 55.39% 180-420 °C (decomposition); Raman (cm⁻¹): 635 (S-C), 375 and 352 (S-As); IR: 3337 (broad, acid OH and secondary NH), 3066 (m, aromatic C-H), 2962 (m, methylene C-H), 1734 (s, acid (C=O)), 1,647 (s, amide (C=O)), 1533 (NH); MS (+DP): 427 (As₄S₄); ICP-OES: 3.3 (sulfur:arsenic mol ratio).

3.4.5 BDT-As(III) and ABDT-As(III) Soft Metal Preference Leaching

Both BDT-As(III) (0.101 g) and ABDT-As(III) (0.104 g) precipitates from section 3.2.1 were used for each leaching experiment. A stock aqueous mixed metal solution was prepared so that each individual metal was 100-200 ppb. Lead acetate trihydrate (45.8 mg, 0.121 mmol), cadmium chloride dihydrate (50.8 mg, 0.232 mmol), and mercury chloride (33.8 mg, 0.125 mmol) were dissolved in deionized water (500 mL). This solution (1 mL) was diluted with water (250 mL) and used for each leaching study. Small aliquots (5-10 mL) at time intervals of 12 and 24 h were collected from the solutions (50 mL), filtered at 0.2 μm (Nalgene syringe filters), and stored under nitrogen until analysis with ICP-OES. In addition, both BDT-As(III) and ABDT-As(III) precipitates were leached in metal-free deionized water (50 mL) for comparison.

3.4.6 BDTH₂ and ABDTH₂ Arsenate Interactions

Sodium arsenate heptahydrate (0.104 g, 0.334 mmol), was dissolved in water (500 mL). This solution (2.5 mL) was diluted to a total volume of 250 mL for the 5 ppm solution for both batch reactions. BDTH₂ (0.0915 g, 0.334 mmol) and ABDTH₂ (0.125 g, 0.334

mmol) in EtOH (50 mL) were added to separate 5 ppm arsenate solutions (100 mL) in small aliquots over 1 h. The reaction mixture was stirred for an additional 11 h. The EtOH was removed under vacuum, the solids were filtered by vacuum filtration, washed with water (200 mL), and allowed to dry in air. The filtrate was repeatedly filtered at 0.2 μm (Nalgene syringe filters). Excess EtOH was removed by heating at 90 $^{\circ}\text{C}$ for 2 hours followed by dilution with water to the original volume with 1% nitric acid for ICP-OES aliquots and DI water for IC aliquots. The solutions were stored under nitrogen until analysis with ICP-OES and IC.

3.5 Conclusions

BDTH₂ is a robust chelator of “soft” metal ions from aqueous solutions. The hypothesis that both BDTH₂ and the bidentate carboxylic acid derivative ABDTH₂ would be useful precipitation chelates for the removal of As(III) was confirmed. Both remove As(III) from aqueous solutions in high yield, >80%. Raman and IR spectroscopy confirm the formation of stable S-As(III) bonds. An evaluation of the thermal stability of BDT-As(III) and ABDT-As(III) shows each is relatively stable for filtration purposes. Also, both contain stable S-As bonds in ion-free aqueous solutions. Applications for targeting individual ions in solutions outside of laboratory controls may be difficult due to the dynamic equilibrium of covalent Metal-S bonds. Both BDTH₂ and ABDT₂ have unusual resistance to oxidation when mixed with As(V) in mixed aqueous solutions. Their insoluble products with As(III) make them ideal chelation compounds for areas such as the West Bengal region.

Chapter 4 Synthesis of ABDTH₂ Functionalized Silica Core-Shell Magnetite Nanoparticles

4.1 Introduction

Magnetic nanoparticles (MNPs) fit into the size range of 1-100 nm. Their applications are the focus of multidisciplinary scientific studies due to the high surface-to-volume ratio of nano-sized crystals, high magnetization in an applied magnetic field, and high surface energy.¹¹⁵⁻¹¹⁷ Magnetic nanoparticles generally smaller than 20 nm display superparamagnetic activity above certain blocking temperatures.¹¹⁵ Superparamagnetic nanoparticles behave as individual magnets¹¹⁵ Providing reproducible methods towards particles with very narrow size distributions is a synthetic focus. Superparamagnetic iron oxide nanoparticles (SPIONS) attract attention for applications involving biomedical applications due to biocompatibility and large magnetic moments.

116-118

MNPs are useful in a wide range of applications. These applications include the following: adsorption media, drug delivery, MRI contrast agents, catalysts, core-shells, hyperthermia, separations, and theranostics among many others.^{116-117, 119} Functional strategies often include interactions that prevent agglomeration and oxidation. For example, surface complexation with organic and inorganic groups can drastically alter stability.¹²⁰ Increased surface interactions become especially important as the size of the metal nanoparticles is reduced. Metal atoms exposed physically at the outer nanoparticle boundary show increased activity compared to bulk metal atoms. As such, agglomeration and coatings can alter the magnetization.¹²¹

This chapter will explore the chemistry and synthesis of magnetite, Fe_3O_4 , nanoparticles. Also, this chapter will evaluate functionalization strategies with MNPs and ABDTH₂. These potential strategies include core-shell attachment of ABDTH₂ through the bidentate carboxylic acid residues and as surface passivating groups directly attached to the particle surface.

4.1.1 Magnetite

Magnetite (Fe_3O_4) and maghemite ($\gamma\text{-Fe}_2\text{O}_3$) are ferrite colloids that form the basis of a broad range of MNPs.¹¹⁵ Both ferrites have spinel-type unit cells with oxygen atoms in a cubic close-packed arrangement. Regular spinel lattices have the composition AB_2O_4 where A is a divalent metal generally with an ionic radius of 80-110 Å. Examples of type A metals include Fe(II), Mn(II), Mg(II), and Cu(II).¹¹⁵ Type B metals are usually trivalent metals with an ionic radius of 75-90 Å. Examples of type B metals include Fe(III), Ti(III), and Al(III).¹¹⁵ The unit cell contains 32 oxygen anions in a close-packed cubic arrangement that forms 64 tetrahedral sites and 32 octahedral sites per unit cell forming $(\text{AB}_2\text{O}_4)_8$ formula units. In traditional spinels type A metals occupy 1/8 of the tetrahedral sites while type B metals occupy 1/2 of the octahedral sites. Interestingly, magnetite has an inverse-spinel unit cell where half the type B metals fill the tetrahedral sites and the other half fill the octahedral sites, while the type A metals fill only octahedral sites.¹¹⁵

Table 4.1 lists magnetic saturation (M_s) values of various magnetic materials. The ferrimagnetic properties of Fe_3O_4 are the result of two different interactions. The Fe(III) ions in the tetrahedral and octahedral sites in the lattice have opposing spin.^{116, 119} This interaction results in anti-ferrimagnetic super-exchange between Fe(III) cations and O^{2-}

anions. Here a spin-up 5d electron in $\text{Fe(III)}_{\text{Oh}}$ couples with an electron from O^{2-} in a 2p orbital reversing the spin.¹²² The other electron from O^{2-} in the second 2p orbital has an opposing spin to the first in O^{2-} . Thus the 5d electron in $\text{Fe(III)}_{\text{Th}}$ is spin-down and opposes the $\text{Fe(III)}_{\text{Oh}}$. The magnetic properties of Fe_3O_4 are due to the Fe(II) ions in the octahedral sites resulting from double-exchange interactions. Oxidation with atmospheric oxygen and other oxidizers can alter the stability of Fe_3O_4 MNPs. Oxidation results in the conversion of Fe_3O_4 to maghemite, $\gamma\text{-Fe}_2\text{O}_3$. The M_S of Fe_3O_4 MNPs varies over a broad range, 50-80 emu g^{-1} , which is lower than bulk phases at 92 emu g^{-1} .¹¹⁹ The oxidation to maghemite results in lower M_S due to the conversion of 2/3 of the $\text{Fe(II)}_{\text{Oh}}$ to $\text{Fe(III)}_{\text{Oh}}$ and increased vacancies. The bulk phase of maghemite has a M_S of 76 emu g^{-1} .

Table 4.1 Magnetic saturation values of various magnetic materials

| Material | M_S (emu g^{-1}) | Ref. |
|---------------------------|-------------------------------|------|
| Fe | 171 | 123 |
| Co | 143 | 123 |
| Ni | 48.5 | 123 |
| Fe_2O_3 | 76 | 124 |
| Fe_3O_4 | 92 | 122 |
| MnFe_2O_4 | 80 | 125 |
| CoFe_2O_4 | 75 | 126 |

The decrease in M_S for MNPs is due in part to the reduction in crystal size where the number of surface sites increases and inner bulk decreases.¹¹⁵ Small changes in

particle size below 10 nm have significant effects on the overall M_s . For example, MNPs with particle sizes of 7.8 and 9.4 nm increased M_s from 58.6 to 78.0 emu g^{-1} , respectively.¹²⁷ The reduction in individual crystal size below that of a single domain changes the magnetic behavior. In a typical magnetic hysteresis loop, the remanence is a measure of residual magnetization after removing an applied field to zero.¹¹⁵ Also, coercivity is a measure of the reverse applied field to reach zero. The remanence and coercivity usually found with traditional ferrimagnetic materials decrease as the number of exchange-coupled spins resisting spontaneous realignment decreases.¹¹⁵ This phenomenon as particle size decreases below certain thresholds leads to superparamagnetism. The estimated crossover for Fe_3O_4 nanoparticles from multi- to a single domain is below 128 nm.¹¹⁵ In comparison, Co(0) nanoparticles that adopt hexagonal close-packed (hcp) and cubic close-packed (ccp) unit cells convert to single domains below 15 and 7 nm, respectively.¹¹⁵ The conversion of Fe(0) nanoparticles to single domains occurs below 15 nm. Thus, Fe_3O_4 is predicted to exhibit superparamagnetic behavior over a greater size distribution than other common MNPs.¹¹⁵ In industry, High-Gradient Magnetic Separators (HGMS) that use large fields (up to 2 T) allow convenient removal of magnetic materials.⁶⁴

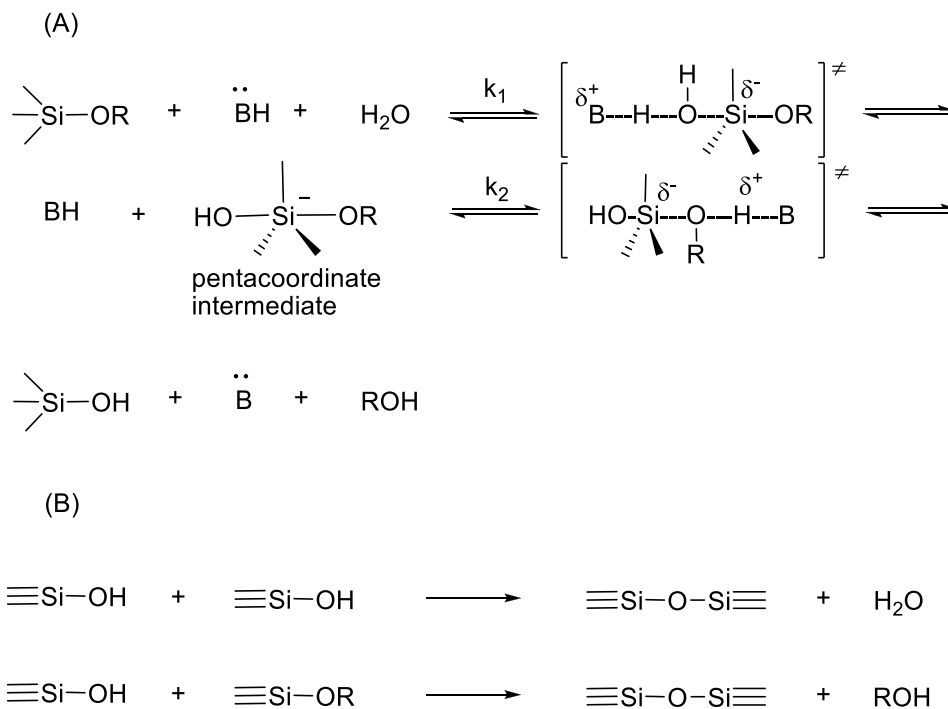
The stabilization of iron oxide nanoparticles is critically essential to their utility. The point of zero charge (PZC) of magnetite MNPs is pH 7-8.¹²⁸⁻¹²⁹ The stabilization and sedimentation/agglomeration are directly related to the surface charge of the nanoparticle.¹³⁰ Particles tend to sediment and agglomerate close to the PZC. Thus for magnetite, the PZC is very close to neutral conditions and is expected to form large agglomerates. The PZC of nanoparticles is controllable by surface passivation of small

molecules that carry negative or positive charges and have an affinity towards the nanoparticles surface.¹²⁸ Surface passivation with citric acid, oleic acid, and other surfactant molecules reduces agglomeration by altering the PZC.¹²⁸ Furthermore, citric acid stabilized magnetite nanoparticles help the formation of monodispersed core-shell strategies. Silica and alumina are common core-shell inorganic layers.¹²⁰ Without surface passivation such core-shell reactions result in large agglomerates reducing the high surface to volume ratio at the nanoscale.¹²⁸

This section will explore the co-precipitation of iron salts in the synthesis of magnetite nanoparticles or MNPs. For the remainder of this text, MNPs will be synonymous with magnetite nanoparticles. Also, the section will explore the aqueous stability of bare and citric acid-passivated MNPs.

4.1.2 Silica Core-Shell Chemistry

The Stöber method is common among surface coating techniques for the formation of nanometer-sized layers of silica.¹²⁰ This wet chemical process involves the hydrolysis and condensation of alkoxy silanes. Silica is made up of interlinked SiO₄ tetrahedra. The bond energy of Si-O in the molecular lattice of silicon dioxide is 452 kJ/mol. Silica formed by the sol-gel process is typically acid or base-catalyzed. The sol-gel process is a multistep reaction.¹³¹ Scheme 4.1 shows the generation of silica using the base-catalyzed sol-gel procedure. Nucleophilic attack by an oxygen atom of water to the silicon atom initiates hydrolysis. Deprotonation by the base results in a pentacoordinate intermediate that results in the concomitant elimination of an alcohol and formation of a silanol. Condensation occurs with the removal of water forming the condensed siloxane bonds from two silanols or a silanol plus an alkoxy silane.



Scheme 4.1 Base promoted sol-gel syntheses of alkoxy silanes: (A) hydrolysis (B) condensation¹³¹

The acid or base-promoted synthesis of sol-gels is not alkoxy silane specific. The two most common include tetramethoxysilane (TMOS) and tetraethoxysilane (TEOS).¹²⁰ Due to the low solubility of alkoxy silanes in water, the reaction is performed in EtOH or some other alcohol to promote the reaction. In the base-promoted sol-gel method the rate of condensation far outweighs that of hydrolysis resulting in highly branched polymeric networks creating bulkier polymers.¹²⁰ There are several ways to control the thickness and morphology of the silica sol-gel layer. For example, altering the MNP concentration, the ratio of ROH/H₂O, type of alcohol, and concentration of base results in different formations.¹³²⁻¹³³

Silica porous structures vary in particle size (nm to > micron), surface area (10 to >1000 m²g⁻¹), and pore volume (micro to mesoporous). As an example, commercial grade Kiesegel-60 had a BET surface area 495 m²g⁻¹, a pore diameter of 5.9 nm, and a BET pore volume of 0.9 m³g⁻¹.¹³⁴ Similarly, commercial grade Sylopol had a BET surface area of 330 m²g⁻¹, a pore diameter of 19 nm, and a BET pore volume of 1.7 m³g⁻¹.¹³⁴ Silica-coated magnetite has a variable porous structure dependent on the thickness of the coating and morphology. For example, the surface area of silica core-shell MNP ranges from 30 to > 500 m²g⁻¹.^{120, 132} Values of BET surface area of silica by the Stöber method are inconsistent. BET values often deviate outside the geometric surface area of non-porous particles.¹³⁵ Pore characteristics often vary by reaction time, washing solvent, and outgassing temperature.

Siloxane and silanol groups cover the surface of silica in multiple ways. Figure 4.1 shows the different types of surface silanols. Isolated silanols contain a surface silicon atom with three siloxane bonds. Vicinal silanols occur at adjacent silicon surface atoms each having a silanol linkage. Geminal silanols include two silanols connected to the same silicon surface atom.¹³⁴

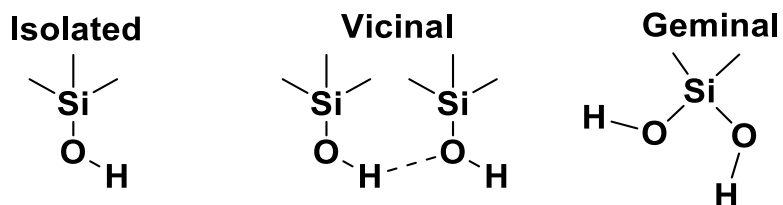
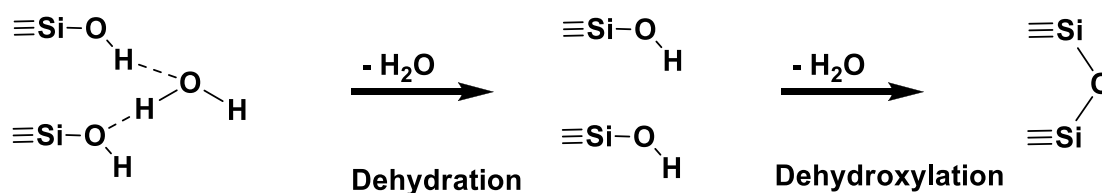


Figure 4.1 Different silica silanol groups

The surface density of the silanol groups can be determined by several different methods including TGA, ²⁹Si CPMAS NMR (cross-polarization magic-angle spinning),

and IR Fourier transform DRIFT spectra.^{134, 136} The distribution of isolated, vicinal, and geminal silanols is random for amorphous silica. Several hydration layers also cover the surface via hydrogen bonded water molecules. The determination of surface silanol concentration using TGA is a cheap and quick procedure.¹³⁴ However, distinguishing dehydration from dehydroxylation (silanol) is somewhat controversial due to the ambiguous nature of the evolving gas (water).¹³⁵ For example, the complete dehydration temperature ranges from 200-380 °C.¹³⁶ The high temperature of dehydration indicates that the waters are strongly bound to the silica surface and pores. However, a slow ramping thermogram correctly measured the silanol concentration in comparison with NMR results.¹³⁴ This assumes the surface is completely devoid of any potential organic or inorganic contaminants. Scheme 4.2 displays the different step transitions when heating silica. Deuterium-exchange showed the silanol number of totally hydroxylated silica ranges from 4.2 to 5.7 SiOH nm⁻² regardless of the origin and structural characteristics of the silica. In comparison, TGA of untreated or rehydroxylated silica by acid treatment showed a concentration of 4.3 to 6.7 SiOH nm⁻².¹³⁴



Scheme 4.2 Heat treatment of silica

This section will explore the synthesis of silica core-shell MNPs and critically evaluate the surface structure and properties. The silica core-shell should provide thermal and oxidative protection for the magnetite core.

4.1.3 APTS Attachment to Silica

Organosilanes can functionalize the amorphous phase of silica to provide different reactive groups and properties. As an example, 3-(aminopropyl)triethoxysilane (APTS) and 3-(mercaptopropyl)triethoxysilane (MPTS) are common organosilanes among silica core-shell functionalization strategies.¹³⁷ The primary amine and sulfhydryl groups can serve as specific substrates or as coupling reagents. Thus this allows further functionalization with molecules to target specific applications.¹²⁰ However, functionalization with organosilanes suffers from several drawbacks. These drawbacks include unwanted hydrogen bonding, vertical and horizontal polymerization, and disorder.¹³⁸

Industrially, aminosilane modifications typically use water-EtOH mixtures with silica gels. Water hydrolysis of the alkoxy groups produces silanols. An advantage of using aminosilanes is their stability towards unwanted polymerization. Enhanced stability results from the formation of an intramolecular seven-membered ring. Figure 4.2 shows the proposed cyclic hydrogen bonded form and an internal zwitterion form.¹³⁹ The zwitterion form results from a proton transfer of the silanol group to the amine. The $pK_a = 10.7$ for the terminal amine in APTS. Surface silanols are more acidic than the APTS silanols reducing polymerization.¹⁴⁰ The thermodynamically favored process results in immobilization of APTS, through the silanols, to the silica surface.¹³⁸

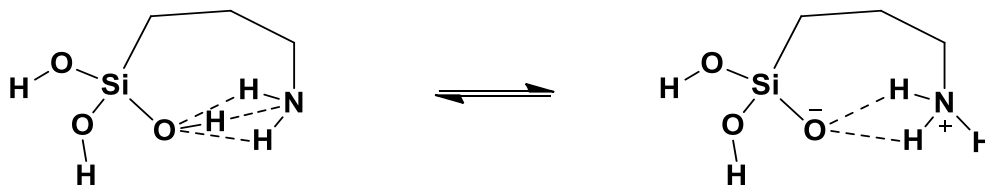
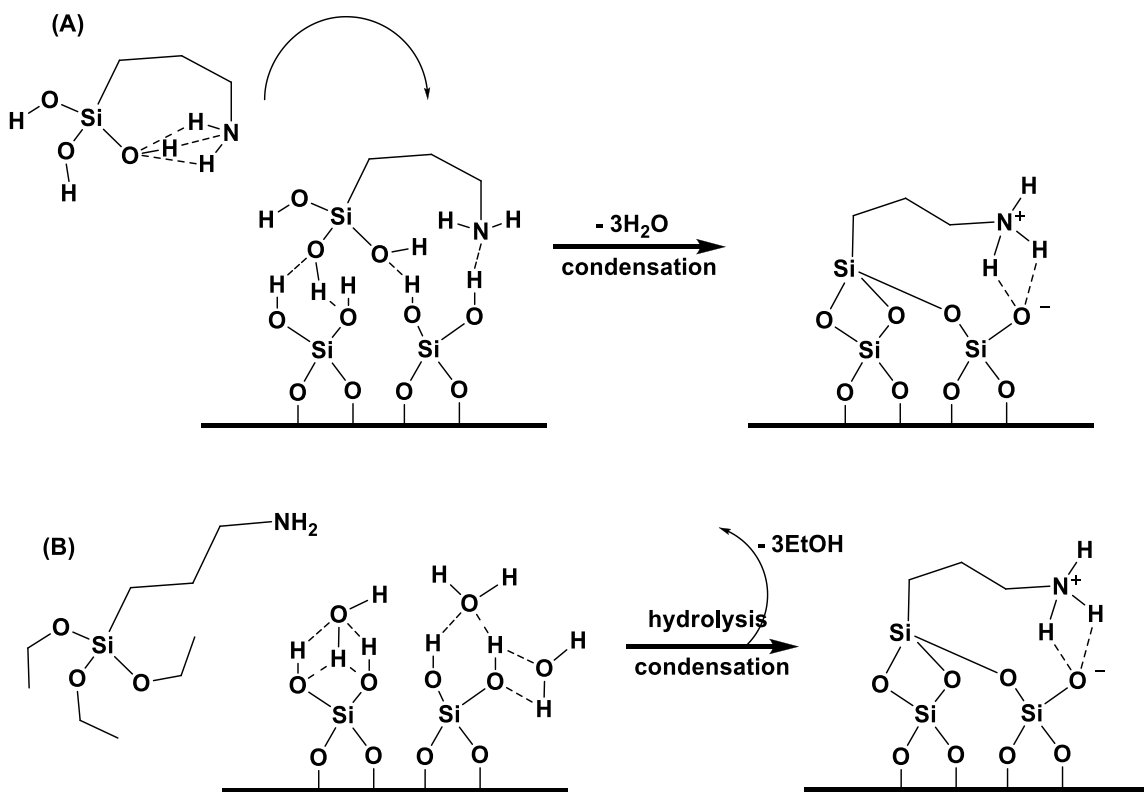


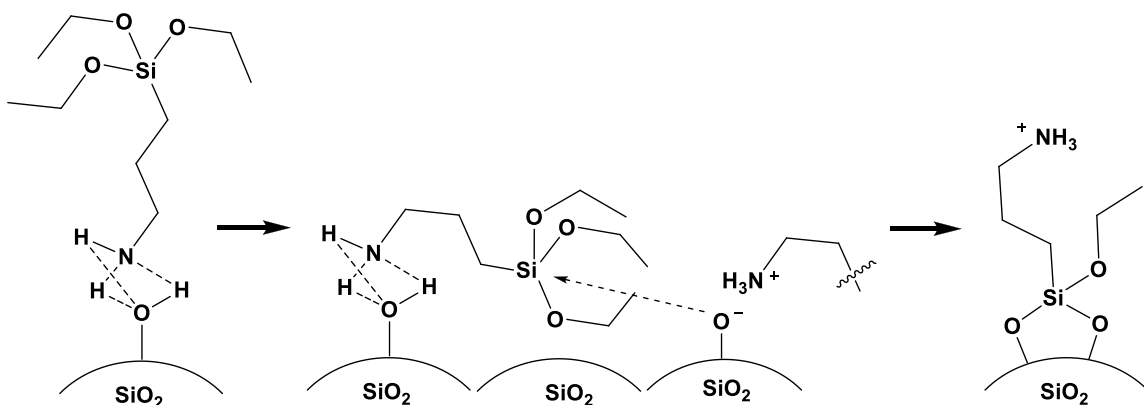
Figure 4.2 Seven-membered APTS ring in aqueous solution

Immobilization of APTS in dry organic solvents results in better loadings and reproducibility.¹⁴¹ The most common solvent for the reaction is toluene.¹³⁸ In water, the hydrolysis occurs immediately in solution. In a dry organic solvent with hydrated silica, the hydrolysis of the alkoxy groups only forms at the surface. Immediate condensation of the silanol to the bridging siloxane then forms.¹³⁹ Thus hydrolysis and polymerization are minimized in dry organic solvents. Scheme 4.3 shows immobilization in aqueous conditions (A) and a dry organic solvent (B).



Scheme 4.3 (A) APTS in water (B) APTS in dry organic solvent with hydrated silica¹³⁹

The orientation of the amine group of APTS is important for the immobilization to form readily.¹³⁸ Hydrogen bonding to the silica surface is responsible for fast APTS adsorption. Also, proton abstraction by surface silanol leads to electrostatic stabilization of the amine.¹³⁸ Thus the hydrogen bonding amines help catalyze the condensation forming the siloxane linkages that are free to orient away from the surface. Scheme 4.4 shows the “flip mechanism” interaction with APTS and the silica surface.



Scheme 4.4 Flip mechanism for APTS¹³⁹

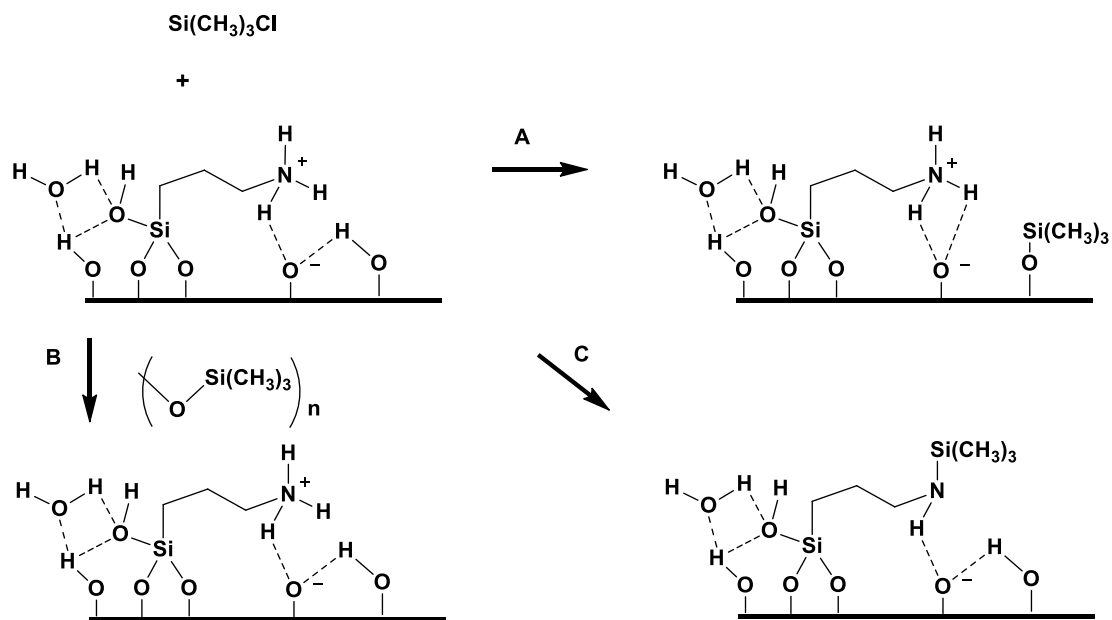
The section will explore APTS functionalized silica core-shell MNPs. Here the focus is to determine the yield in comparison to the concentration of surface silanol groups and fully characterize the surface properties.

4.1.4 Silanol Interaction with Chlorotrimethylsilane

Interestingly there is little fundamental research investigating the protection of surface silanols previously functionalized with organic molecules. Due to the changes in solubility and reactivity this area is important for the overall utility of the intended application.¹⁴² Protection allows for increased solubility in organic solvents that may find

extensive use in catalytic transformations.¹⁴² Also, protection may block equilibrium-based adsorption for the removal of inorganic ions from solution. Here such a surface functionalized with ABDTH₂ allows for sequestration of ions predominantly through sulfhydryl groups. However, removing potential adsorption sites is non-ideal regarding cost, recyclability, and removal capacity.

Different pathways can result from the addition of chlorotrimethylsilane. Each assumes incomplete immobilization of all surface silanols during the loading of APTS. Washing the APTS functionalized silica surface with dilute acid should protonate the terminal amine of APTS, as the hydrochloride salt $\text{-NH}_3\text{Cl}$, lowering the nucleophilicity of the amine. However, interactions might still be possible. The reaction in a dry organic solvent with hydrated silica should react similarly to the same conditions with APTS. Hydrolysis of chlorotrimethylsilane at the surface allows for condensation with the surface silanols.¹³⁹ This assumes that the surface hydration shell is not very thick and that hydrolyzed trimethylsilanol is close enough in proximity to the surface. Another scenario may involve nucleophilic attack of the protonated ammonium ion of APTS. The third scenario may involve hydrolysis of the chlorotrimethylsilane and subsequent polymerization in solution. Scheme 4.5 shows all three scenarios. This section will explore silanol protection, and compare functionality to the free silanol analog.



Scheme 4.5 Chlorotrimethylsilane pathways: (A) silanol protection (B) polymerization (C) APTS interaction

4.1.5 $\text{ABDT}_2@\text{MNPs}$

Post-synthetic modification of nanoparticles is a common technique to introduce desired functionalities. A broad variety of organic functional groups can passivate the surface of nanoparticles. For example, carboxylic acids, phosphates, amines, and sulfhydryl groups among others have preferential interactions with a broad range of nanoparticle surfaces.¹²⁰ For MNPs, carboxylic acid stabilization is the most common choice of capping ligand.⁷⁰ For example, citric acid, oleic acid, and other surfactant molecules coordinated to the surface reduce agglomeration by altering the PZC.¹²⁸ Surface passivation creates a “dense molecular rug.”¹⁴³ The organic component can dictate changes in solubility, reactivity, and magnetism.¹⁴⁴ Also, a dynamic equilibrium exists between the capping ligand, particle surface, and other ligands in solution. Surface

exchange is a common technique that allows modifying pre-stabilized surfaces. Typically surface passivation by ligands occurs immediately after nanoparticle formation.

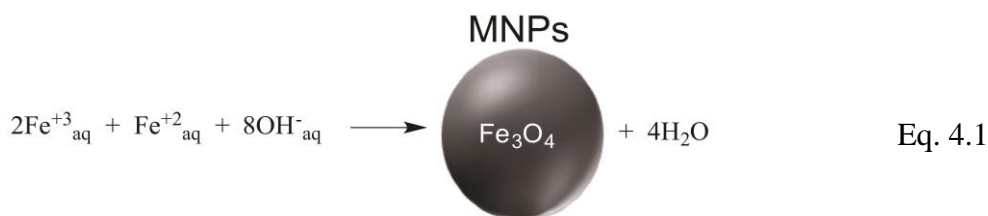
This section will explore the stabilization of MNPs with ABDTH₂. The bidentate carboxylic acid groups should provide stabilization in solution by altering the PZC. In this way, ABDTH₂ can participate in S-As(III) bond formation while stabilizing the MNP surface. The MNPs are also capable of binding As(III) through inner and outer sphere adsorption.⁶⁴ Thus this is a double-edged sword approach to the removal process. Both components are capable of interactions with As(III) in some capacity.

4.2 Results and Discussion

4.2.1 ABDTH₂ Core-Shell MNPs

Magnetite (Fe₃O₄) MNPs were synthesized by the chemical co-precipitation of Fe(II) and Fe(III) salt solutions treated with ammonium hydroxide. Co-precipitation is the most common method due to reaction time, cost, and narrow size distributions.¹¹⁵

Equation 4.1 shows the general reaction stoichiometry for the synthesis of MNPs.



The ease in isolation using an applied magnetic field, here with computer hard drive magnets, is a useful utility. The average particle size determined by TEM was 11 ± 3 nm (polydispersity = 0.220). The XRD spectrum contained peaks at 2^θ = 30, 36, 43, 53, 57,

and 63. These peaks indexed to the cubic inverse spinel Fe_3O_4 and were present throughout the stepwise functionalization reactions. The IR spectrum of the MNPs contained absorptions at 3500-3000, 1632, and 570 cm^{-1} . These were due to hydrogen bonded water on the MNP surface, O-H bending from water, and the Fe-O bond, respectively. A nitrogen isotherm analysis determined the BET surface area, pore volume, and pore radius were 73.48 $\text{m}^2 \text{g}^{-1}$, 0.2227 $\text{cm}^3 \text{g}^{-1}$, and 6.06 nm, respectively. These isotherm results compare similarly with other MNPs using the co-precipitation method.¹⁴⁵

The thermogravimetric analysis (TGA), with a custom method, for all combined functionalized MNPs was characterized from 25-1000 °C. This method was adopted to elucidate water of hydration. TGA for the as-synthesized magnetite showed a mass loss of 1.851% up to 100 °C corresponding to 18.51 $\text{mg H}_2\text{O g}^{-1}$ or 1.03 $\text{mmol H}_2\text{O g}^{-1}$. A sharp weight loss at 511 °C corresponding to 1.189 % occurred due to the phase transformation of γ -maghemite to hematite.¹⁴⁶

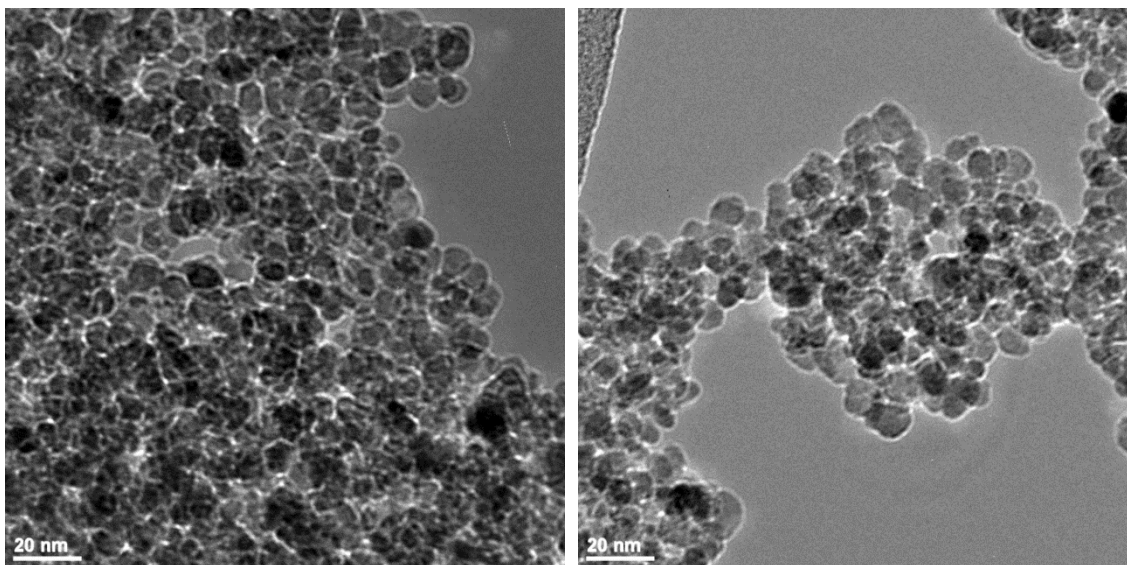
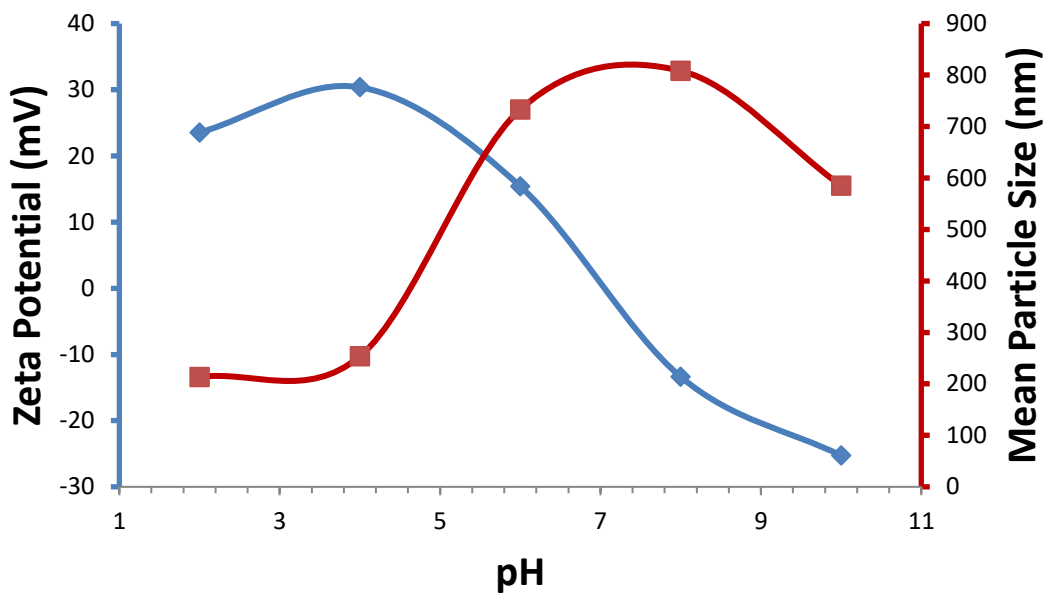


Figure 4.3 TEM images of uncoated magnetite nanoparticles

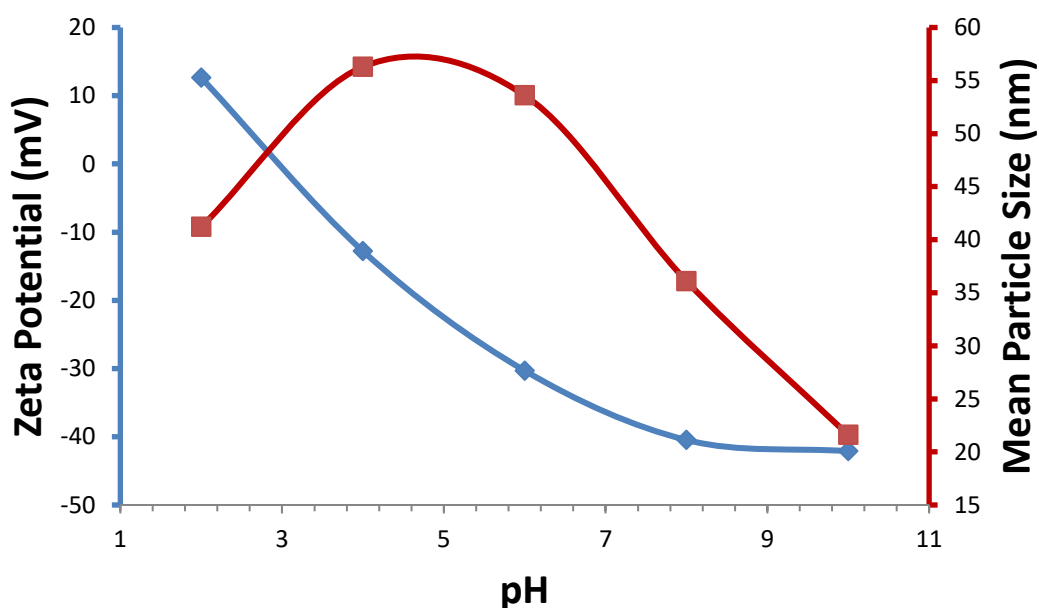
During the isolation of MNPs repeated washing steps were done to neutralize the alkalinity of the medium. One major disadvantage of uncoated magnetite MNPs is their instability towards agglomeration near the PZC. Magnetite has a PZC around 7-8.¹²⁹ Thus magnetite MNPs are predicted to form undesirable products in the pH range for which they are to be utilized as solid supports. Sonication and heat treatments are alternate methods, but have proven to be less effective and may lead to oxidation of Fe(II).¹⁴⁷ The zeta potential and particle size by dynamic light scattering (DLS) determined the PZC of uncoated MNPs to be 7.2, within the literature value of 7-8, and suffered from inter-particle agglomeration (Figure 4.3). The results show a strong correlation between the zeta potential and mean particle size. Overall, at pH values close to the PZC the largest agglomerates occur, and at either more positive or negative zeta potentials, the mean particle size is reduced. This trend is due to the electrostatic repulsion between particles that are either positive or negative. These results compare to similar trends in particle size vs. pH and for the PZC of magnetite at pH 7.9.¹⁴⁸



Graph 4.1 Zeta Potential (blue) and mean particle size (red) for raw MNPs

Surface passivation with small molecules capable of altering the surface charge through surface coordination stabilizes MNPs.¹²⁸ Citric acid-coated MNPs were also formed by the co-precipitation method. Immediately after the first decanting of the aqueous solution, the particles were dispersed in a 0.1 M solution containing trisodium citrate. The zeta potential of citrate MNPs was negative from pH 4-10 with a PZC at 3.05, which compares to the 1st pK_A of 3.15 for citric acid. Agglomeration was mitigated with particle size ranging from 21.6- 56.3 nm from pH 2-10. These results are comparable to those found for similar citrate coated MNPs. However, some have recorded negative zeta potentials over the entire pH range examined.¹²⁸ The IR spectrum of the resulting citrate coated MNPs indicated surface coverage by citrate groups. Two strong IR absorptions were observed at 1576 cm⁻¹ and 1384 cm⁻¹ characteristic of the asymmetric and symmetric stretches of the citrate carboxylate groups, respectively. In comparison, the carboxylate groups in neat sodium citrate were observed at 1580 and

1416 cm^{-1} , respectively. TGA also supports surface coverage by citrate groups. There were three significant mass loss regions. These mass loss events correspond to dehydration, loss of CO and CO_2 , and additional release of CO_2 .¹⁴⁹ Overall, the additional mass lost between the raw MNP and the citrate-coated MNP was 27.23% at 800 °C.



Graph 4.2 Zeta Potential (blue) and mean particle size (red) for citrate MNPs

Silica core-shell MNPs were synthesized via a base-promoted sol-gel reaction with TEOS. Early attempts at small core-shell MNPs resulted in mixed morphologies with large silica core-shells that tended to agglomerate. These initial attempts were with raw MNPs where agglomeration had been shown to occur over a wide pH range. Figure 4.4 shows TEM images of the products of these sol-gel reactions. The images reveal an agglomerated polymer-like network of interconnected silica core-shells containing

random distributions of MNPs. Several different synthetic methods were investigated to promote more homogenous core-shell structures. The reaction was attempted with constant sonication, but the results were similar, and the heat from sonication led to oxidation of Fe(II) ions in the MNPs. Microemulsion techniques have greater control of the silica core-shell growth, but they rely on expensive organic solvents and harsh reducing agents.¹⁵⁰

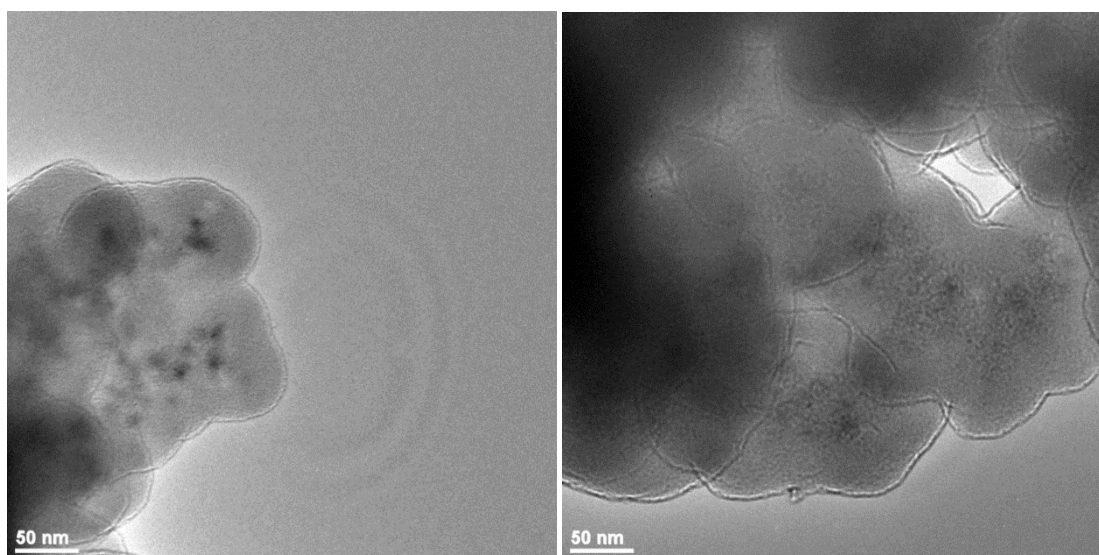


Figure 4.4 Silica core-shell images from raw MNPs

Citrate MNPs promote homogenous core-shell structures due to the stabilization of the negatively charged surface groups. There is a strong correlation between the concentration of citrate and the formation of agglomerated products.¹²⁸ Thus citrate MNPs were chosen as an ideal candidate to improve the efficiency of the core-shell MNPs. The IR spectrum of the silica core-shell MNPs confirmed the formation of the silica network. The asymmetrical Si-O-Si stretching absorption was at 1060 cm^{-1} . Absorptions at 942 and 800 cm^{-1} are due to Si-OH bending and in-plane Si-OH (geminal)

bends, respectively. There was no significant peak associated with citrate compared to the citrate coated MNPs. Figure 5.4 shows TEM images of the silica core-shell MNPs derived from citrate MNPs. The average core-shell radius determined by TEM was 55 ± 10 nm. Importantly, many of the viewable particles on the TEM grid were monodisperse, and the agglomerated silica core-shell structures were not present. Many of the particles contained single magnetic cores. The core-shells that did contain multiple MNPs were of similar size and morphology to the single MNP core analogs. The BET surface area was $125.49 \text{ m}^2 \text{ g}^{-1}$ with a pore volume and radius of $0.2692 \text{ cm}^3 \text{ g}^{-1}$ and 4.29 nm , respectively. The BET surface area for a 2nd batch used for the i-ABDTH₂ MNPs was $71.1 \text{ m}^2 \text{ g}^{-1}$ with a single point volume and radius of $0.9439 \text{ cm}^3 \text{ g}^{-1}$ and 2.66 nm , respectively. These results compare to the BET surface area of the raw MNPs, $73.48 \text{ m}^2 \text{ g}^{-1}$ and $96.8 \text{ m}^2 \text{ g}^{-1}$, for the 1st and 2nd batch. The same experimental conditions were used for both the 1st and 2nd batch of silica MNPs. However, the drying temperature was increased from 80 to 160 °C under vacuum. Also, the de-gas temperature was increased from 120 to 190 °C prior to isotherm analysis. There are large differences observed in the surface area of core-shell MNPs depending on the method of silica formation.¹⁵¹ In general, silica core-shells prepared with sodium silicate as the precursor instead of alkoxysilanes have higher surface area.¹⁵² The accepted surface silanol group density of 4-7 sites nm^{-2} fits within the BET and TGA results for the sample with $125.49 \text{ m}^2 \text{ g}^{-1}$. The gradual mass loss of 1.210% from 380-1000 °C corresponds to $1.42 \text{ mmol SiOH g}^{-1}$ or $6.83 \text{ SiOH nm}^{-2}$. The 2nd batch used for the i-ABDTH₂ MNPs contained $1.003 \text{ mmol SiOH g}^{-1}$ or $8.49 \text{ SiOH nm}^{-2}$ which is slightly higher. However, amorphous silica contains random distributions

of isolated, geminal, and vicinal silanols which are uncontrollable and may factor into the increased mass.

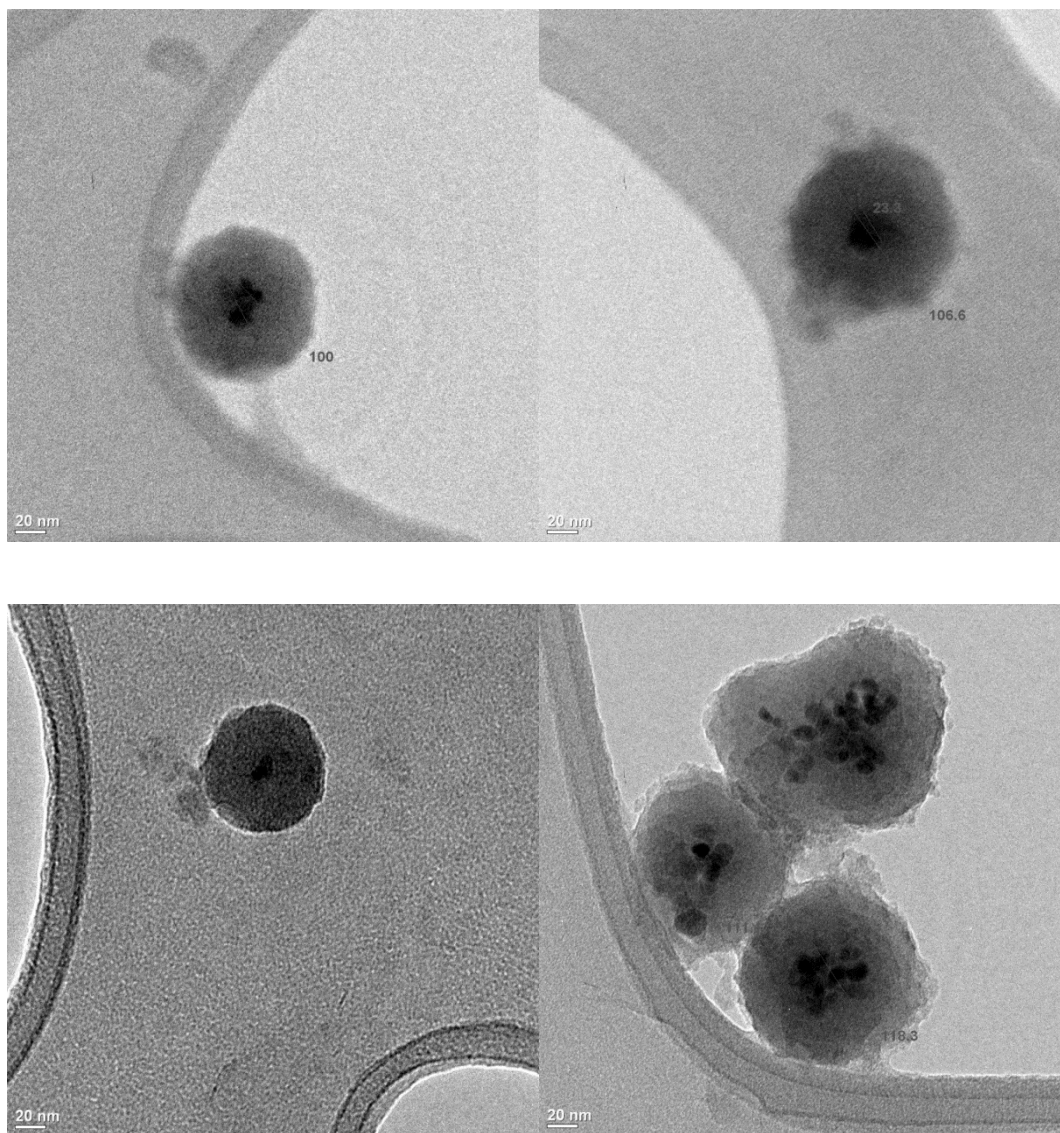
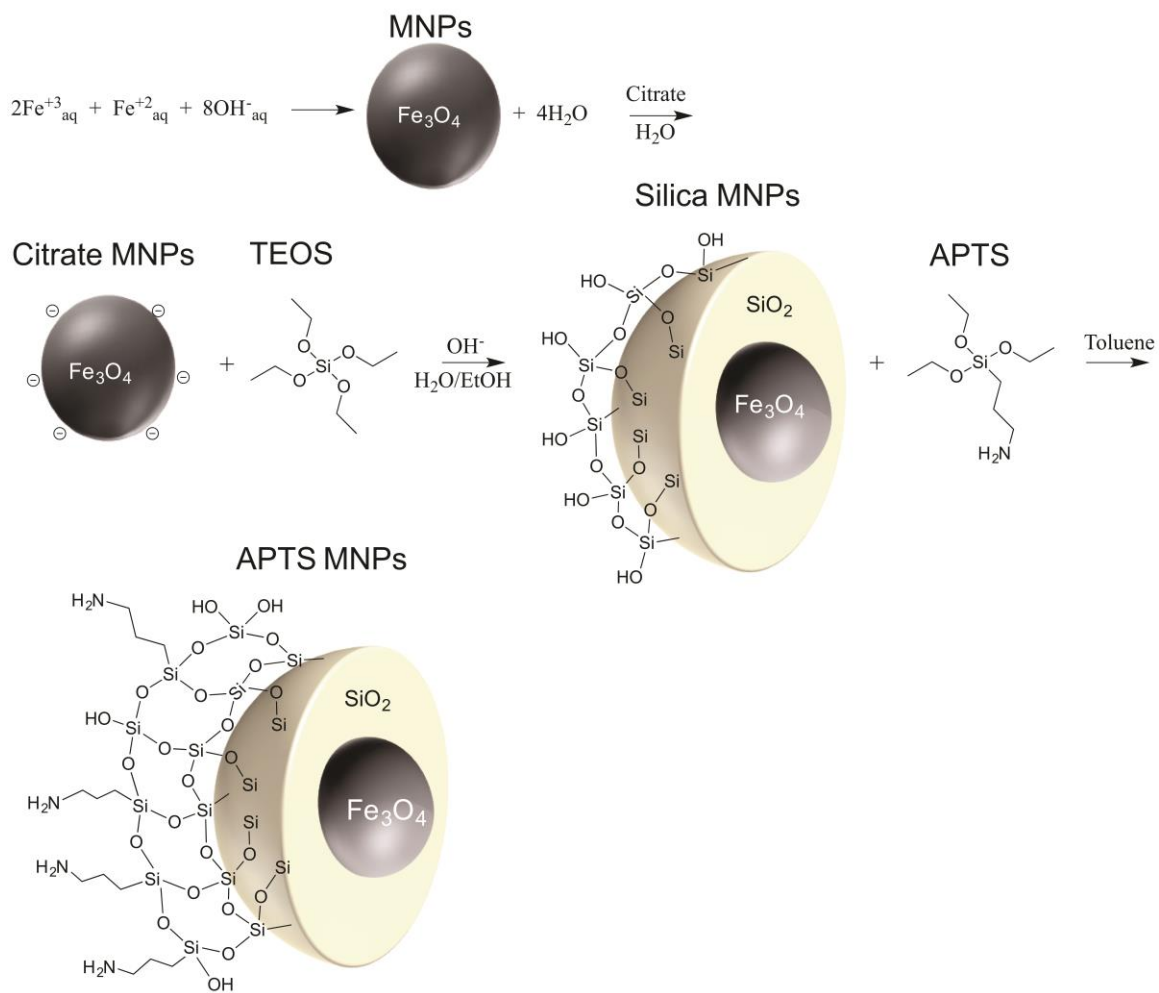
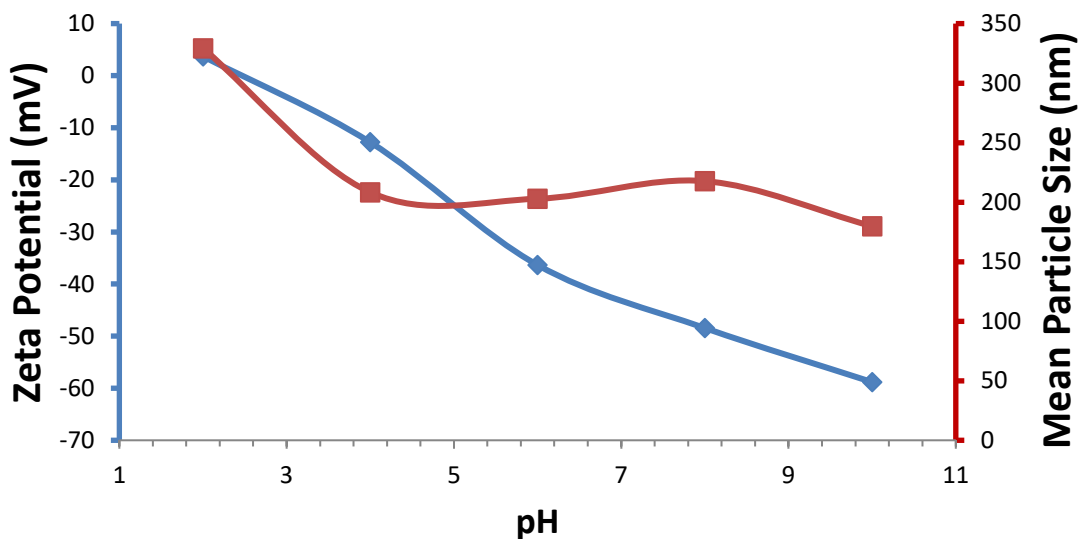


Figure 4.5 TEM images of silica core-shell MNP



Scheme 4.6 Reaction pathway for the synthesis of APTS MNPs

The PZC of the silica core-shell MNPs was determined to be 2.4 and close to the literature value, ~2, with potentials greater than -30 mV from pH 6-10. Particle size determined by DLS ranged from 208.0-179.8 nm from pH 4-10. Thus the silica core-shell MNPs are predicted to be stable in pH values similar to groundwater where the utility of the core-shell MNP will find future use.¹²⁸



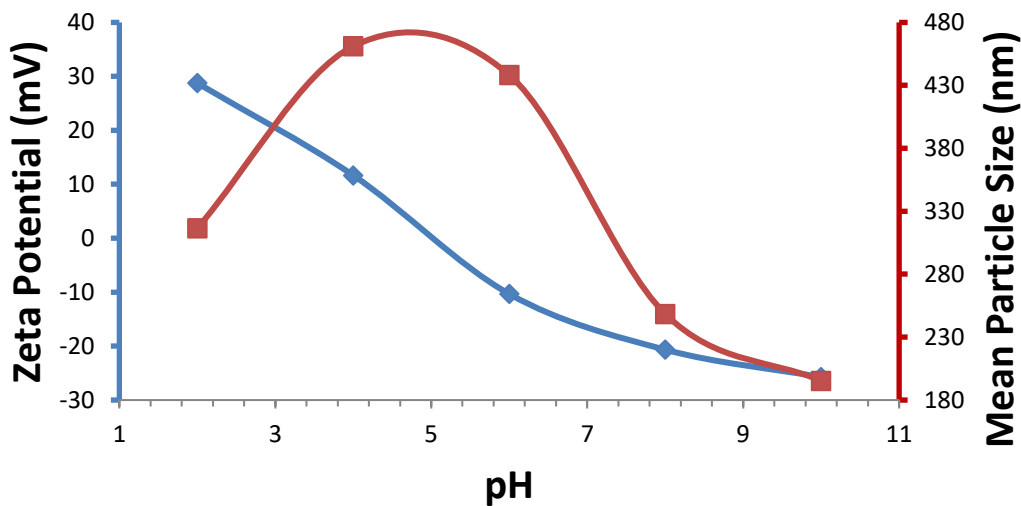
Graph 4.3 Zeta potential and mean particle size for silica core-shell MNPs

Amine functionalization with (3-aminopropyl)triethoxysilane (APTS) was formed by reflux in dry toluene. The silica core-shell MNPs were not completely dehydrated so that hydrolysis and condensation of APTS could occur directly at the silica surface. The IR spectrum of the material showed all the characteristic absorptions for the silica-core-shell MNP. There were additional absorptions at 2981, 2941, and 1541 cm^{-1} assigned to sp^3 hybridized C-H stretching and N-H scissor from APTS, respectively. The PZC of APTS MNPs was determined to be 5.2 and shifted from a value of 2.4 for silica core-shell MNPs. This value compares similarly to other APTS derivatives where the PZC was between 5-7.¹³⁷ The shift in the PZC is further proof that APTS has been immobilized on the surface, and gives insight to the protonated state of the amine functional group. APTS functionalization also resulted in a net gain in particle size growth ranging from 461-196 nm between pH 2-10 with the largest aggregates near the PZC.

Elemental analysis was done to determine the nitrogen content present from APTS. EA showed a nitrogen concentration of 1.62%. Thus the concentration of APTS on the silica core-shell MNP was 1.157 mmol APTS g⁻¹. The APTS concentration compares to the 1.47 mmol SiOH g⁻¹ available on the silica surface calculated from TGA. This represents an overall yield of 78% for a 1:1 silanol condensation ratio per mol APTS. However, there is some error involved in the calculation of the actual silanol concentration for the silica core-shell MNP due to ambiguous nature of the thermogram. A second batch used for the *i*-ABDTH₂ MNPs had a nitrogen concentration of 1.48 % with 1.06 mmol g⁻¹ APTS. This represents an overall yield of 100 % for a 1:1 SiOH per APTS ratio. The horizontal and vertical growth of APTS as multilayers is a possible explanation for the high yields.

Three distinct mass losses occurred from 200-1000 °C. TGA-GC-MS has determined the evolving gas products with APTS functionalized directly on MNPs.¹⁵³ These mass loss events are due to the loss of water and ammonia and decomposition products of the carbon backbone. These carbon products include the following: ethane, CO₂, acetaldehyde, aziridine and cyclobutanone. Overall the total mass lost from 100-1000 °C was 19.182 % or an additional 10.77 % compared to the previous silica core-shell MNPs. In comparison to EA with 1.157 mmol APTS g⁻¹, the additional mass loss assuming the change resulted from cleavage of the C-Si bond releasing NH₂CH₂CH₂CH₂ results in 1.85 mmol APTS g⁻¹. The overestimation by TGA is likely due to additional mass loss from uncondensed ethoxy groups. Monodentate, bidentate, and tridentate structures are each possible on the SiO₂ surface. However, the carbon, hydrogen, and nitrogen concentrations determined by EA support monodentate formation. The

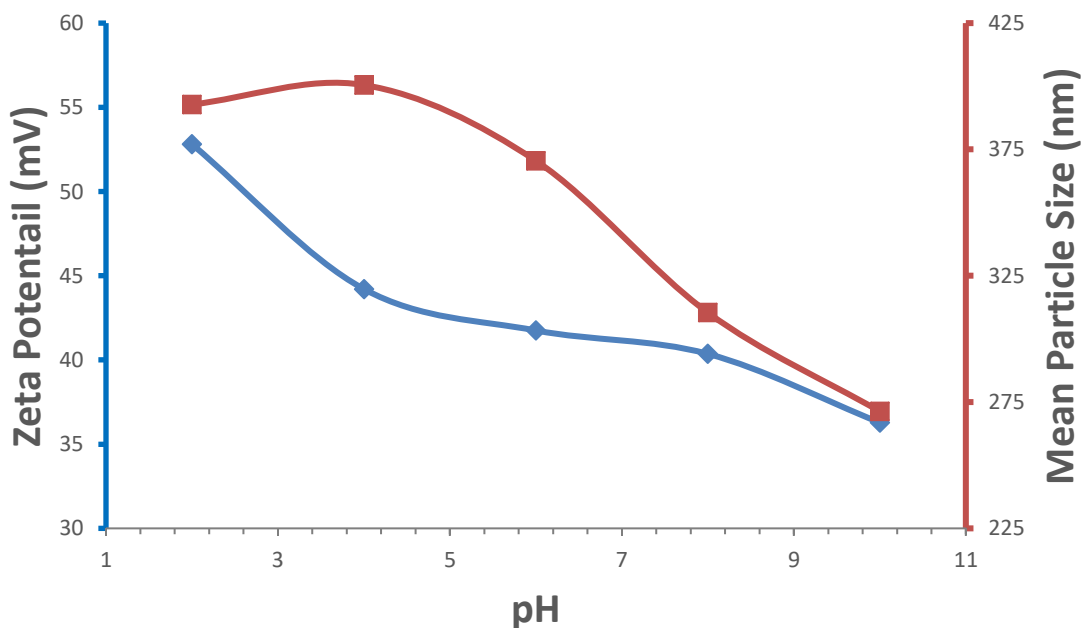
theoretical C, H, N ratio 6:1.3:1 for APTS with two ethoxy groups compares to the measured ratio 6.2:1.4:1. Including the additional mass in the TGA weight loss equates to 0.921 mmol g⁻¹ APTS which is much closer to the concentration determined by EA. The 2nd batch used for the i-ABDTH₂ MNPs had an additional mass loss of 11.86 % compared to the silica MNPs. This corresponds to 1.03 mmol APTS g⁻¹ for the monodentate complex. This value agrees well with the 1.06 mmol APTS g⁻¹ determined by EA.



Graph 4.4 Zeta potential and mean particle size analysis of APTS MNPs

The interaction of free surface silanols with chlorotrimethylsilane and the overall effect on the utility of the composite was investigated. The APTS MNPs were first washed with dilute hydrochloric acid and dried. The dried APTS MNPs were stored open to air for one week prior to the experiment. The amount of the chlorotrimethylsilane loading was half of the potential silanol surface concentration, 0.71 mmol g⁻¹ SiOH. The IR spectrum for the TMS MNPs compared similarly to the APTS MNPs. There was a small increase in intensity and broadening of the absorption between 2981 and 2941 cm⁻¹.

Two large mass losses occurred between 200-450 °C and 500-800 °C corresponding to 10.45 and 11.31 %, respectively. The previously mentioned gas products are expected to be among those lost plus the addition of methane or methyl radicals from the CH₃ groups in the trimethylsilane. Overall, there was an additional mass loss of 2.95 % compared to APTS MNPs. Assuming the increased mass corresponds to the cleavage of the C-Si bond releasing three methyl groups equates to 0.656 mmol TMS g⁻¹. This calculated value compares similarly to half of the silanol density calculated previously, 0.71 mmol SiOH g⁻¹. The PZC was not determined due to negative potentials for the pH range. The potentials ranged from 56-36 mV with particle the size from 391-271 nm across the pH range of 2-10. The zeta potentials are strikingly different from the APTS MNP zeta potentials. These results support that surface silanols were indeed protected via the trimethylsilane condensation.



Graph 4.5 Zeta potential and DLS results for TMS MNPs

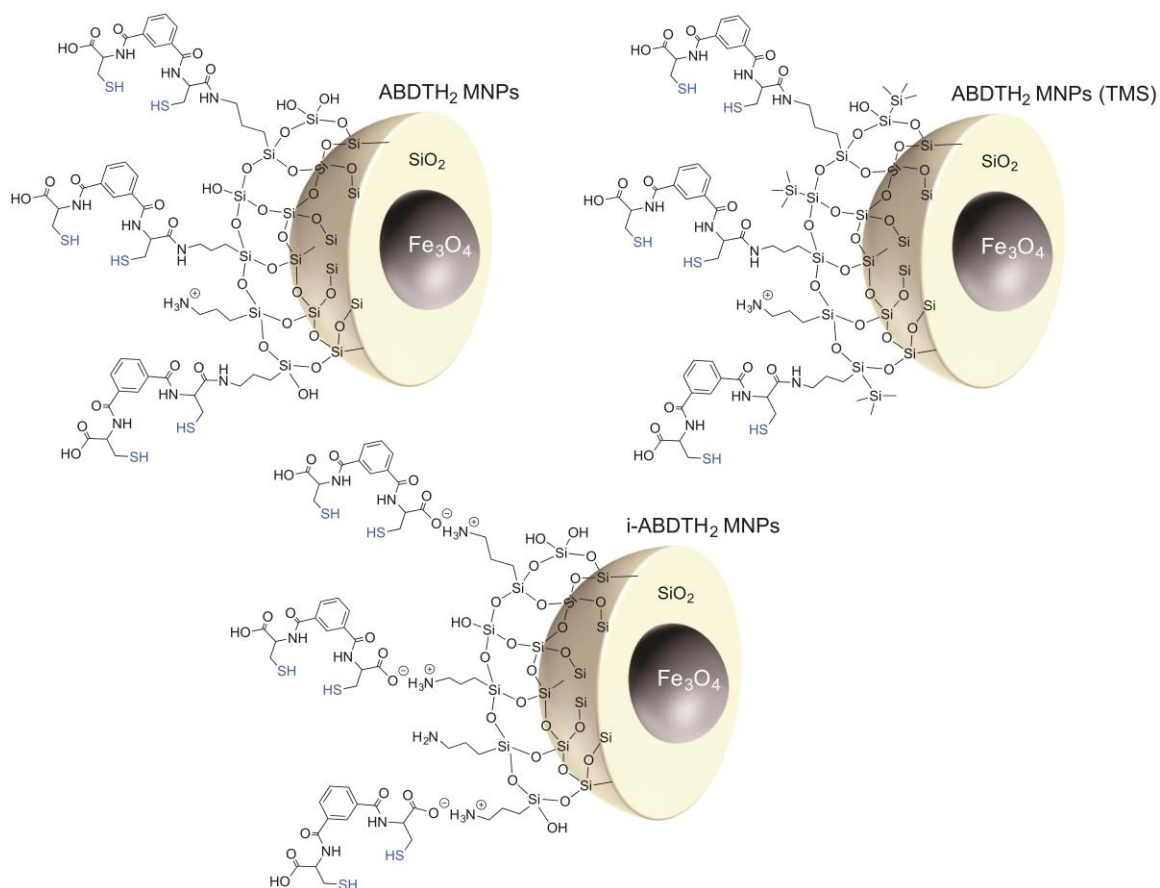


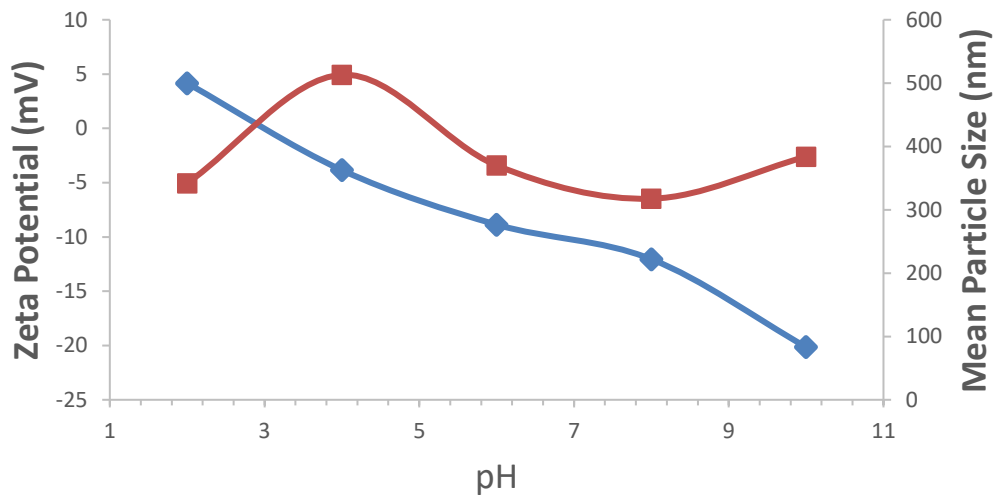
Figure 4.6 Ideal surface composition for split-view structures of ABDTH₂, ABDTH₂ (TMS), and i-ABDTH₂ MNPs

The coupling of ABDTH₂ to APTS MNPs and TMS MNPs was done via EDC. Prior to the reaction, both APTS MNPs and TMS MNPs were treated with 3 equivalents of triethylamine and briefly dried to deprotonate the primary amine of APTS. Several successful coupling reactions of molecules containing both carboxylic acid and free sulfhydryl groups with primary amines have been reported.^{65, 154-157} For example, thiosalicylic acid and the hydrochloride salt of amino acids afforded the coupled N-2-mercaptobenzoyl-amino acids with DBTU and DIEA in DMF. Cysteamine coupled to carboxylic acids stabilized on quantum dots with EDC resulted in amide bond formation.

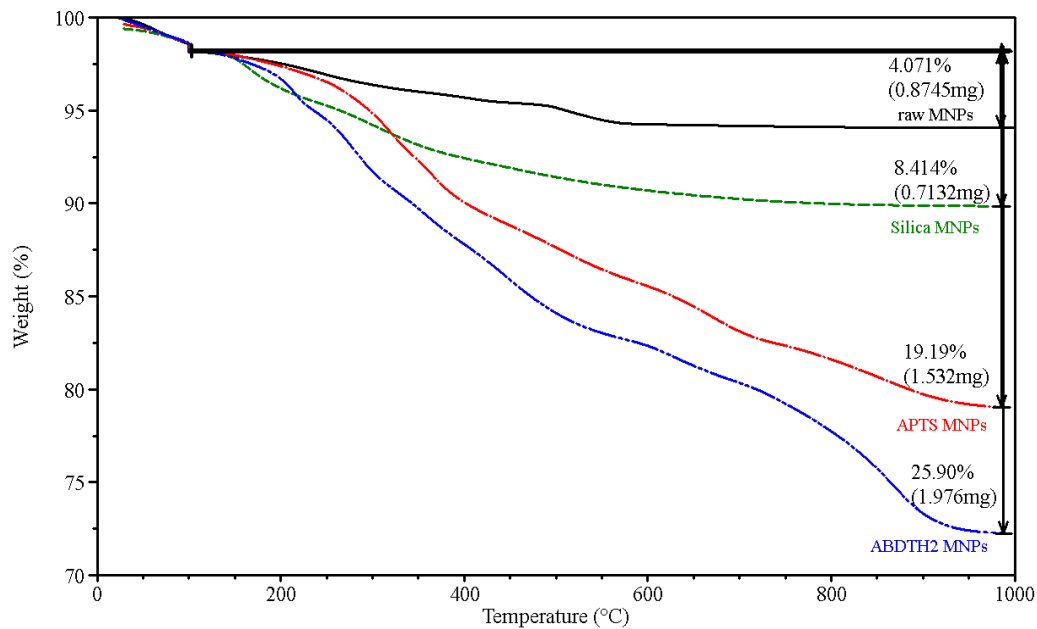
Also, L-cysteine with free sulfhydryl groups coupled to nanoparticles with EDC resulted in amide bond formation. Oxidized dithiol formation upon aqueous workup is a limiting issue for all three examples. Reduction with DTT was necessary to liberate the free sulfhydryl groups. However, N-glutathione coupled to 2-D graphene oxide with EDC by amide bond formation showed efficient removal of As(III) and Pb(II) without the need for reducing the SH of glutathione. Here, 4-dimethylaminopyridine (DMAP) was used to promote carboxylic acid activation, and DTT was used in later subsequent steps to help avoid oxidized dithiols.

The IR spectrum of ABDTH₂ MNPs contained similar absorptions to ABDTH₂. Increased absorption of the sp³ C-H was observed between 2976-2893 cm⁻¹. Importantly, a weak sulfhydryl band was observed at 2542 cm⁻¹. The amide (C=O) vibration was observed at 1639 cm⁻¹ with peak broadening. The acid carbonyl (C=O) vibration was assigned to the absorption at 1733 cm⁻¹, but the overall intensity of the peak was much weaker relative to the amide (C=O) in raw ABDTH₂. The PZC of ABDTH MNPs was 3, with the particle size ranging from 342-390 nm across the pH values. The previous trend in stability with zeta potential was not as apparent from the results. The PZC compares similarly with the results from citrate MNPs, 3.1, stabilized by the carboxylate groups. Two distinct mass losses occurred from 200-1000 °C. The mass loss products are expected to consist of the previously mentioned gases from prior steps with additional decomposition products related to ABDTH₂. Due to the similarity in structure with cysteine the decomposition of ABDTH₂ products should consist of H₂S, CO₂, SO₂, CO₂, and N₂. The overall mass loss after the isothermal equilibrium was 25.53%. The ABDTH₂ MNPs had an additional 6.37 % overall mass loss compared to APTS MNPs.

Graph 4.7 shows the TGA for all ABDTH₂ MNP synthetic steps. Assuming the mass lost resulted from complete decomposition of the additional ABDTH₂, this results in 0.172 mmol g⁻¹ ABDTH₂.

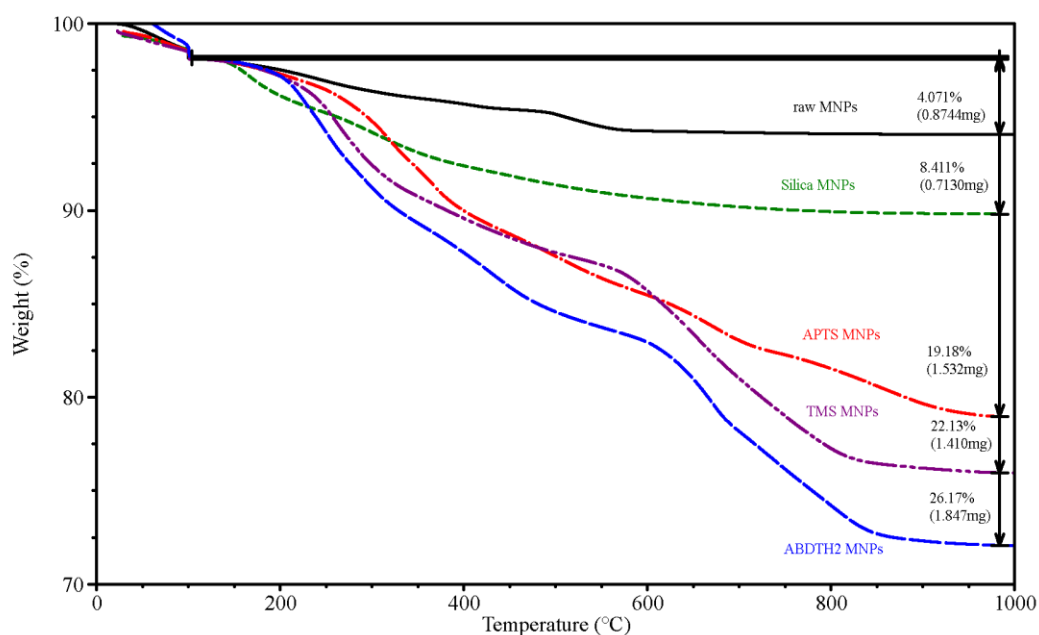


Graph 4.6 Zeta potential and mean particle size analysis of ABDTH₂ MNPs



Graph 4.7 TGA results raw MNPs (black, solid), silica MNPs (green, short dash), APTS MNPs (red, dash dot), and ABDTH₂ MNPs (blue, broken double)

Similar mass losses for ABDTH₂ MNPs (TMS) were observed compared to ABDTH₂ MNPs. Two significant mass losses occurred between 200-500 °C and 600-850 °C. The ABDTH₂-MNPs (TMS) had an additional 4.04 % mass loss compared to the APTS MNPs (TMS). Graph 4.8 shows the TGA results for all synthetic steps for ABDTH₂ MNPs (TMS). Assuming the mass loss resulted from complete decomposition of ABDTH₂, corresponds to 0.109 mmol g⁻¹ ABDTH₂.



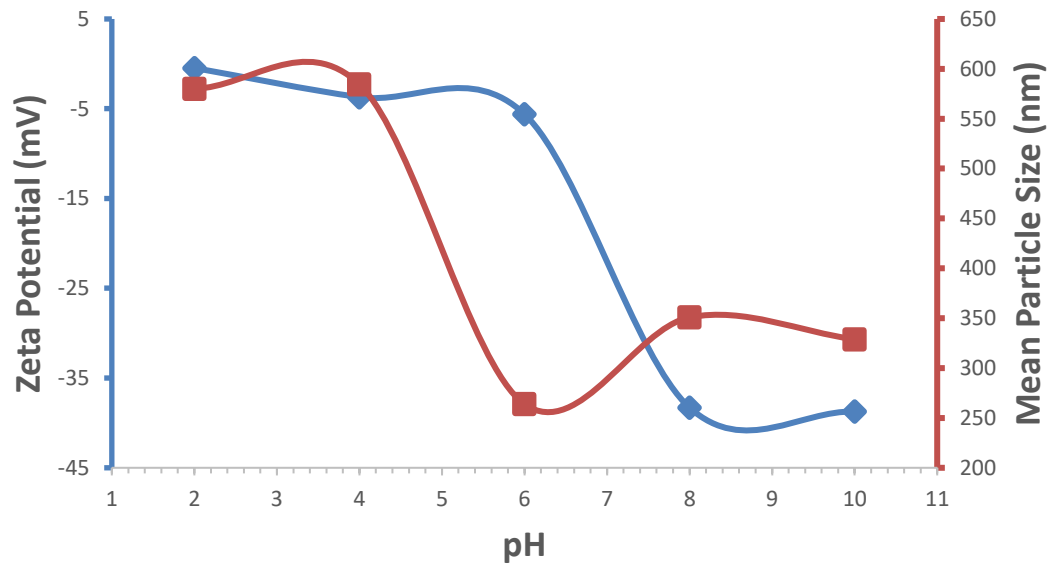
Graph 4.8 TGA for silica MNPs (red), APTS MNPs (green), TMS-MNPs (violet), ABDTH₂ MNPs (blue)

The ABDTH₂ loadings on the coupled MNPs were determined by ICP-OES. ABDTH₂ was digested in aqueous media in the presence of a strong acid and peroxide to break down organic content present on the surface. The loading of ABDTH₂ MNPs was 0.283 mmol S g⁻¹ or 0.142 mmol ABDTH₂ g⁻¹ which corresponds to a yield to N content of 25 %, and a surface density of 0.68 ABTH₂ groups nm⁻². The loading for ABDTH₂

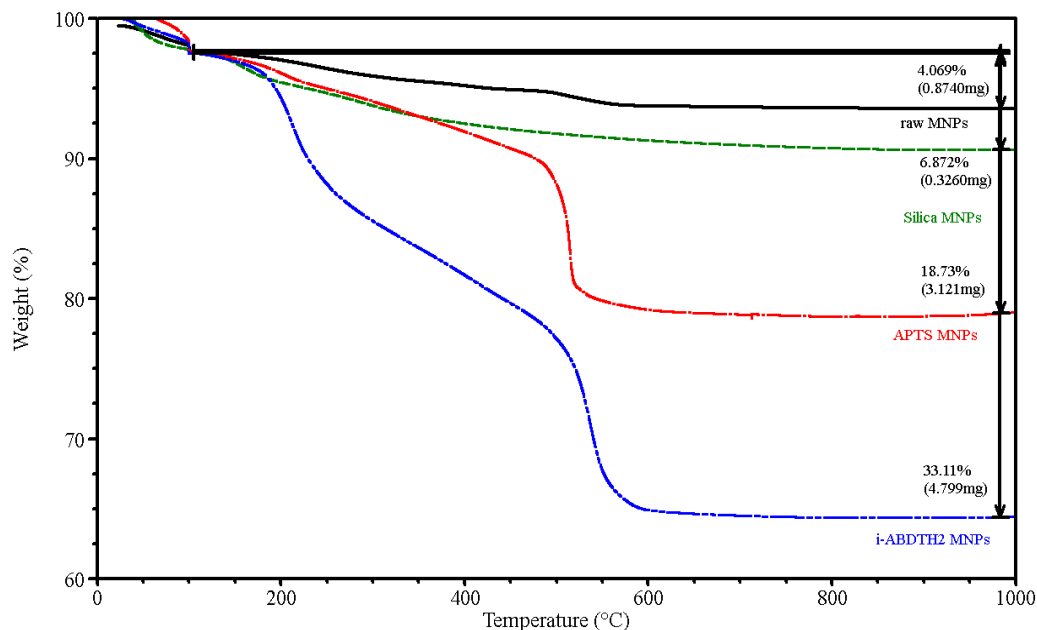
MNPs (TMS) was $0.232 \text{ mmol S g}^{-1}$ or $0.116 \text{ mmol ABDTH}_2 \text{ g}^{-1}$. This corresponds to a yield to N content of 21%, and to a surface density of $0.55 \text{ ABTH}_2 \text{ groups nm}^{-2}$. The results from ICP-OES with $0.142 \text{ mmol g}^{-1} \text{ ABDTH}_2$ are slightly lower than predicted by the mass loss in TGA with $0.172 \text{ mmol g}^{-1} \text{ ABDTH}_2$. A possible explanation for the small overestimation is due to residual DMF. The ICP-OES results for the (TMS) MNPs with $0.116 \text{ mmol ABDTH}_2 \text{ g}^{-1}$ compares very similarly to TGA results with $0.109 \text{ mmol g}^{-1} \text{ ABDTH}_2$. These reactions were repeated numerous times with similar low loading of ABDTH_2 . Much higher loadings, 8.4 mmol Cys , were recovered on similar nanoparticles.¹⁵⁷ The low yield may be the result of inefficient activation of the carboxylic acid groups of ABDTH_2 in DMF. EDC coupling is much faster in aqueous buffers where pH is modified to deprotonate the acid. Because of its problematic environmental impact, DMF is problematic, and a non-ideal choice for functionalization of the MNPs for later use in water treatment. Unfortunately, solvent compatibility with ABDTH_2 was rather limited.

The loading of i- ABDTH_2 MNPs was done by refluxing APTS MNPs with ABDTH_2 in EtOH. Here the loadings were much higher compared to the coupled composites. Importantly, this is by far the cheapest route that doesn't require expensive coupling agents or DTT. Also, this method avoids the health risks associated with DMF. There were two major mass losses between $150\text{-}250$ and $390\text{-}630$ °C corresponding to 13.72 and 18.64 %, respectively. The additional mass loss of 14.38% compared to the 2nd batch of APTS MNPs results in a loading of $0.386 \text{ mmol ABDTH}_2 \text{ g}^{-1}$. ICP-OES determined the loading of $0.612 \text{ mmol S g}^{-1}$ or $0.306 \text{ mmol g}^{-1} \text{ ABDTH}_2$. This corresponds to a yield to N content of 59%, and to a surface density of $2.6 \text{ ABDTH}_2 \text{ nm}^{-2}$.

². The IR spectrum had identical peaks for those of ABDTH₂ with the addition of increased broadening at 1530 and 1390 cm⁻¹ due to the carboxylate ionically stabilized with the quaternary ammonium ions of APTS, respectively. There was no observed PZC. The potentials were all negative, and particle size ranged from 264-329 nm from pH 6-10.

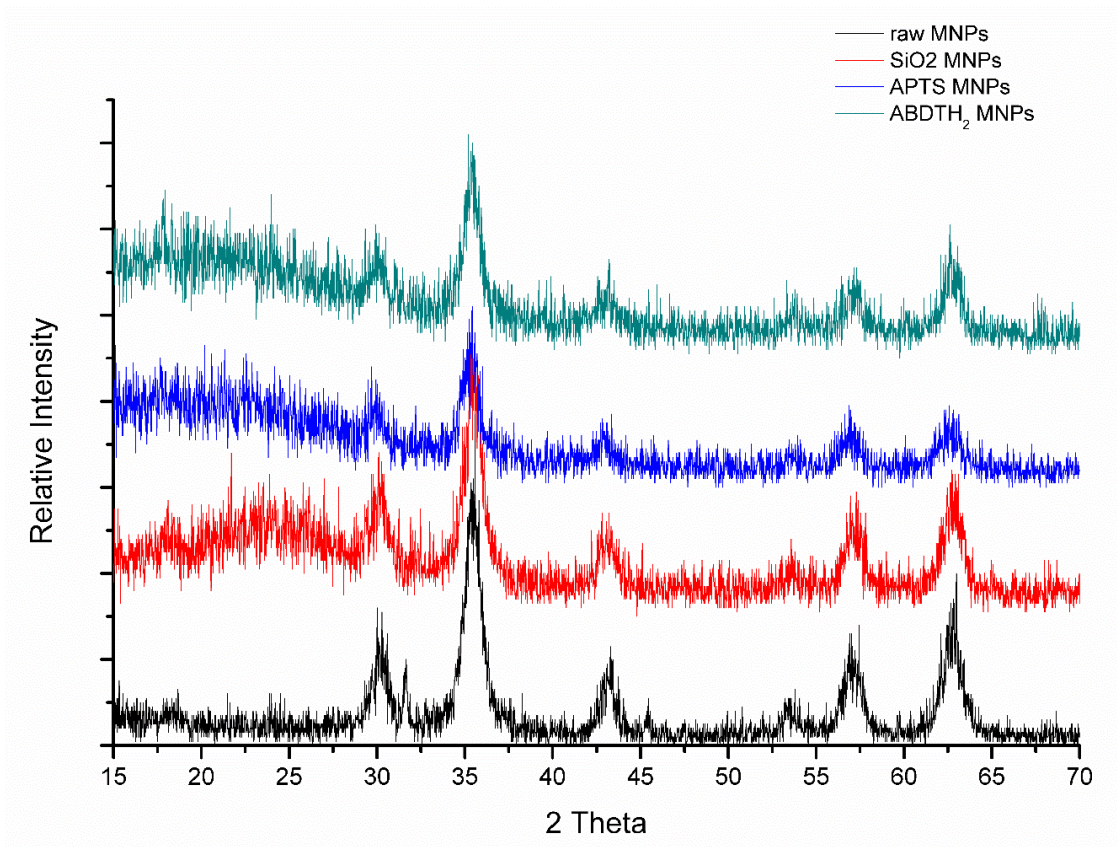


Graph 4.9 Zeta potential and mean particle size analysis of i-ABDTH₂ MNPs



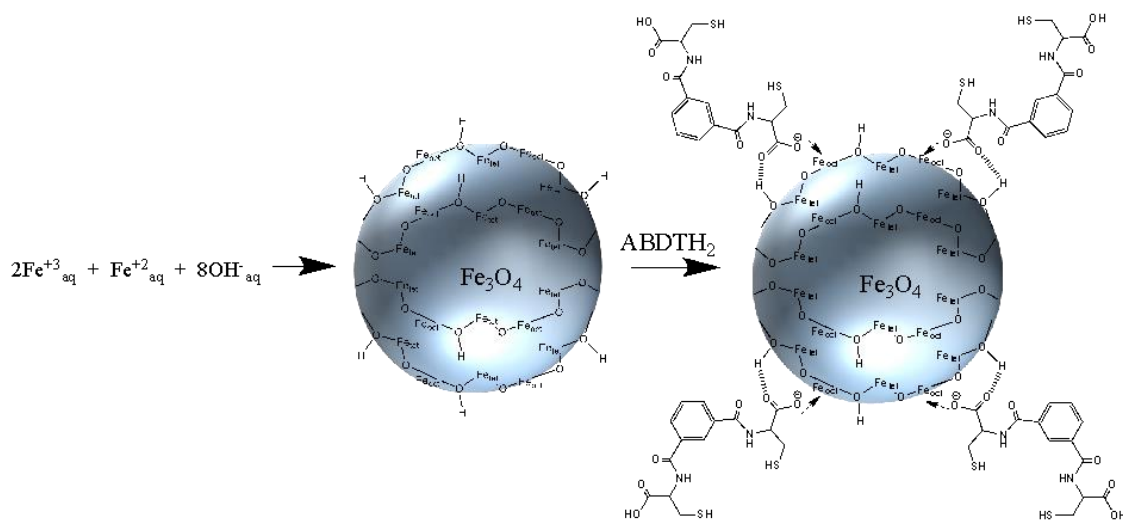
Graph 4.10 TGA results raw MNPs (black, solid), silica MNPs (green, short dash), APTS MNPs (red, dash dot), and i-ABDTH₂ MNPs (blue, broken double)

The XRD spectrums for all the subsequent prior steps are displayed in Graph 4.11. XRD analysis of raw MNPs displayed peaks at $2\theta = 30, 36, 43, 53, 57,$ and 63 which were all indexed to cubic inverse spinel Fe_3O_4 . Importantly the peaks for the MNPs were retained throughout the subsequent core-shell and functionalization reactions. The amorphous silica core-shell was also confirmed with broad increases at $2\theta = 20$. Peak lowering and broadening did occur with each added functionalization to the MNP core. The XRD spectrum for the i-ABDTH₂ MNPs was identical to ABDTH₂ MNPs and not shown for clarity.



Graph 4.11 XRD of raw MNPs (black), silica MNPs (red), APTS MNPs (blue), and ABDTH₂ MNPs (green)

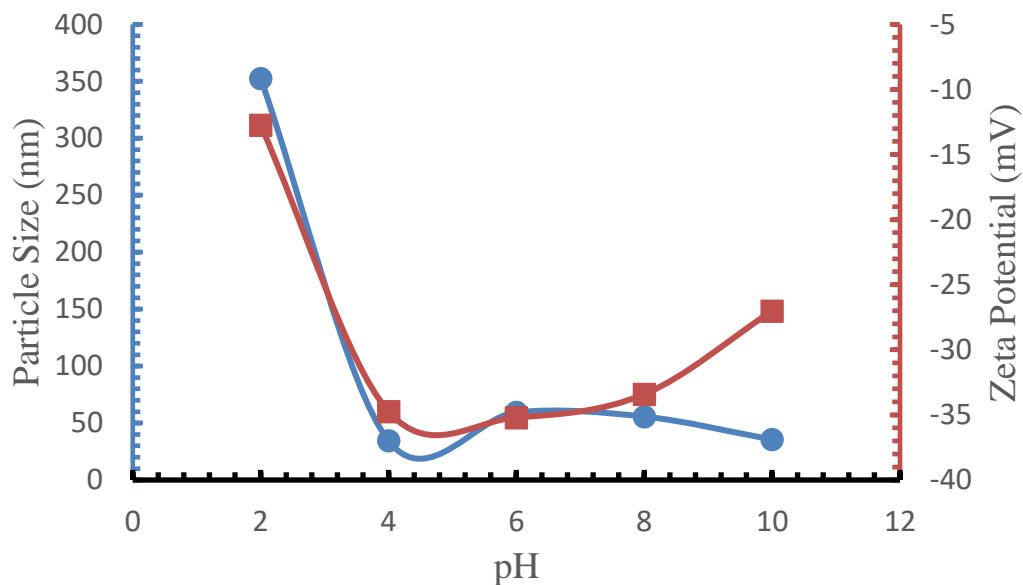
4.2.2 Surface Stabilized ABDTH₂@MNP



Scheme 4.7 Synthesis of ABDTH₂ stabilized MNPs

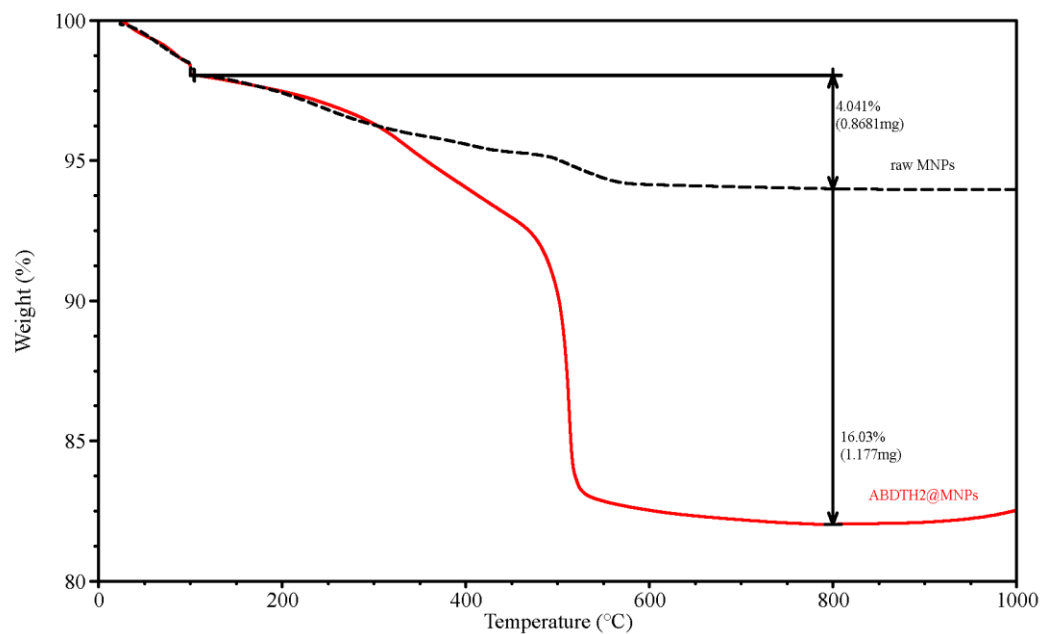
Surface stabilized ABDTH₂@ MNPs were synthesized similarly to the citrate MNPs. Scheme 4.7 shows the formation of ABDTH₂@MNPs. The MNPs were dispersed with a 0.1M solution containing ABDTH₂ at pH 5 and allowed to stir for one hour at 50 °C. The IR spectrum of ABDTH₂@MNPs contained a wide band from 3500 cm⁻¹ to 2900 cm⁻¹ due to hydrogen bonding from water on the MNP surface. The aromatic C-H stretching, sp³ C-H stretching, and thiol absorptions were located at 3062, 2884, and 2539 cm⁻¹, respectively. The carboxylate absorptions were observed at 1570 and 1365 cm⁻¹ indicating surface stabilization by the acid groups of ABDTH₂. The potentials were negative across the pH range. This compares to the i-ABDTH₂ MNPs that were also negative from pH 2-10. The particle size ranged from 35-60 nm from pH 4-10. Large agglomerates were avoided with ABDTH₂@MNPs above pH 4. Similar results were seen with previous citrate MNPs. The BET surface area of ABDTH₂@MNPs was 78.0

$\text{m}^2 \text{g}^{-1}$. Thus there was a 20 % reduction compared to the BET surface area of bare MNPs of $96.8 \text{ m}^2 \text{g}^{-1}$.



Graph 4.12 Zeta potential and particle size results for ABDTH₂@MNPs

The TGA of ABDTH₂@MNPs confirmed surface coverage. There were two large mass losses between 200-800 °C. The decomposition of ABDTH₂ products should consist of H₂S, CO₂, SO₂, CO₂, and N₂ due to the similarity in structure with cysteine. There was an additional 11.99% mass loss compared to bare MNPs corresponding to 0.322 mmol ABDTH₂ g⁻¹. The i-ABDTH₂ MNPs also contained two major mass loss events between 150-250 and 390-630 °C. ICP-OES determined a loading of 0.461 mmol S g⁻¹ or 0.230 mmol ABDTH₂ g⁻¹. This concentration compares similarly with the increased i-ABDTH₂ MNPs loading due to non-covalent surface coverage.

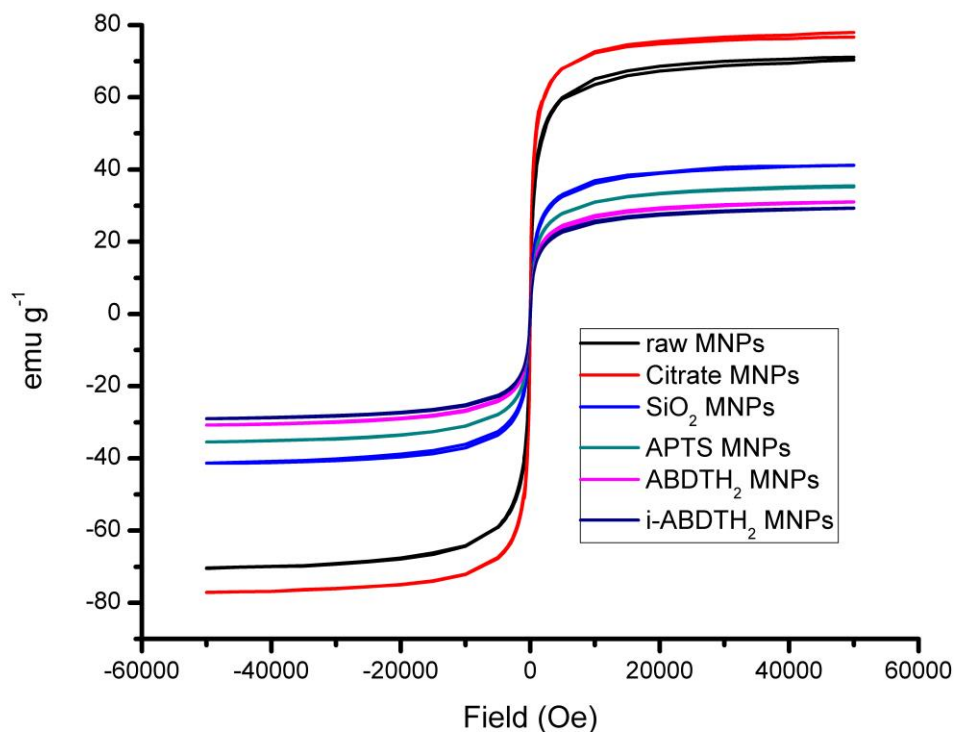


Graph 6.13 TGA for raw MNP(black) and ABDTH₂ MNP(SAMs) (red)

4.2.3 Magnetic Properties of MNPs



Figure 4.7 Dispersed ABDTH₂ MNPs and magnetically separated ABDTH₂ MNPs using computer hard drive magnets



Graph 4.14 Magnetic saturation results for the sequential intermediates in the preparation of ABDTH₂ MNPs

Figure 4.7 demonstrates the ease in separation of ABDTH₂ MNPs with computer hard drive magnets (2 min). Graph 4.14 shows the M_s measured with SQUID for the MNPs and subsequent core-shell and functionalization reactions. There was small coercivity and remanence for each sequential product as expected for particles < 50 nm with superparamagnetism and single domain character.¹¹⁵ Citrate MNPs had a slightly higher M_s , 76.7 emu g^{-1} , compared to the raw MNPs, 71.1 emu g^{-1} . Dramatic reductions in M_s , >10 emu g^{-1} , are not typical with surface stabilizing strategies that employ electrostatic repulsion such as the carboxylates of citric acid at the particle surface.¹⁵⁸ The

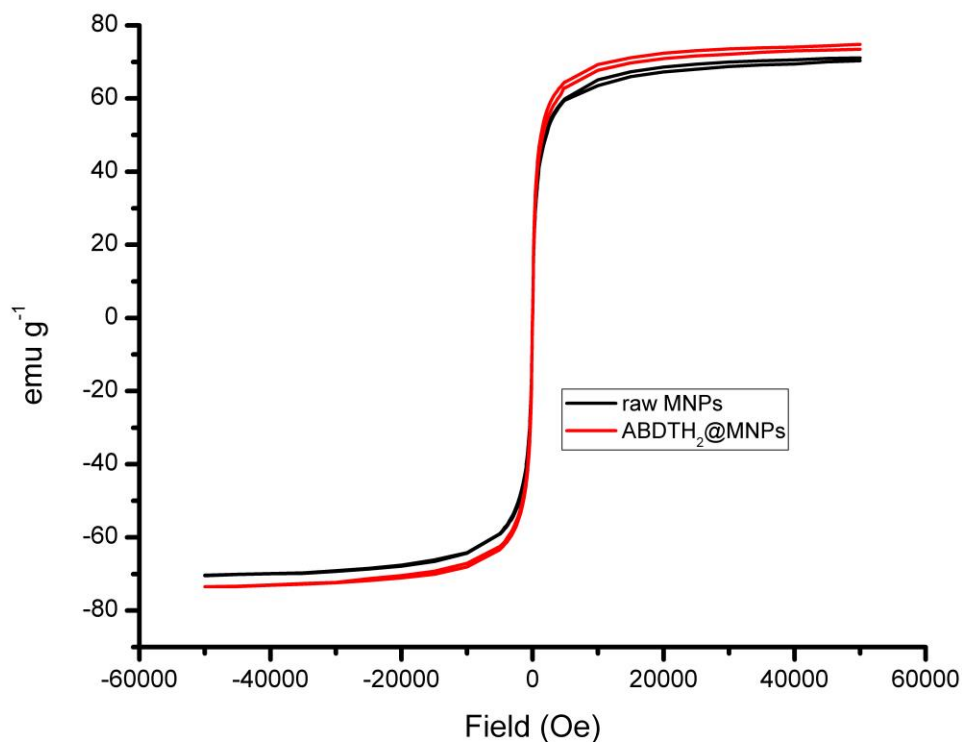
M_S of these MNPs with a particle size 11 ± 3 nm compare similarly to those listed in Table 4.2.

The silica coating is the major limiting step for M_S . The silica surface coating, with $M_S = 41.2$ emu g^{-1} , decreased saturation 42% compared to the high saturation observed for both citrate and raw MNPs.¹⁵⁹ The M_S of further surface modifications with APTS, ABDTH₂, and i-ABDTH₂ was 35.5, 31.1, and 29.3 emu g^{-1} , respectively. Table 4.2 shows size differences in shell thickness have little effect on the reduced M_S . Silica core-shell MNPs often result in >40% loss of M_S even for silica shells only several nm thick.¹⁶⁰ The largest contributions to reduced M_S following silica coverage result from decreased surface anisotropy and increased surface disorder.¹⁶⁰ The network of amorphous silica at the particle surface reduces the magnetic spin moment per unit mass.¹⁶¹ This has dramatic effects on M_S due to the increasing percentage of surface moments compared to inner core as the size of the particle decreases. Also, coordination of oxygen in the silica network to ferrous ions at the particle surface results in reduced crystallinity at the surface.¹⁶¹ The ferrous ions are responsible for the magnetic properties as the ferric ions oppose each other in the T_h and O_h sites. Oxidation of Fe(II) ions during the silica core-shell formation may also result in M_S reduction.

Table 4.2 A comparison of core-shell thickness and M_S

| Magnetic Sample | SiO₂ thickness (nm) | M_S bare (emu/g) | M_S coated (emu/g) | Ref. |
|---------------------------------------|---------------------------------------|-----------------------------------|-------------------------------------|-------------|
| Fe ₃ O ₄ oleic | 9 | 52 | 22 | 162 |
| Fe ₃ O ₄ | 70 | 81 | 53 | 152 |
| Fe ₃ O ₄ | >20 | 72 | 37 | 160 |
| Fe ₃ O ₄ citric | 24.5 | 61 | 15 | 128 |
| Fe ₃ O ₄ citric | 55 | 77 | 41 | This work |

Graph 4.15 shows the M_S of ABDTH₂@MNPs and raw MNPs. These results were omitted from Graph 4.12 for clarity. The M_S of ABDTH₂@MNPs was 74.82 emu g⁻¹ which was slightly higher compared to the bare MNPs, 71.81 emu g⁻¹. Importantly, there was not a dramatic loss of M_S with surface passivation typically seen with other core-shell techniques such as SiO₂ due to the gain and loss of surface defects and anisotropy, respectively.¹⁵⁹ This is a major difference compared to the silica core-shell strategies. ABDTH₂@MNPs should be easier to isolate in an actual use scenario compared to ABDTH MNPs.



Graph 4.15 M_s of surface stabilized ABDTH₂@MNPs (red) and raw MNPs (black)

4.3 Experimental

4.3.1 Reagents

The following reagents and solvents were obtained commercially and used as received: ferrous chloride tetrahydrate ($\text{FeCl}_2 \cdot 4\text{H}_2\text{O}$, 99+%), sodium citrate tribasic dihydrate (> 99%), tetraethyl orthosilicate (TEOS, 98%), (Na_2 N-(3-Dimethylaminopropyl)-N'-ethylcarbodiimide hydrochloride (EDC) (98%), (3-Aminopropyl)triethoxysilane (APTS, >99%), dithiothreitol (> 99%), and 4-(dimethylamino)pyridine (>99%) from Sigma-Aldrich; ferric chloride hexahydrate ($\text{FeCl}_3 \cdot 6\text{H}_2\text{O}$, 97-102%) from Fisher Scientific; Omnitrace hydrochloric acid (HCl), nitric acid (HNO_3), and ammonium hydroxide

(NH₄OH) from EMD; solvents from PHARMCO-AAPER; water was distilled and deionized (18 MΩ cm).

4.3.2 Analytical Techniques

Infrared spectra (IR) were obtained on a Nicolet Avatar 370 DTGS IR spectrophotometer manufactured by Thermo Electron Corporation. Thermogravimetric analysis (TGA) was obtained on a TA instrument Q5000 from 30 to 1000 °C under nitrogen. A custom method was developed with a ramp of 5 °C per minute until 100 °C, isothermal for 30 minutes, then an additional ramp of 5 °C per minute until 1000 °C. Zeta Potential and dynamic light scattering were measured with a Brookhaven ZetaPals Zeta Potential Analyzer. Zeta Potential measurements were recorded in triplicate with 30 read cycles for each measurement. Dynamic light scattering was performed at an angle of 90 ° for 2 minute run times and repeated in triplicate. Stock solutions were made with 3 mg of MNP with 20 mL of the pH solutions and sonicated for 5 min. prior to analysis. Magnetic saturation was measured using a SQUID with a scanning field of 50000 Oe at 310K. Transmission electron microscope images were obtained using a JEOL 2010F at 200KeV. Magnetic separation was achieved using computer hard drive magnets. Nitrogen isotherm analysis, performed using a Micrometrics Tri-Star instrument, and elemental analysis CHNO was obtained at the Center for Applied Energy Research Facility at the University of Kentucky. X-ray powder diffraction (XRD) was obtained using a Bruker-AXS D8 Discover Diffractometer from 10° to 80° (2θ) with step increments of 0.100° in 6 s at 25 °C.

4.4 Synthesis

4.4.1 Magnetite Nanoparticles

Magnetite (Fe_3O_4) nanoparticles were prepared by chemical co-precipitation of Fe(II) and Fe(III) in an alkaline medium. A fresh mixture of $\text{FeCl}_2 \cdot 4\text{H}_2\text{O}$ (0.994 g, 5.00 mmol) and $\text{FeCl}_3 \cdot 6\text{H}_2\text{O}$ (2.70 g, 10.0 mmol) was dissolved in 120 mL of deoxygenated water. After complete dissolution 20 mL of ammonium hydroxide was added rapidly, causing precipitation of a black solid, and stirred for an additional 30 minutes. The magnetite nanoparticles were washed with deoxygenated water five times and anhydrous methanol five times. The suspension was separated magnetically then dried under vacuum at room temperature.

4.4.1.1 Characterization

IR: 3500-3000 cm^{-1} (broad, $-\text{H}_2\text{O}$), 570 cm^{-1} (s, Fe-O); XRD: all Bragg planes indexed to cubic inverse spinel Fe_3O_4 ($2^\theta = 30, 36, 43, 53, 57, 63$); TGA: 1.851 % 30-100 °C (H_2O), 2.040% 100-315, 0.6610% 330-420°C, 1.189% 420-600°C ; TEM: 11 ± 3 nm; Zeta Potential (mV) pH 2: 23.54, 4: 30.38, 6: 15.4, 8:-13.38, 10:25.27; DLS (nm) pH 2: 213.5, 4: 253.6, 8: 808.2, 10: 585.1; SA 1st Batch: BET : 73.48 $\text{m}^2 \text{g}^{-1}$, Single Point Pore Volume: 0.2227 $\text{cm}^3 \text{g}^{-1}$, BJH Adsorption Pore Volume: 0.2422 $\text{cm}^3 \text{g}^{-1}$, BJH Desorption Pore Volume: 0.2414 $\text{cm}^3 \text{g}^{-1}$, Single Point Pore Radius: 6.06 nm, BJH Adsorption Pore Radius: 6.73 nm, BJH Desorption Pore Radius: 6.11 nm; 2nd Batch : BET SA: 96.8 $\text{m}^2 \text{g}^{-1}$, Single Point Pore Volume: 0.117 $\text{cm}^3 \text{g}^{-1}$, Single Point Pore Diameter: 4.9 nm.

4.4.2 Citrate Magnetic Nanoparticles

Magnetite (Fe_3O_4) nanoparticles were prepared by chemical co-precipitation of Fe(II) and Fe(III) in an alkaline medium. A fresh mixture of $\text{FeCl}_2 \cdot 4\text{H}_2\text{O}$ (0.994 g, 5.00 mmol) and $\text{FeCl}_3 \cdot 6\text{H}_2\text{O}$ (2.70 g, 10.0 mmol) was dissolved in 120 mL of deoxygenated water. After complete dissolution 20 mL of ammonium hydroxide was added rapidly, precipitating a black solid, and stirred for an additional 30 minutes. After decanting the initial volume 60 mL of 0.10 mM trisodium citrate dihydrate (17.6 mg, 60.0 μmol) was added to the magnetite precipitate and stirred at 50 °C for one hour. The citrate coated magnetite nanoparticles were washed with deoxygenated water five times and anhydrous methanol five times. The suspension was separated magnetically and dried under vacuum at room temperature for 12 h.

4.4.2.1 Characterization

IR: 3441cm^{-1} and 3258cm^{-1} (broad, $-\text{H}_2\text{O}$), 1576cm^{-1} and 1384cm^{-1} (s, CO_2^{-1}); TGA: 30-100 °C (H_2O), 100-260 °C (H_2O), 260-410 °C (CO , CO_2), 410-800 °C (CO , CO_2); Zeta Potential (mV) pH 2: 12.64, 4: -12.79, 6: -30.31, 8: -40.47, 10: -42.11; DLS (nm) pH 2: 41.2, 4: 56.3, 6: 53.6, 8: 36.1, 10: 21.6.

4.4.3 Silica Core-Shell Nanoparticles

Silica core-shell Fe_3O_4 nanoparticles were obtained by hydrolysis of TEOS on the surfaces of the Fe_3O_4 nanoparticles. Citrate coated magnetite (0.50 g) was ultrasonically dispersed in a solution containing 240 mL ethanol, 60. mL water, and 5 mL ammonium hydroxide. Tetraethylorthosilicate (0.90 mL, 0.80 g, 7.4 mmol) was added dropwise to the suspension over six hours followed by stirring for 12 h. The coated magnetite

nanoparticles were washed successively with deoxygenated water and anhydrous methanol and filtered by magnetic separation, and then vacuum dried at 80 °C for 12h. The 2nd batch increased the drying temperature to 160°C.

4.4.3.1 Characterization

IR: 3600-2700 cm⁻¹(broad, H₂O); 1160 cm⁻¹ (s, Si-O), 942 cm⁻¹ (w, Si-OH), 800 cm⁻¹ (w, Si-OH); XRD: broad Bragg peaks for amorphous silica phase occur at 18-20 2^θ and 2^θ = 30, 36, 43, 53, 57, 63 indexed to cubic inverse spinel Fe₃O₄; TEM: 55 ± 10 nm; TGA 1st Batch: 2.362 % 30-100 °C (H₂O), 2.31% 100-200 °C (H₂O), 3.354% 200-380 °C (H₂O), 1.210% 380-1000 °C (OH); 2nd Batch: 2.38 % 30-100 °C (H₂O), 2.40% 100-200 °C (H₂O), 3.28% 200-380 °C (H₂O), 0.90% 380-1000 °C (OH); BET SA 1st Batch: 125.49 m²/g, Single Point Pore Volume: 0.2692 cm³ g⁻¹, BJH Adsorption Pore Volume: 0.2817 cm³ g⁻¹, BJH Desorption Pore Volume: 0.2805 cm³ g⁻¹, Single Point Pore Radius: 4.29 nm, BJH Adsorption Pore Radius: 4.08 nm, BJH Desorption Pore Radius: 3.73 nm; 2nd Batch: 71.1 m² g⁻¹, Single Point Pore Volume: 0.09439 cm³ g⁻¹, Single Point Pore Radius: 2.66 nm. Zeta Potential (mV): pH 2: 3.71, 4: -12.79, 6: -36.36, 8: -48.45, 10: -25.27; DLS (nm): pH 2: 329.3, 4: 208.3, 6: 202.9, 8: 217.7, 10: 179.8.

4.4.4 APTS-SiO₂ Magnetic Nanoparticles

Amine-functionalized silica coated magnetite nanoparticles were prepared by condensation of 3-(aminopropyl)triethoxysilane on the silica surface. The silica-coated magnetite nanoparticles (0.500 g) were dispersed into 300 mL of dry toluene under nitrogen protection. 3-(Aminopropyl)triethoxysilane (APTS) (1.1 mL, 1.0 g, 4.5 mmol) was added drop wise to the mixture and refluxed for 12 h. The free amine terminated

composite was isolated by magnetic filtration, successively washed with toluene followed by anhydrous methanol and vacuum dried at 80 °C for 12 h.

4.4.4.1 Characterization

IR: 3600-2700 cm^{-1} (broad, H_2O); 2981 cm^{-1} (m, sp^3 C-H), 2,941 cm^{-1} , 1541 cm^{-1} (w, N-H scissor), 1160 cm^{-1} (s, Si-O), 942 cm^{-1} (w, Si-OH), 800 cm^{-1} (w, Si-OH); XRD: broad Bragg peaks for amorphous silica phase occur at 18-20 2^θ and $2^\theta = 30, 36, 43, 53, 57,$ and 63 indexed to cubic inverse spinel Fe_3O_4 ; TGA 1st Batch: 1.434 % 30-100 °C (H_2O), 19.182% 200-1000 (decomposition: H_2O , NH_3 , ethane, CO_2 , acetaldehyde, aziridine, cyclobutanone); 2nd Batch: 3.87 % 30-100 °C (H_2O), 6.67 % 100-420 °C (Decomposition), 11.45 % 420-620 °C (Decomposition: H_2O , NH_3 , ethane, CO_2 , acetaldehyde, aziridine, cyclobutanone); EA 1st Batch: %C: 9.94, %H: 2.26, %N, 1.62; 2nd Batch: %C: 9.06, %H: 2.09, %N, 1.48; Zeta Potential (mV): pH 2: 28.75, 4: 11.65, 6: -10.33, 8: -20.66, 10: -25.75; DLS (nm): pH 2: 316.5, 4: 461.1, 6: 438.2, 8: 248.4, 10: 195.3.

4.4.5 $\text{Si}(\text{CH}_3)_3\text{-APTS-SiO}_2$ Magnetite Nanoparticles

APTS-functionalized silica core-shell magnetite (0.500 g) was treated with 100 mL of 0.1 mM HCl and stirred for 1 hour. The suspension was separated magnetically then dried under vacuum at room temperature. The material was left open to air for one week before use. The APTS silica-coated magnetite nanoparticles (0.500 g) were dispersed into 300 mL of dry toluene under nitrogen protection. Chlorotrimethylsilane (0.090 mL, 0.077 g, 0.71 mmol) was added slowly by syringe and the slurry stirred at room temperature for 6 h. The solid was isolated by magnetic filtration and vacuum dried at room temperature for 12 h.

4.4.5.1 Characterization

IR: 3600-2700 cm^{-1} (broad, H_2O); 2981 cm^{-1} (m, sp^3 C-H), 2941 cm^{-1} (sp^3 C-H), 1,541 cm^{-1} (w, N-H scissor), 1160 cm^{-1} (s, Si-O), 942 cm^{-1} (w, Si-OH), 800 cm^{-1} (w, Si-OH); XRD: broad Bragg peaks for amorphous silica phase occur at 18-20 2^θ plus $2^\theta = 30, 36, 43, 53, 57,$ and 63 indexed to cubic inverse spinel Fe_3O_4 ; TGA: 2.972 % 30-100 $^\circ\text{C}$ (H_2O), 10.45% 100-510 $^\circ\text{C}$ (decomposition), 11.31 % 510-875 $^\circ\text{C}$ (decomposition); Zeta Potential (mV): pH 2: 52.81, 4: 44.21, 6: 41.75, 8: 40.36, 10: 36.28; DLS (nm): pH 2: 392.8, 4: 400.5, 6: 370.5, 8: 310.4, 10: 271.3.

4.4.6 Covalent attachment of ABDTH₂

APTS MNPs (0.500 g, 0.579 mmol APTS) were combined with 3 equivalents of triethylamine (175 mg, 0.242 mL, 1.74 mmol) in THF (30mL) and stirred for 1 h. The material was isolated magnetically followed by vacuum drying at room temperature for 6 h. APTS MNPs, ABDTH₂ (225 mg, 0.601 mmol), and 4-(dimethylamino)pyridine (73.3 mg, 0.601 mmol) were combined in DMF (100 mL) at 0 $^\circ\text{C}$ under nitrogen. 1-ethyl-3-(3-dimethylaminopropyl)carbodiimide hydrochloride (57.7 mg, 0.301 mmol) was slowly added to the mixture and stirred for 6 hours. The material was isolated by magnetic filtration and stirred in neutral water with dithiothreitol (10 mM) for 1 hour. The isolated material was washed with 200 mL water and 200 mL ethanol then dried under vacuum at 50 $^\circ\text{C}$ for 12 h.

4.4.6.1 Characterization

IR: 3600-2700 cm^{-1} (broad, H_2O); 2981 cm^{-1} (w, sp^3 C-H), 2941 cm^{-1} (sp^3 C-H), 2893 cm^{-1} , 2542 cm^{-1} (w, S-H), 1733 cm^{-1} (w, acid, (C=O)), 1639 cm^{-1} (m, amide (C=O)) 1541 cm^{-1}

¹ (w, N-H scissor), 1160 cm⁻¹ (s, Si-O), 942 cm⁻¹ (w, Si-OH), 800 cm⁻¹ (w, Si-OH); XRD: broad Bragg peaks for amorphous silica phase occur at 18-20 2^θ and 2^θ = 30, 36, 43, 53, 57, 63 indexed to cubic inverse spinel Fe₃O₄; TGA: 1.845 % 30-100 °C (H₂O), 14.60% 100-550 (decomposition), 10.953% 550-1000 °C (decomposition); Zeta Potential (mV): pH 2: 4.16, 4: -3.85, 6: -8.87, 8: -12.05, 10: -20.14; DLS (nm): pH 2: 342.0, 4: 513.1, 6: 370.1, 8: 317.5, 10: 383.9; ICP: 0.283 mmol S g⁻¹, 0.142 mmol ABDTH₂ g⁻¹, % yield to N content: 25.4%.

4.4.7 Covalent attachment of ABDTH₂ (TMS)

APTS MNPs (TMS) (0.500 g, 0.579 mmol APTS) were combined with 3 equivalents of triethylamine (175 mg, 0.242 mL, 1.74 mmol) in THF (30mL) and stirred for 1 h. The material was isolated magnetically followed by vacuum drying at room temperature for 6 h. APTS MNPs, ABDTH₂ (225 mg, 0.601 mmol), and 4-(dimethylamino)pyridine (73.3 mg, 0.601 mmol) were combined in DMF (100 mL) at 0°C under nitrogen. 1-ethyl-3-(3-dimethylaminopropyl)carbodiimide hydrochloride (57.7 mg, 0.301 mmol) was slowly added to the mixture and stirred for 6 hours. The material was isolated by magnetic filtration and stirred in neutral water with dithiothreitol (10 mM) for 1 hour. The isolated material was washed with 200 mL water and 200 mL ethanol then dried under vacuum at 50 °C for 12 h.

4.4.7.1 Characterization

IR: 3600-2700 cm⁻¹ (broad, H₂O); 2981 cm⁻¹ (w, sp³ C-H), 2,941 cm⁻¹ (sp³ C-H), 2893 cm⁻¹, 2542 cm⁻¹ (w, S-H), 1733 cm⁻¹ (w, acid, (C=O)), 1639 cm⁻¹ (m, amide (C=O)) 1541 cm⁻¹ (w, N-H scissor), 1160 cm⁻¹ (s, Si-O), 942 cm⁻¹ (w, Si-OH), 800 cm⁻¹ (w, Si-

OH); XRD: broad Bragg peaks for amorphous silica phase occur at 18-20 2^θ and $2^\theta = 30, 36, 43, 53, 57,$ and 63 indexed to cubic inverse spinel Fe_3O_4 ; TGA: 1.845 % 30-100 °C (H_2O), 14.60% 100-550 (decomposition), 10.953% 550-1000 °C (decomposition); ICP: 0.232 mmol S g^{-1} , 0.116 mmol ABDTH₂ g^{-1} , % yield to N content: 21%.

4.4.8 Ionic Attachment of ABDTH₂

APTS functionalized silica core-shell magnetite (0.500 g) was combined with ABDTH₂ (350 mg, 0.941 mmol) in EtOH (250 mL) and refluxed for 6h. The material was isolated by magnetic filtration, and washed three times with water (300 mL) and ethanol (100 mL) followed by vacuum drying at 50 °C for 12 h.

4.4.8.1 Characterization

IR: 3600-2700 cm^{-1} (broad, H_2O); 2981 cm^{-1} (w, sp^3 C-H), 2941 cm^{-1} (sp^3 C-H), 2893 cm^{-1} , 2542 cm^{-1} (w, S-H), 1733 cm^{-1} (w, acid, (C=O)), 1639 cm^{-1} (m, amide (C=O)) 1541 cm^{-1} (w, N-H scissor), 1160 cm^{-1} (s, Si-O), 942 cm^{-1} (w, Si-OH), 800 cm^{-1} (w, Si-OH); XRD: broad Bragg peaks for amorphous silica phase occur at 18-20 2^θ and $2^\theta = 30, 36, 43, 53, 57, 63$ indexed to cubic inverse spinel Fe_3O_4 ; TGA: 2.57 % 30-100 °C (H_2O), 13.72 % 100-350 (decomposition), 18.64 % 350-700 °C (decomposition); Zeta Potential (mV): pH 2: -0.46, 4: -3.71, 6: -5.61, 8: -38.30, 10: -38.73; DLS (nm): pH 2: 580.0, 4: 584.4, 6: 263.8, 8: 350.8, 10: 328.8; ICP: 0.601 mmol S g^{-1} , 0.301 mmol ABDTH₂ g^{-1} , % yield to N content: 59%.

4.4.9 Surface-Stabilized ABDTH₂ Magnetite Nanoparticles

Magnetite (Fe_3O_4) nanoparticles were prepared by chemical co-precipitation of Fe(II) and Fe(III) in an alkaline medium. A fresh mixture of $\text{FeCl}_2 \cdot 4\text{H}_2\text{O}$ (0.994 g, 5.00 mmol) and

FeCl₃ · 6H₂O (2.70 g, 10.0 mmol) was dissolved in deoxygenated water (120 mL). After complete dissolution 20 mL of concentrated ammonium hydroxide was added rapidly, precipitating a black solid, and stirred for an additional 30 minutes. After repeated decanting and water washing 120 mL of 0.1 M ABDHT₂ (EtOH) was added to the magnetite precipitate at pH 5 and stirred at 50 °C for one hour. The obtained coated magnetite nanoparticles were washed with deoxygenated water five times and anhydrous methanol five times. The suspension was separated by magnet, followed by drying under vacuum at 50 °C for 12 h.

4.4.9.1 Characterization

IR: 3500 cm⁻¹ to 2900 cm⁻¹ (broad, H₂O), 3062 cm⁻¹ (m, sp² C-H), 2884 cm⁻¹ (sp³ C-H), 2539 cm⁻¹ (w, S-H), 1739 cm⁻¹ (w, acid (C=O)), 1644 cm⁻¹ (m, amide (C=O)); TGA: 1.542 % 30-100 °C (H₂O), 100-300 °C 6.8387 % (decomposition, dehydration), 5.54% 300-500 °C (decomposition), 5.753 % 600-850 °C (decomposition); ICP: 0.461 mmol S g⁻¹, 0.230 mmol ABDTH₂; Zeta Potential (mV) pH 2: -12.74, 4: -34.73, 6: -35.19, 8: -33.41, 10: -27.01; DLS (nm) pH 2: 352.7, 4: 34.5, 6: 59.5, 8: 55.7, 10: 35.6; BET SA: 78.0m² g⁻¹, Single Point Pore Volume: 0.112 cm³ g⁻¹, Single Point Pore Diameter: 6.3 nm.

4.5 Conclusions

Magnetic nanoparticles covalently attached to ABDTH₂ were synthesized and characterized. The utility of the composite materials for the removal of arsenite will be investigated over a range of different pH values. The stabilization of the magnetite nanoparticles was achieved using sodium citrate. Negatively charged sodium citrate MNPs leads to improved silica core-shell morphologies. The functionalization of the

silica surface with APTS allows attachment of ABDTH₂. The surface chemistry of the stepwise reaction pathway has been investigated via the mobility of the colloids in an applied electric field where a measure of the stability of the composite materials can be modeled.

Chapter 5 Arsenic Removal with ABDTH₂ Magnetic Nanocomposite

5.1 Introduction

ABDTH₂ forms stable covalent S-As(III) bonds when mixed with arsenous acid (Chapter 3.2). It was hypothesized that ABDTH₂ bound to a solid support would also be capable of covalent S-As bonds. Adsorption of the solid support media would be enhanced by the inclusion of non-equilibrium removal. Attachment to a solid surface should, in theory, change the bonding arrangement of the product. Elemental analysis of the ABDT-As(III) precipitates always contained S:As ratios >3 when combined in excess, 1:2, and 1:1. However, when bound to a solid support horizontal and vertical movement along the surface should be restricted compared to stirring dissolved in EtOH. Thus the 1:3 product is not predicted to be the most common binding analog. Also, the surface density of the various ABDTH₂ functionalized MNPs is quite low. For example, the ABDTH₂ MNPs had a surface density of 0.68 ABTH₂ groups nm⁻². An interparticle complex formation may result in S₃-As sequestration, but intraparticle formation with this arrangement is unlikely. Figure 5.1 shows the optimal proposed binding of As(III) with the ABDTH₂ MNPs. All three derivatives (covalent, covalent (TMS), and ionic) of the

ABDTH₂ MNPs are expected to form similar bonds with the bidentate sulfhydryl groups and As(III).

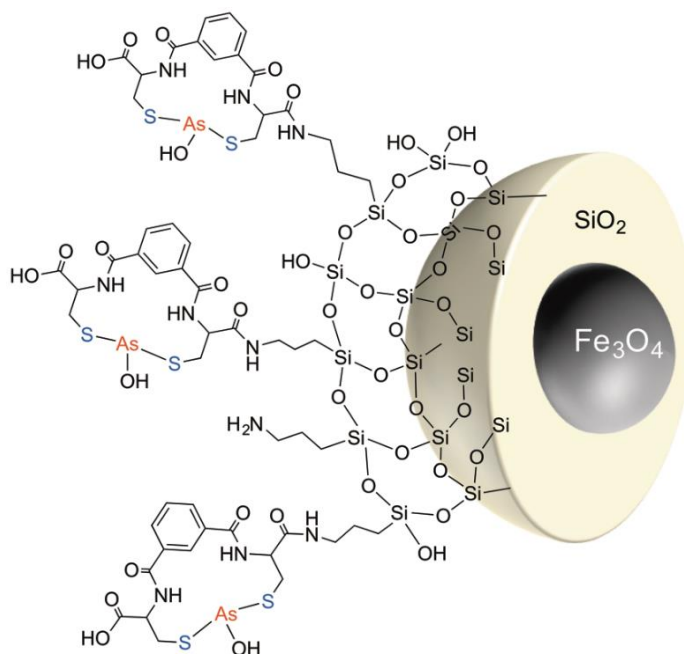


Figure 5.1 Optimal proposed split view of ABDTH₂ MNPs after As(III) removal

This chapter will explore the ability of ABDTH₂ functionalized MNPs to remove As(III) from aqueous solutions. ABDTH₂ was bound to MNPs as the following: ABDTH₂ MNPs, covalent; ABDTH MNPs (TMS), covalent; i-ABDTH₂ MNPs, ionic; and ABDTH₂@MNPs, surface stabilized ligand. The removal efficiency of these materials will be explored as a function of pH to determine the best possible conditions for capture. Also, the removal efficiency will be compared in the presence of other anions. These anions include sulfate, phosphate, carbonate, chloride, and nitrate. The surface stabilized MNPs will also be evaluated for any potential removal of As(V) and other alkyl substituted derivatives. The resulting products will be characterized and

compared to other materials with high affinities for As(III). Finally, the treated materials will be evaluated for potential leaching.

5.2 Results and Discussion

5.2.1 Aqueous As(III) Removal with ABDTH₂, ABDTH₂ (TMS), and i-ABDTH₂ MNPs as a Function of pH

The concentration of As(III), as As(OH)₃, for all batch studies was prepared to emulate typically high conditions, ~200 ppb.¹ This concentration is representative of acute risk to human life from ingestion. The performance of the materials was investigated at pH 5, 7, and 9. The limit of detection for all batch studies was the suggested safe limit, 10 ppb As, set by the World Health Organization (WHO) in 1993. Each batch was stirred unopened to air in the aqueous As(III) stock solution (50 mL) for 3h followed by magnetic separation and repeated microfiltration before elemental analysis by ICP-OES. The performance of ABDTH₂ MNPs (TMS), ABDTH₂ MNPs, i-ABDTH₂ MNPs, and ABDTH₂@MNPs for the removal of aqueous As(III) as a function of pH is shown in Tables 5.1-5.4, respectively.

Table 5.1 ICP-OES results for aqueous As(III) with ABDTH₂ MNPs (TMS)

| Sample | As (ppb) | % | As (ppb) | % | As (ppb) | % |
|-------------------------------------|----------|---------|----------|---------|----------|---------|
| | pH 5 | Removal | pH 7 | Removal | pH 9 | Removal |
| As (III) stock | 196 ± 5 | - | 203 ± 3 | - | 198 ± 4 | - |
| 0.1g ABDTH ₂ -MNPs (TMS) | 55 ± 6 | 72 | 85 ± 3 | 58 | 79 ± 2 | 60 |
| 0.2g ABDTH ₂ -MNPs (TMS) | < 10 | >95 | < 10 | >95 | <10 | >95 |

Table 5.2 ICP-OES results for aqueous As(III) with ABDTH₂ MNPs

| Sample | As (ppb) | % | As (ppb) | % | As (ppb) | % |
|------------------------------|----------|---------|----------|---------|----------|---------|
| | pH 5 | Removal | pH 7 | Removal | pH 9 | Removal |
| As (III) stock | 215 ± 3 | - | 212 ± 1 | - | 213 ± 1 | - |
| 0.1g ABDTH ₂ MNPs | 29 ± 1 | 86 | 53 ± 3 | 75 | 51 ± 8 | 76 |
| 0.2g ABDTH ₂ MNPs | < 10 | >95 | < 10 | >95 | <10 | >95 |

Table 5.3 ICP-OES results for aqueous As(III) with i-ABDTH₂ MNPs

| Sample | As (ppb) pH 5 | % Removal | As (ppb) pH 7 | % Removal | As (ppb) pH 9 | % Removal |
|--|------------------|--------------|------------------|--------------|------------------|--------------|
| As (III) stock (ppb) | 199 ± 4 | - | 195 ± 6 | - | 197 ± 2 | - |
| 0.1g i- ABDTH ₂ - MNP | 26 ± 7 | 87 | 39 ± 2 | 80 | 42 ± 4 | 79 |
| 0.2g i- ABDTH ₂ - MNP | < 10 | >95 | < 10 | >95 | <10 | >95 |

Table 5.4 ICP-OES results for aqueous As(III) with ABDTH₂@MNPs

| Sample | As (ppb) pH 5 | % Removal | As (ppb) pH 7 | % Removal | As (ppb) pH 9 | % Removal |
|-------------------------------------|------------------|--------------|------------------|--------------|------------------|--------------|
| As (III) stock | 196 ± 4 | - | 205 ± 2 | - | 206 ± 3 | - |
| 0.1g ABDTH ₂ @MNP | 31 ± 1 | 84 | 25 ± 9 | 88 | 24 ± 5 | 88 |
| 0.2 g ABDTH ₂ @MNP | < 10 | >95 | < 10 | >95 | <10 | >95 |

All ABDTH₂ functionalized materials have a high affinity for As(III) at pH 5, 7, and 9. For the 0.1g loadings, the ABDTH₂ (TMS), ABDTH₂, and i-ABDTH₂ MNPs were more similar at pH 7 and 9. At pH 5, there was a significant increase in removal percentage for each of these materials. These results compare similarly to the pH

dependency observed with As(Cys)₃, As(GS)₃, and As(DTT).^{5, 11} With increasing pH, each of these complexes had S-As bonds exchanged for competing hydroxide ions. This dependency is counter to increased reactivity of sulfhydryl groups with pH levels approaching the S-H pKa.⁹⁷ However, oxidation of As(III) to As(V) may also play a role in S-As bond displacement in alkaline solutions.

Interestingly, the ABDTH₂ MNPs (TMS) were not as effective. This suggests surface condensation reactions with As(III) were reduced and may represent the true removal capacity of the bidentate sulfhydryl groups in ABDTH₂. However, the goal of this study was to increase the removal capacity of the material, and not to increase the resource capacity of removal. The ability of ABDTH₂ to enhance the removal capacity of a material is a benefit due to the preference for “soft” ions.¹⁰⁰ Moreover, adsorption could be a pathway towards eventual covalent removal with the sulfhydryl groups. Interaction with the solid support through both inner- and outer-sphere adsorption brings the ion in closer proximity to the sulfhydryl groups. The ABDTH₂@MNPs did not show the same preference for As(III) at lower pH compared to the other materials. The removal capacity was slightly higher at pH 7 and 9, but the difference was on the margin of the standard deviations. The ability of magnetite to function as an adsorbent in alkaline conditions is an added attribute to the performance of the hybrid material. The overall loading capacities at pH 5 with 0.1g of surface passivated ABDTH₂@MNPs and silica core-shell MNPs (ABDTH₂ (TMS), ABDTH₂, and i-ABDTH₂) were 69, 55, 71, and 74 μg As g⁻¹, respectively. These results indicated that the materials were not exhausted to the theoretical limit of capture after 3h based on the total mol S g⁻¹. However, with increased 0.2g loadings all the batch results were below the 10 ppb detection limit. The IR

spectrum for all products after the As(III) batch studies confirmed removal through S-As(III) bond formation. The sulfhydryl adsorption at $\sim 2560\text{ cm}^{-1}$ was either much lower in intensity or completely missing in the various products.

These removal capabilities with As(III) all compare favorably with other filtration media presented in Table 1.2. The ability of ABTH₂@MNPs also compares to magnetite nanoparticles where a 500 ppb As(III) solution treated with 1g of magnetite removed all of the As(III).⁶⁴ Typically, the performance of magnetite to remove As(III) compared to As(V) is lower due to the neutral charge of arsenite at typical groundwater pH values.⁴⁷ However, the removal efficiency of aqueous As(III) with metal oxides suffers from several drawbacks. Some of these drawbacks include the dependency of removal on particle size, unwanted agglomeration near the PZC, oxidation of mixed metal oxides, and leaching when other anions and cations are present in a range of ionic strengths.⁶⁴ Here the limiting factor of these materials is the low concentration of ABDTH₂ on the various surfaces. Greater resource consumption may be required for a filtration scheme that only relies on this chemistry.

5.2.2 Aqueous As(III) Removal with Mixed Sodium Anions

The performance of ABDTH₂ MNPs for removal As(III) was also evaluated in the presence of different sodium anions typically found at elevated concentrations in groundwater. These sodium anions included the following: Na₂SO₄, NaHPO₄, NaNO₃, NaCl, and Na₂CO₃. The loading of ABDTH₂ MNPs and the concentration of As(III) was held constant with either 0.2g or 0.3g and 200 ppb As(III), respectively. The batch studies were done with increasing concentrations of each sodium anion collectively at

concentrations of 200, 500, and 1,000 ppb, respectively. As an example, the Stock 1000 solution contained the following: 200 ppb As(III), 1000 ppb Na₂SO₄, 1000 ppb NaHPO₄, 1000 ppb NaNO₃, 1000 ppb NaCl, and 1000 ppb Na₂CO₃. Table 5.5-5.7 lists the results of the anionic batch studies.

Table 5.5 ICP-OES results for As(III) removal with ABDTH₂ MNPs and ABDTH₂@MNPs at different anionic concentrations

| Sample ID | As (ppb) | As (ppb) | Anions * | % Removal |
|-------------------------------|----------|----------|----------|-----------|
| | Standard | Actual | (ppb) | |
| Stock 200 | 200 | 207 ± 3 | 200 | - |
| Stock 500 | 200 | 214 ± 2 | 500 | - |
| Stock 1000 | 200 | 208 ± 1 | 1000 | - |
| 0.2 g ABDTH ₂ MNPs | 200 | 76 ± 9 | 200 | 63.27 |
| 0.2 g ABDTH ₂ MNPs | 200 | 75 ± 2 | 500 | 64.92 |
| 0.2 g ABDTH ₂ MNPs | 200 | 86 ± 4 | 1000 | 58.63 |
| 0.3 g AB9@MNP | 200 | < 10 | 200 | >95 |
| 0.3g AB9@MNP | 200 | <10 | 500 | >95 |
| 0.3g AB9@MNP | 200 | < 10 | 1000 | >95 |

Table 5.6 ICP-OES results for As(III) removal with ABDTH₂ MNPs at different anionic concentrations

| Sample ID | As (ppb) | As (ppb) | % Rem. | Anion (ppb) | Cl ⁻ | NO ₃ ⁻ | PO ₄ ²⁻ | SO ₄ ²⁻ |
|-------------------------------|----------|----------|--------|-------------|-----------------|------------------------------|-------------------------------|-------------------------------|
| | Stand. | Actual | | | | | | |
| Stock 200 | 200 | 208 ± 4 | - | ~200 | 175 | 136 | 142 | 205 |
| Stock 500 | 200 | 213 ± 1 | - | ~500 | 403 | 431 | 457 | 471 |
| Stock 1000 | 200 | 220 ± 3 | - | ~1000 | 759 | 840 | 860 | 942 |
| 0.3 g ABDTH ₂ MNPs | 200 | < 10 | >95 | - | - | - | - | - |
| 0.3 g ABDTH ₂ MNPs | 200 | < 10 | >95 | - | - | - | - | - |
| 0.3 g ABDTH ₂ MNPs | 200 | < 10 | >95 | - | - | - | - | - |

The increased sodium anions at concentrations of 200, 500, and 1000 ppb for the 0.2g ABDTH₂ MNPs batch study did show some interference. These results compare to the results in Table 5.2 where complete removal was achieved with the same loading of ABDTH₂ MNPs. These results highlight the complexity of solutions outside of laboratory controls. The reduction in removal efficiency decreased 37, 35, and 41% for the 0.2 g loadings of ABDTH₂ at combined individual anionic concentrations of 200, 500, and 1000 ppb, respectively. The 0.2g loading with i-ABDTH₂ MNPs performed better, but there was still some interference from the anions. The removal efficiency decreased 18,

23, and 21%, respectively. Increased interference with ABDTH₂ MNPs compared to i-ABDTH₂ MNPs is likely the result of lower loadings of both APTS and ABDTH₂ and increased unreacted surface silanols. However, slightly higher 0.3g loadings for the ABDTH₂ MNPs, i-ABDTH₂ MNPs, and ABDTH₂@MNPs removed 100%.

Table 5.7 ICP-OES results for As(III) removal with i-ABDTH₂ MNPs at different anionic concentrations

| Sample ID | As (ppb) Standard | As (ppb) Actual | % Rem. | Anions (ppb) | Cl ⁻ | NO ₃ ⁻ | PO ₄ ²⁻ | SO ₄ ²⁻ |
|---------------------------------|-------------------|-----------------|--------|--------------|-----------------|------------------------------|-------------------------------|-------------------------------|
| Stock 200 | 200 | 208 ± 4 | - | ~200 | 216 | 227 | 264 | 250 |
| Stock 500 | 200 | 213 ± 1 | - | ~500 | 491 | 520 | 640 | 593 |
| Stock 1000 | 200 | 220 ± 3 | - | ~1000 | 961 | 1227 | 1280 | 1190 |
| 0.2 g i-ABDTH ₂ MNPs | 200 | 34 ± 3 | 82 | 200 | - | - | - | - |
| 0.2 g i-ABDTH ₂ MNPs | 200 | 44 ± 1 | 77 | 500 | - | - | - | - |
| 0.2 g i-ABDTH ₂ MNPs | 200 | 42 ± 1 | 79 | 1000 | - | - | - | - |
| 0.3 g i-ABDTH ₂ MNPs | 200 | < 10 | > 95 | 200 | - | - | - | - |

| | | | | | | | | |
|--|-----|------|------|------|---|---|---|---|
| 0.3 g i- ABDTH ₂ MNPs | 200 | < 10 | > 95 | 500 | - | - | - | - |
| 0.3 g i- ABDTH ₂ MNPs | 200 | < 10 | > 95 | 1000 | - | - | - | - |

These results show the selective affinity for As(III) even in the presence of anions much higher in concentration. Interactions with the “soft” sulfhydryl groups of ABDTH₂ and the “hard” anions is unfavorable with hard-soft-acid-base (HSAB) theory. Unreacted silica sols are relatively inert with aqueous As(III) at pH 7 compared to As(V) due to the former’s high 1st pK_A at 9.11.^{44,163} High uptake with similar silica gels requires adsorption with metal cations that function as the removal source with aqueous As(III).⁴² In comparison, a blank run with the APTS MNPs with only As(III) removed 15% of 202 ppb As solution. Thus, adsorption does indeed occur without ABDTH₂ on the solid albeit with low removal. The ABDTH₂@MNPs were not evaluated at the 200 mg loading, but did completely lower the As(III) solution to below the detection limit at higher 300 mg loadings. Phosphate, silicate, and bicarbonate reduce the removal of As(III) at low concentrations with iron hydroxides.⁵⁰ Phosphate increases the mobility of As(V) due to the similarity of charge and acidity.⁵⁰ Here, equilibrium adsorption through competitive surface complexation and covalent S-As(III) bond formation operate simultaneously for total removal. However, the former is much greater with the ABDTH₂@MNPs due to the non-covalent surface coverage and increased affinity of magnetite for As(III) compared to silica.

5.2.3 Removal of Other Forms of Arsenic with ABDTH₂@MNPs

A batch study with a 50:50 mixture of As(III) and As(V) at ~200 ppb was evaluated with 0.3g of ABDTH₂@MNPs. Also, a batch study was accessed with dimethylarsinic acid or cacodylic acid (DMA) at ~500 ppb with slightly higher 0.5 g of ABDTH₂@MNPs. Table 5.8 lists the ICP-OES results for the removal of mixed As(III/V) and DMA with ABDTH₂@MNPs.

Table 5.8 ICP-OES results for the removal of DMA and mixed As(III/V) with ABDTH₂@MNPs

| Sample ID | As(DMA) (ppb) | % Removal | As(III/V) (ppb) | % removal |
|-----------------|---------------|-----------|-----------------|-----------|
| As(DMA) stock | 507.7 | - | - | - |
| 0.15g AB9@MNPs | 197.7 | 61 | - | - |
| 0.30g AB9@MNPs | 135.3 | 73 | - | - |
| As(III&V) stock | - | - | 219.5± 1.1 | - |
| 0.3g AB9@MNPs | - | - | < 10 | 100 |

The removal of DMA results from surface complexes that form at the magnetite surface with As-O-Fe type bonds.^{164,49} ABDTH₂ was very ineffective for removing As(V). Also, the reduction of As(V) was very low with ABDTH₂ where binding through S-As(III) bonds could concomitantly occur.³³ The IR spectrum for the DMA batch study showed the sulfhydryl absorption at 2558 cm⁻¹ was still present in the ABDTH₂@MNPs. Interestingly the mixed As(III/V) batch study showed complete removal below the

detection limit (10 ppb). Here both thiolate bonds to As(III) and surface complex formation with As-O-Fe type bonds are possible. The IR spectrum for the mixed As(III/V) batch study did not contain the SH absorption at 2558 cm^{-1} after the reaction. There are numerous pathways for both As(III) and As(V) to interact with ABDTH₂@MNPs. In anaerobic conditions both As(III) and As(V) can form inner-sphere complexes with As-O-Fe bonds.¹⁶⁵ Also, the sulfhydryl groups from ABDTH₂ form covalent S-As(III) bonds. However, when both forms are present in oxidizing conditions several other reactions may occur. Figure 5.2 displays the different interactions of As(III) and As(V) with ABDTH₂@MNPs in anaerobic and aerobic conditions. In aerobic conditions both the surface of magnetite ($\text{Fe}^{2+}_{\text{Oh}}$) and As(III) are partially oxidized to maghemite and As(V), respectively.¹⁶⁵ Conversely, As(V) is partially reduced to As(III) by electron migration from internal bulk magnetite to the oxidized surface. Also, non-oxidized As(III) forms stable S-As(III) bonds from the sulfhydryl groups of ABDTH₂.

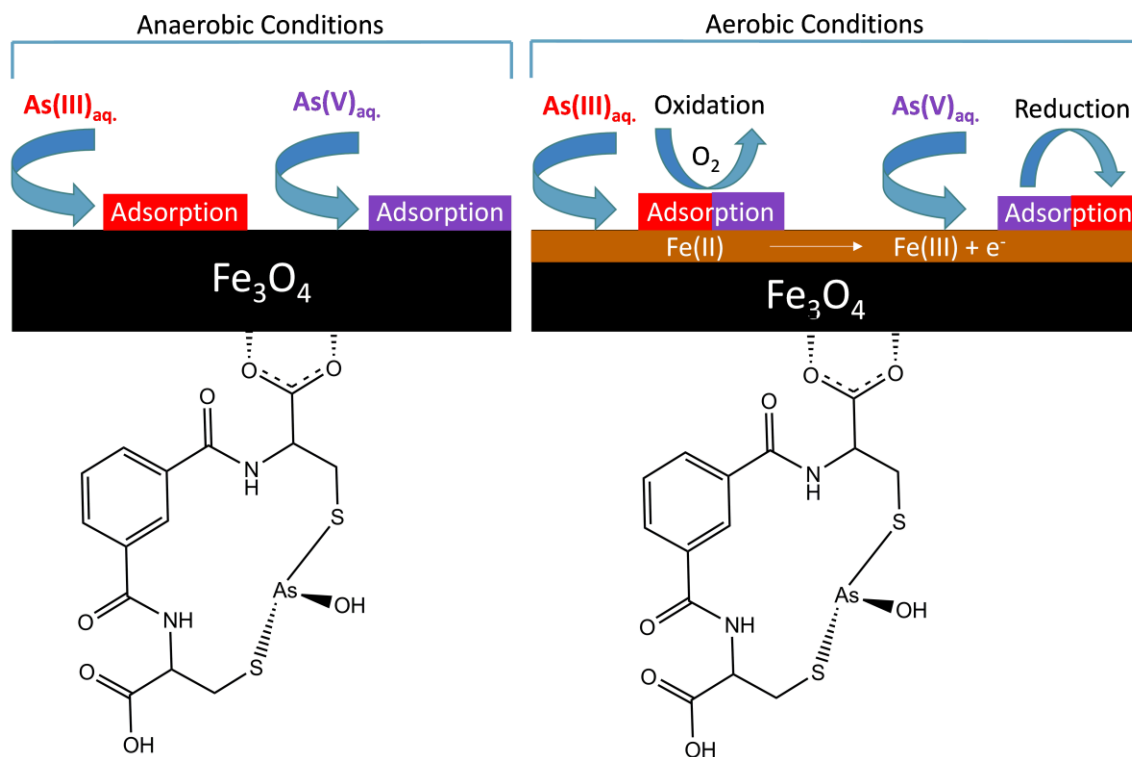


Figure 5.2 Possible interactions of As(III) and As(V) with ABDTH₂@MNPs¹⁶⁵

5.2.4 Arsenic Leaching from As-ABDT MNPs

The stability of As(III) bound to ABDTH₂ MNPs, i-ABDTH₂ MNPs, and ABDTH₂@MNPs is a requirement for an efficient removal strategy. Importantly, the covalent S-As(III) bonds that operate as the utility are less prone to oxidation and exchange outside of other variables.¹⁰³ ABDTH₂-As(III) demonstrated “soft” metal preferences for other “soft” metals when leached. Similar trends with other sulfhydryl groups support the preferences of S-Metal binding per HSAB theory. Here the leaching experiments were evaluated with the focus on stability as a function of time in the absence of other variables. The products from various batch experiments with As(III), at ~200 ppb, with 100% removal were leached. The concentrations of As were determined

at time intervals of 12, 24, and 48 h. Table 5.9 lists the leaching results as a function of time with As(III) bound to ABDTH₂ MNPs, i-ABDTH₂ MNPs, and ABDTH₂@MNPs.

Table 5.9 ICP-OES results for As leaching with ABDTH₂ MNPs, i-ABDTH₂ MNPs, and ABDTH₂@MNPs

| Sample | C ₀ As (nmol) | 12 h (nmol) | % Leach | 24 h (nmol) | % Leach | 48 h (nmol) | % Leach |
|---------------------------------|--------------------------|-------------|---------|-------------|---------|-------------|---------|
| 0.1 g ABDTH ₂ MNPs | 66.54 | 3.97 | 6.0 | 4.82 | 7.2 | 5.37 | 8.1 |
| 0.1 g i-ABDTH ₂ MNPs | 67.10 | 4.11 | 6.1 | 4.38 | 6.5 | 4.46 | 6.6 |
| 0.1g ABDTH ₂ @MNPs | 66.26 | 3.6 | 5.5 | 3.8 | 5.8 | 4.09 | 6.2 |

The results from the batch leaching studies demonstrated the stability of the S-As(III) bond for these materials. Very low levels of arsenic leached out over the 48 h evaluation. The leaching results for the ABDTH₂ MNPs were slightly higher compared to the results with i-ABDTH₂ MNPs and ABDTH₂@MNPs. However, the difference after 48 h was minimal and not unexpected since the ABDTH₂ MNPs had the lowest surface density. The leached arsenic is not expected to consist of S-As(III) bond breakage due to hydrolysis in water at pH 7. The leached arsenic may be attributable to the adsorbed arsenic from the amorphous silica and magnetite surfaces. The TGA before and after leaching for all three samples determined almost identical mass losses from 100-1000 °C.

Also, the IR spectrum was unchanged before and after the leaching experiments. The SH absorption would have occurred due to the hydrolysis of the S-As(III) bond.

These results highlight the stability of covalent S-As(III) bonds. Removal is enhanced by the addition of ABDTH₂ to these oxide surfaces.

5.3 Experimental

5.3.1 Reagents

The following reagents were obtained commercially and used as received: sodium meta-arsenite (NaAsO₂, > 99%), sodium arsenate heptahydrate (Na₂HAsO₄ · 7H₂O, >98%), sodium chloride (NaCl, >99%), sodium nitrate (NaNO₃, >99%), sodium sulfate (Na₂SO₄, >99%), sodium phosphate dibasic (Na₂HPO₄, >99%), and sodium bicarbonate (NaHCO₃, >99.7%) from Sigma-Aldrich; Omnitrace hydrochloric acid (HCl), nitric acid (HNO₃), and ammonium hydroxide (NH₄OH) from EMD; water was distilled and deionized (18 MΩ cm).

5.3.2 Analytical Techniques

The concentrations of arsenic (188.9 nm) were obtained using a Varian Vista-Pro CCD Simultaneous ICP-OES. Yttrium internal standard was used (371.029 nm) to evaluate and/or correct for matrix effects. Laboratory control samples (LCS) were produced with diluted elemental standards in 1% HNO₃. Digestions were done with 1% HNO₃, and heated if necessary to remove organics. Before ICP-OES analysis each sample was repeatedly filtered by micro-syringe filtration (0.45 and 0.2 μm). A 5-point standard curve was constructed to determine experimental concentrations.

5.4 Synthesis

5.4.1 Aqueous As(III) Removal as a Function of pH

The removal of arsenite was investigated for the different ABDTH₂ magnetic nanocomposites at pH 5, 7, and 9. Arsenic stock solutions were prepared by diluting 1 mL of a 50 ppm solution of As(III) to 250 mL using volumetric glassware. The pH of the various solutions was adjusted using either dilute Omni trace HCl or dilute ammonium hydroxide solutions. Two different loading amounts were used for the various solids. The As(III) solutions at pH 5, 7, 9 were loaded with 100 mg for the first batch study and 200 mg for the second batch study for each sample. Solutions were stirred for 3 h followed by isolation of the arsenic-containing MNPs through magnetic filtration.

5.4.2 Aqueous As(III) Removal with Mixed Sodium Anions

The aqueous As(III) solutions with increasing amounts of different sodium anions were prepared by keeping the total concentration of As(III) at ~200 ppb for all three batches while increasing each individual anion concentration collectively from 200 ppb to 500 ppb to 1000 ppb, respectively. Batch analysis was loaded with 200 mg of ABDTH₂-MNPs and i-ABDTH₂ MNPs, and with 300 mg of ABDTH₂ MNPs, i-ABDTH₂ MNPs, and ABDTH₂@MNPs, respectively. For example, the Stock 500 solution contained the following: 200 ppb As(III), 500 ppb Na₂SO₄, 500 ppb NaHPO₄, 500 ppb NaNO₃, 500 ppb NaCl, and 500 ppb Na₂CO₃. Solutions were stirred for 3 h followed by isolation of the arsenic-containing MNPs through magnetic filtration.

5.4.3 Removal of Other Forms of Arsenic with ABDTH₂@MNPs

Mixed arsenic stock solutions were prepared by diluting 0.50 mL of a 50 ppm solution of As(III) and 0.5 mL of a 50 ppm solution of As(V) to 250 mL using volumetric glassware. ABDTH₂@MNPs (300 mg) were combined with the mixed As(III &V) solution (50mL) and stirred for 3 h followed by isolation of the arsenic-containing MNPs through magnetic filtration. The dimethylarsinic acid stock solution was prepared by diluting 2.5 mL of a 50 ppm solution of DMA using volumetric glassware. Batch analysis was loaded with 150 and 300 mg ABDTH₂@MNPs. ABDTH₂@MNPs were combined with the DMA solution (50mL) and stirred for 3 h followed by isolation of the arsenic-containing MNPs through magnetic filtration.

5.4.4 Arsenic Leaching from MNPs

The arsenic-containing ABDTH₂ MNPs, i-ABDTH₂ MNPs, and ABDTH₂@MNPs (100 mg) were stirred unopened to air for 48 h. Small aliquots (5 mL) were taken from the solutions at time intervals of 12, 24, and 48 h. Separately, the MNPs (15 mg) were digested with 1:3 HCl/HNO₃ solution at 90 C for 12 hr. The solutions were diluted to the original volume before analysis with ICP-OES.

5.5 Conclusions

The high affinity of the ABDTH₂ MNPs and derivatives for aqueous As(III), the selective nature of “soft” metals and metalloids, and ease of filtration due to the magnetic properties highlight these hybrid materials. This platform could be used with other soft toxic heavy metals and metalloids, such as Hg(II) and Pb(II), in the same selective manner. The magnetic core allows for easy filtration and separation through the

introduction of a magnetic field. These results compare to raw magnetite MNPs for the efficient removal of As(III).⁶⁴ However, the removal efficiency of aqueous As(III) with iron oxides is particle size dependent. Also, agglomeration becomes problematic at neutral pH levels.⁶⁴ Competitive adsorption with oxide based filtration media can quickly exhaust its removal efficiency.⁴² The high removal efficiency of ABDTH₂ MNPs is a testament to arsenic toxicity in humans exploiting the covalent As(III)-S binding affinity.¹¹³ ABDTH₂ functionalized solid supports such as silica and magnetite are enhanced by the addition of the bidentate sulfhydryl ligand. Bimodal removal capacities increase the usefulness of the removal technology. Ideally, these materials would be combined with other phases in a filtration scheme to covalently remove “soft” ions in areas with known contamination risks to human health. For example, adding these materials towards the final stages of a filtration scheme would lower the likelihood of the sulfhydryl groups binding to solid particulates and organic matter which could be easily separated by a high gradient magnetic separator (HGMS).

Chapter 6 Flow Cell Calorimetry of Silica Supported ABDTH₂

6.1 Introduction

The chemistry of interfaces between inorganic/organic solids and aqueous solutions plays a fundamental role in the mobility and chemistry in both natural and laboratory systems. Calorimetry provides a direct quantitative method for measuring the heat of reactions. The transformed heat is directly related to the enthalpy of the chemical process. Typically, the heat is measured in either batch or flow systems. Flow calorimetry is better suited for measuring the interaction of adsorption due to the ability to cycle

multiple adsorption/desorption studies on the same sample. The shape and slope of the recorded change in heat provide an indication for the surface interaction.¹⁶⁶⁻¹⁶⁷ The width of the heat signal is a good measure of the uniformity at the interface of the reaction.¹⁶⁶⁻¹⁶⁷ Furthermore, this technique can determine the surface charge of the interface by measuring repeated anionic and cationic exchange reactions.¹⁶⁶⁻¹⁶⁷

Flow calorimetry has been used to study the interaction of arsenites and arsenates with many naturally occurring mineral phases to model the dissolution and adsorption chemistry of arsenic. As an example, the exothermic enthalpy for the adsorption of arsenate on amorphous aluminum hydroxides was determined to range from -3.0 to -66 kJ mol⁻¹.¹⁶⁶⁻¹⁶⁷ Also, the exothermic enthalpy of adsorption on hematite nanoparticles with arsenate, monomethylarsonate (MMA), and dimethylarsinate (DMA) was determined to be -160, -85, and -102 kJ mol⁻¹, respectively.⁴⁹

ABDTH₂ covalently (c-ABDTH₂-Si60) and ionically (i-ABDTH₂-Si60) bound on a sol-gel, commercial grade Kiesegel-60, will be investigated to determine the enthalpy of the sulfhydryl bond formation with aqueous As(III). Also, anionic and cationic reversible surface exchange reactions will determine the overall surface charge of the material, ABDTH₂-Si60. This calorimetry technique should elucidate the interaction of aqueous As(III) and ABDTH₂-Si60, and determine whether the measured enthalpic energies suggest covalent As(III)-S bond formation vs. equilibrium based physisorption on the silica surface.^{167,166,49} For example, calorimetric (isothermal titration) enthalpies measured with other sulfhydryl compounds mixed with As(III) supported the exothermic formation of covalent S-As(III) bonds.¹⁶⁸

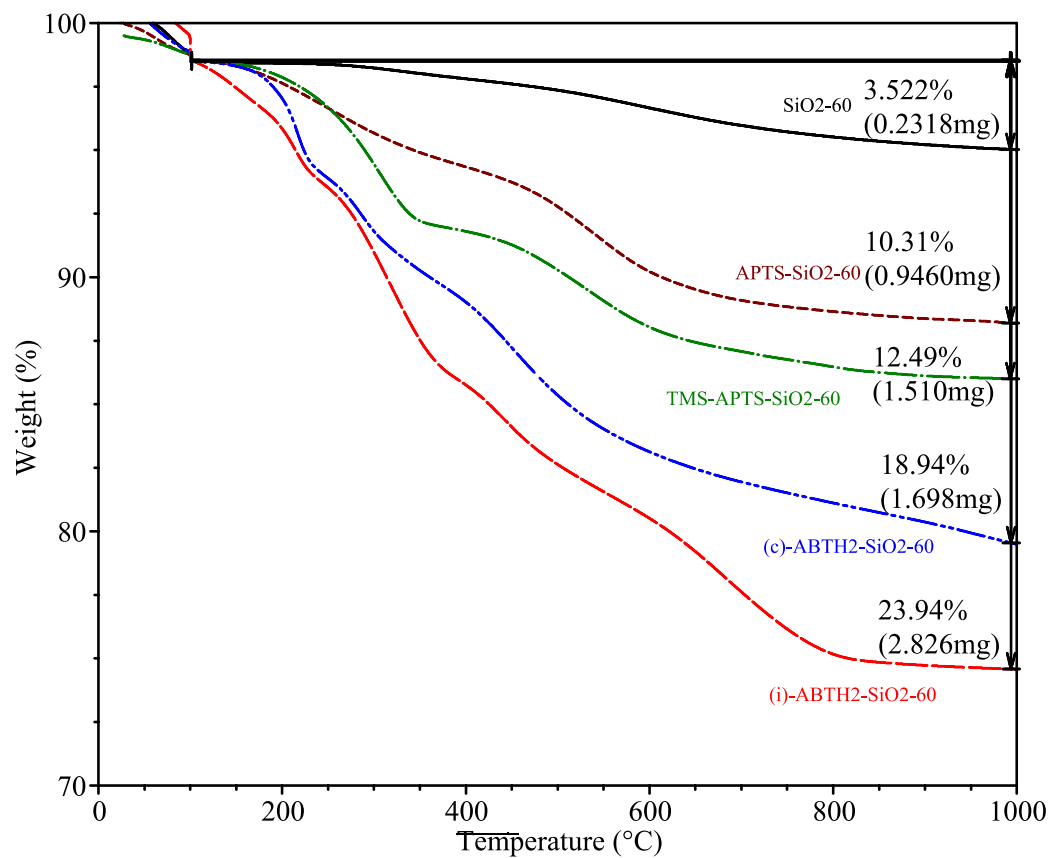
6.2 Results and Discussion

6.2.1 Synthesis and Characterization of ABDTH₂-Si60

The formation of ABDTH₂-Si60 is very similar to the synthesis previously reported for APTS functionalized silica core-shell MNPs and other silica substrates.^{135, 138, 169} A nitrogen isotherm analysis of the Kiesgel-60 showed the BET surface area was 475.1 m² g⁻¹, the single point pore volume was 0.7622 cm³g⁻¹, and the single point pore radius was 3.21 nm. This compares similarly to the BET surface area of 495 m²g⁻¹, pore diameter of 5.9 nm, and a BET pore volume of 0.9 cm³g⁻¹ for other commercial grade Kiesegel-60.¹³⁴ TGA determined the mass loss from 200-1,200 °C was 3.674% corresponding to 4.08 mmol SiOH g⁻¹ or a surface density of 5.17 SiOH nm⁻². This value fits within the accepted literature value for the surface density of silanol groups on silica, 4-7 SiOH nm².¹³¹

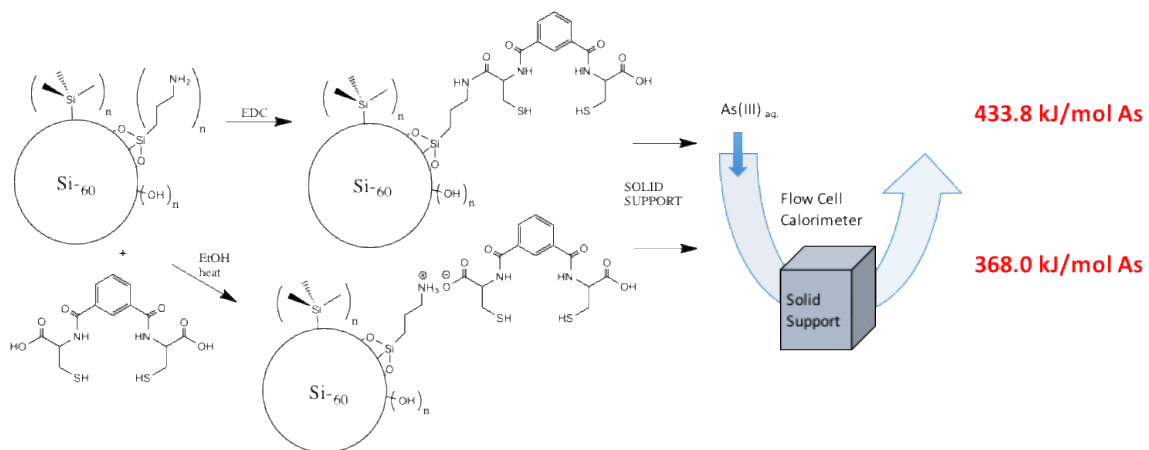
Amine functionalization with (3-aminopropyl)triethoxysilane (APTS) was formed by refluxing the suspended Si-60 beads in dry toluene.¹³⁸ Elemental analysis revealed a nitrogen concentration of 1.14% or 0.8139 mmol APTS g⁻¹ with a surface density of 1.52 APTS nm⁻². This concentration represents an overall yield of 60 % for a 3:1 silanol condensation ratio per mol APTS. The TGA shows two mass loss events from 200-600 °C with an overall increase in mass loss of 11.08% compared to raw Si-60. The surface was treated with chlorotrimethylsilane (TMS) to block any remaining surface silanol groups capable of complex formations with As(III).¹⁷⁰ The TGA of TMS-APTS-SiO₂-60 shows an additional overall mass loss of 2.1% from 100-1000 °C. This mass corresponds to 0.467 mmol TMS g⁻¹ or a yield of 29% compared to the remaining mol of SiOH.

ABDTH₂ was immobilized to the composite by two alternate routes. Both ionic (i-) and covalent (c-) bound ABDTH₂-Si-60 composites were synthesized by reflux in EtOH and EDC coupling, respectively. The BET surface area of the c-ABDTH₂-Si60 material was 322.6 m² g⁻¹ representing a net loss of 32% from the original area of the bare Si-60. The BET surface area of the i-ABDTH₂-Si60 material was 307.1 m² g⁻¹ representing a net loss of 35% from the original area of the bare Si-60. Elemental analysis by ICP-OES of the i-ABDTH₂ determined 0.625 mmol S g⁻¹ or 0.313 mmol ABDTH₂ g⁻¹. This concentration corresponds to a surface density of 1.22 ABDTH₂ groups nm⁻² with a yield of 77% for i-ABDTH₂-Si-60. Elemental analysis by ICP-OES of c-ABDTH₂ determined 0.327 mmol S g⁻¹ or 0.163 mmol ABDTH₂ g⁻¹. This concentration corresponds to a surface density of 0.304 ABDTH₂ groups nm⁻² with a coupled yield of 40% for c-ABDTH₂-Si60. TGA showed the additional mass lost compared to the previous steps were 13.63 % and 6.45 % for i- and c-ABDTH₂. These mass losses correspond to 0.366 and 0.173 mmol i- and c-ABDTH₂ g⁻¹, respectively. The TGA results compare very similarly with the concentrations determined by ICP-OES.



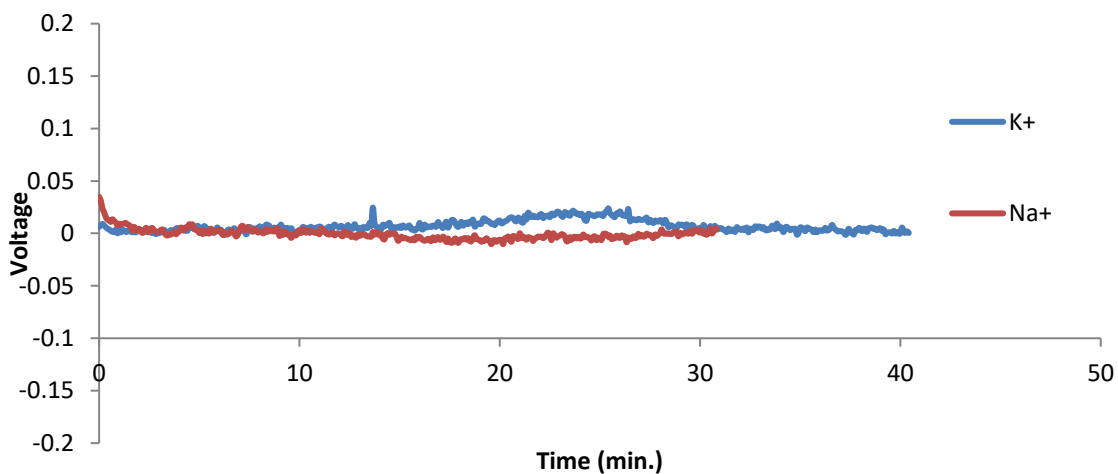
Graph 6.1 TGA results for bare Si60 (black), APTS-Si60 (brown), TMS-APTS-Si60 (green), i-ABDTH₂-SiO60 (red), and c-ABDTH₂-Si60 (blue)

6.2.2 Flow Cell Calorimetry with ABDTH₂-Si60 with Arsenite



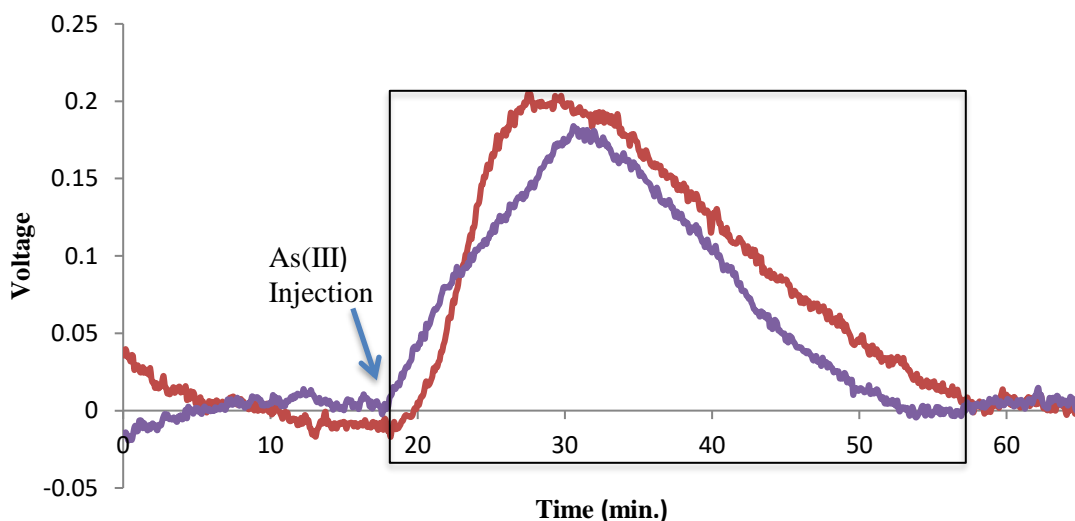
Scheme 6.1 Ideal proposed structures with ABDTH₂-Si60

The samples were both characterized with flow cell calorimetry and dosed with small arsenite injections. The ABDTH₂ functionalized samples were characterized by anionic (Cl⁻/NO₃⁻) and cationic (Na⁺/K⁺) exchange reactions at pH 5.6 to ensure that there were no changes in the recorded heat values. Importantly, Graph 6.2 shows there was only a small response, < 0.02V, from the cationic injections. The surface of silica is negatively charged at this pH with a PZC of ~2.



Graph 6.2 Cation exchange for ABDTH₂-Si60

Graph 6.3 shows the arsenite injections into the line of the flow cell calorimeter. Repeated As(III) injections were not measured with these samples. However, several cationic (Na⁺/K⁺) and anionic (Cl⁻/NO₃⁻) reversible exchange solutions were measured to ensure enthalpic energies did not change after injections. The area of the heat curves was integrated and converted to joules based on three separate prior heat pulses. The enthalpic calculations correspond to the moles of arsenic determined by ICP-OES of the digested solids. These enthalpic values are presented assuming the possibility of mixed S_x-As bonding where x= 1,2, or 3. ICP-OES determined the As content for c-ABDT-As(III) was 0.0963 μmol As and for i-ABDT-As(III) was 0.205 μmol As.



Graph 6.3 As(III) injection heat curve, cov.-ABDTH₂ (purple), ion.-ABDTH₂ (red)

The measured enthalpy of the As(III) injection for the c-ABDTH₂-Si60 sample was -434, -217, and -145 kJ mol⁻¹ based on the three possible As:S ratios of 1:1, 1:2, and 1:3, respectively. The enthalpy of the i-ABDTH₂-Si60 sample was -368, -184, and -123

kJ mol^{-1} based on the three possible A:S ratios of 1:1, 1:2, and 1:3, respectively. The literature value for the As-S bond energy is $379.5 \text{ kJ mol}^{-1}$ and compares similarly to a As:S bond ratio of 1:1 with respect to both ABDTH₂-Si60 samples where the c-ABDTH₂-Si60 sample was $54.28 \text{ kJ mol}^{-1}$ larger, and the i-ABDTH₂-Si60 was 11.5 kJ mol^{-1} smaller. However, due to the nature of bidentate proximity a ratio of As:S of 1:2 is predicted to be the predominant form with $\Delta H = -217$ and -184 kJ mol^{-1} , respectively. The large heat response for both samples is not indicative of non-covalent interactions (physisorption), and it is assumed that the measured heat resulted from the formation of As(III)-thiolate bonds. For example, enthalpic values from physisorption are generally in the range of $2.1\text{-}20.9 \text{ kJ mol}^{-1}$, and those greater are typically chemical adsorption.

These reported values compare to previous calorimetric As(III) results with similar sulfhydryl molecules. For example, GSH mixed with aqueous As(III) generated a measured $-161.92 \text{ kJ mol}^{-1}$ with a As:S ratio of 1:3.¹⁶⁸ Similarly, aqueous As(III) mixed with DMSA was -114.2 kJ/mol with a As:S of 1:2, DHLA was $-179.9 \text{ kJ mol}^{-1}$ with a As:S of 2:3, and DTT was $-57.3 \text{ kJ mol}^{-1}$ with As:S of 1:1.¹⁶⁸

6.3 Experimental

6.3.1 Reagents

The following reagents and solvents were obtained commercially and used as received: sodium meta-arsenite (>98%), N-(3-Dimethylaminopropyl)-N'-ethylcarbodiimide hydrochloride (EDC) (98%), (3-Aminopropyl)triethoxysilane (>99%), chlorotrimethylsilane (98%), and isophthaloyl chloride (> 99%) from Sigma-Aldrich; Omnitrace hydrochloric acid (HCl) and nitric acid (HNO₃) from EMD; silica gel Si₆₀ (0.5

to 1.0 mm) from Macherey Nagel; solvents from PHARMCO-AAPER; water was distilled and deionized (18 M Ω cm). ABDTH₂ was synthesized according to Chapter 2.2.

6.3.2 Analytical Techniques

Thermogravimetric analysis (TGA) was obtained on a TA instrument 2950 TGA HR V5.4A from 30°C to 1000°C under nitrogen. A custom method was developed: a ramp of 5°C per minute until 100 °C, isothermal for 30 minutes, then an additional ramp of 5 °C to 1000 °C. The arsenic concentration was determined using a Varian Vista Pro CCD Simultaneous Inductive Coupled Plasma Spectrometer (ICP-OES) at a wavelength of 188.98 nm. Laboratory control samples (LCS) were produced with diluted elemental standards in 1% HNO₃. Before ICP-OES analysis each sample was repeatedly filtered by micro-syringe filtration (0.45 and 0.2 μ m). A 5-point standard curve was constructed to determine experimental concentrations. Flow cell measurements were made on a proprietary instrument at the College of Agriculture at the University of Kentucky. Cationic and anionic exchange reactions were done with 0.1 M NaCl and 0.1M KCl. Anionic exchange reactions were done with 0.1M KCl and 0.1M KNO₃. Arsenic injections were done with 0.1 mM sodium meta arsenite. Nitrogen isotherm analysis was performed using a Micrometrics Tri-Star instrument and CHNO elemental analysis was obtained at the Center for Applied Energy Research Facility at the University of Kentucky.

6.4 Synthesis

6.4.1-Si60

6.4.1.1 Characterization

BET SA: $475 \text{ m}^2 \text{ g}^{-1}$, Single Point Pore Volume: $0.762 \text{ cm}^3 \text{ g}^{-1}$, BJH Adsorption Pore Volume: $0.798 \text{ cm}^3 \text{ g}^{-1}$, BJH Desorption Pore Volume: $0.795 \text{ cm}^3 \text{ g}^{-1}$,

Single Point Pore Radius: 3.21 nm, BJH Adsorption Pore Radius: 2.72 nm, BJH

Desorption Pore Radius: 2.46 nm; TGA; 1.71% 30-100 °C (H₂O), 3.67 % 200-1000 °C (H₂O).

6.4.2 APTS-Si60

Kiesegel-60 silica (0.500 g) was dispersed into 300 mL of dry toluene under nitrogen protection. 3-(Aminopropyl)triethoxysilane (APTS) (1.1 mL, 1.00 g, 4.52 mmol) added drop wise to the mixture and refluxed for 12h. The solid was filtered and washed with CHCl₃ (5 x 80 mL), and dried under vacuum for 12 h.

6.4.2.1 Characterization

EA: 1.14% nitrogen, 11.9% carbon, 2.16% H; TGA: 1.43 % 30-100 °C (H₂O), 11.08% 200-1000 H₂O (decomposition: H₂O, NH₃, ethane, CO₂, acetaldehyde, aziridine, cyclobutanone).

6.4.3 APTS-Si60 (TMS)

APTS functionalized Si60 (0.500g) was treated with 100 mL of 0.1 mM HCl and stirred for 1 hour. The suspension was filtered and then dried under vacuum at room temperature. The material was left open to air for one week before use. The APTS-Si60

(0.500 g) was dispersed into 300 mL of dry toluene under nitrogen protection.

Chlorotrimethylsilane (0.150 mL, 0.136 g, 1.25 mmol) was added slowly by syringe and the slurry was stirred for 6 h. The solid was isolated by filtration and vacuum dried at room temperature for 12 h.

6.4.3.1 Characterization

TGA: TGA: 1.01 % 30-100 °C, 12.5% 23.9% 200-1000°C (decomposition)

6.4.4 ABTH₂-Si ionic

APTS-Si60 (0.500 g) was refluxed in a solution of ABDTH₂ (350 mg, 0.936 mmol) in ethanol (500 mL) for 24 h. After refluxing, the solid was filtered and washed with water (12 x 50 mL) and dried under vacuum.

6.4.4.1 Characterization

ICP: 0.625 mmol S, 0.313 mmol ABDTH₂; TGA 2.97 % 30-100 °C, 23.9% 200-1000°C (decomposition).

6.4.5 ABDTH₂-Si covalent

APTS-Si60 (0.500 g) was combined with 3 mole equivalents of triethylamine and stirred for 1 h. The suspension was isolated by filtration followed by vacuum drying at room temperature for 6 h. APTS-Si60 (0.500 g), and ABDTH₂ (350 mg, 0.936 mmol) and 4-(dimethylamino)pyridine (0.114 g, 0.936 mmol) were combined in DMF (100mL). 1-ethyl-3-(3-dimethylaminopropyl)carbodiimide hydrochloride (92.5 mg, 0.480 mmol) was slowly added to the mixture and stirred for 6 h. The product was isolated by filtration and stirred in neutral water with dithiothreitol (10 mM) for 1h followed by isolation and

repeated washing with water (5 x 100 mL) and EtOH (4 x 50mL). The product was vacuum dried at room temperature for 12 h.

6.4.5.1 Characterization

ICP: 0.327 mmol S, 0.163 mmol ABDTH₂; TGA 1.80 % 30-100 °C (H₂O), 18.9% 200-1000°C (decomposition).

6.5 Conclusions

The calorimetry data demonstrates that the ABDHT₂-Si60 interactions with As(III) are not due to physisorption. These results compared very similarly to the As-S literature bond energy, 397.8 kJ/mol. Importantly, this is the first recorded measurement of the As-S bond energy using flow cell calorimetry. Previous methods used to determine the S-As bond energy with molecules such as GSH and DMSA were measured using potentiometric calorimetry. The similarities in enthalpic results suggest that flow calorimetry is well suited for modeling the interactions of adsorption or bond formation with functionalized materials.

Chapter 7 Removal of Aqueous Arsenic from Methane Gas Production

7.1 Introduction

Large deposits of methane gas are produced during the bioprocessing of organic matter present in landfills. The methane can be mined as an alternative source of energy.¹⁷¹⁻¹⁷³ Figure 7.1 shows the energy cycle of landfills. There are four stages in waste degradation in landfills. These include initial aerobic, acidogenic, initial

methanogenic, and stable methanogenic. Methane is produced in the latter two stages by methanogenic archaea.¹⁷⁴

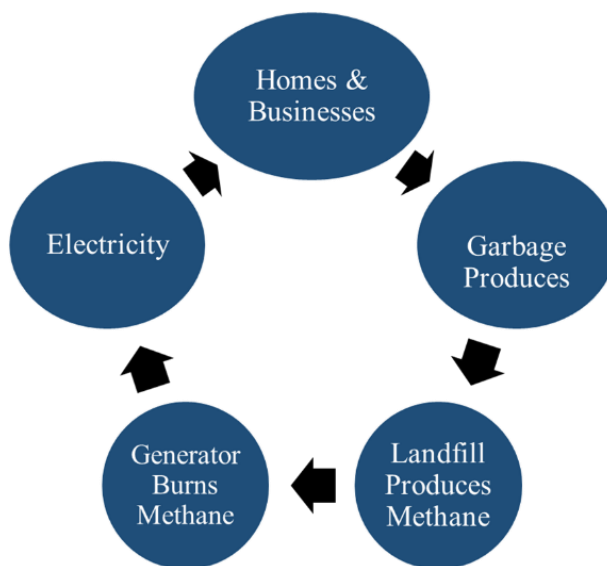
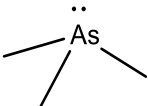
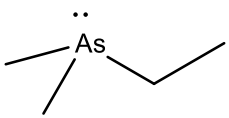
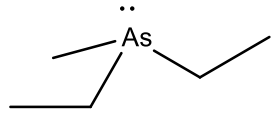
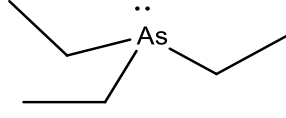


Figure 7.1 Methane generation and renewable energy cycle

Arsine, AsH_3 , is not the most common form of arsenic in typical biogas. Instead, inorganic arsenic is converted to various alkyl substituted arsine species by microbial transformations.¹⁷⁵ Both microbial oxidations of carbon sources and reduction of As(V) play important roles in this process.¹⁷⁵ The major products in this process include volatile methyl- and ethyl- derivatives of arsine.¹⁷⁴ Volatilization of arsenic has been suggested as an alternative method of arsenic remediation.¹⁷⁵ Arsenic contaminated soils and wastes could be volatilized in the atmosphere to safe levels due to dilution. However, there are safety concerns that prevent wide scale adoption. Table 7.1 lists common alkyl substituted arsines found in methane mining.

Table 7.1 Common arsenic compounds present in landfill methane gas production

| As Compound | Structure | BP (°C) | % Comp. |
|-------------------------------|---|---------|---------|
| Trimethylarsine (TMA) |  | 51 | 70 |
| Dimethylethylarsine (DMEA) |  | 36 | 20 |
| Methyldiethylarsine (MDEA) |  | 111 | 8 |
| Triethylarsine (TEA) |  | 140 | 2 |

Water is condensed from the compression and cooling of the landfill gas during methane capture at the landfill site. These solutions are labeled “condensate” at the production facility. In a separate process, water is collected from scrubber blow down during the removal of hydrogen sulfide species using a Cameron process that produces sulfur, sulfate, and thiosulphate.¹⁷⁶ Hydrogen sulfide in biogas is the result of sulfate reduction by bacteria.¹⁷⁴ The hydrogen sulfide is deprotonated in a NaOH medium producing HS⁻ which is then fed to a bioreactor. Bacteria (*Thiobacillus* spp.) convert the HS⁻ into environmentally safe elemental sulfur which is then reused as fertilizer

additives. The hydroxide produced from the bacteria transformation is then recycled back to an alkaline scrubber for further removal of hydrogen sulfide. Figure 7.2 shows the Cameron process for the removal of hydrogen sulfide.

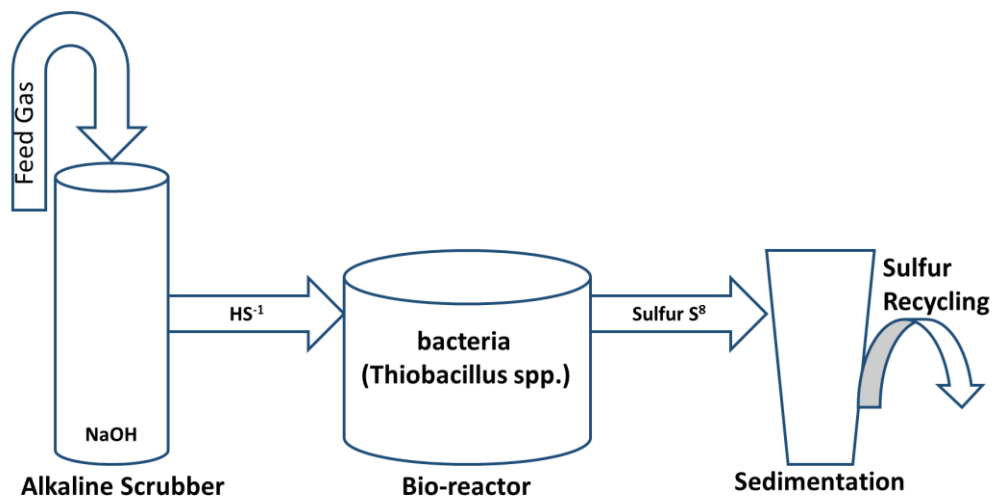


Figure 7.2 Stepwise Cameron process for treating H₂S from biogas

High levels of arsenic are often found in the condensate and blow down solutions.^{177,178} An effective arsenic removal strategy must be used to lower the concentration below regulated levels before discharge. Unfortunately, arsenic typically concentrates in the downstream condensates. For very problematic solutions, the water is stored indefinitely due to the complex chemistry involved in the removal process. There is a critical need for arsenic removal technologies capable of removing arsenic from these solutions that can withstand the harsh conditions of bioaccumulated solutions. To address these issues, this chapter will explore the ability of BDTH₂, ABDTH₂, and ABDTH₂@MNPs to remove arsenic from condensate and Cameron solutions from an active landfill site. Each component in the arsenic removal process will be analyzed to promote efficient capture. These components include an evaluation of removal as a

function of pH, oxidation, speciation of arsenic and other toxic metals, and interference from other ions in the solution matrix.

7.2. Results and Discussion

7.2.1 Arsenic Removal from Aqueous Condensate From Methane Gas Production.

Two different condensate solutions were provided from the landfill production site. The first solution, Tank 1, was used exclusively for the batch experiments with BDTH₂ and ABDTH₂ as chemical precipitation chelates. The second solution, Tank 2, was used exclusively for the batch experiments with ABDTH₂@MNPs. Both condensate solutions were dark brownish to gray colored and oily. Both solutions were extremely pungent and nauseating even inside a fume hood. There were black and white particulates floating in solution. The solutions had to be repeatedly filtered via normal filter paper until no precipitate was collected. The condensate solutions were both neutral with a pH of 7.21 and 7.46, respectively.

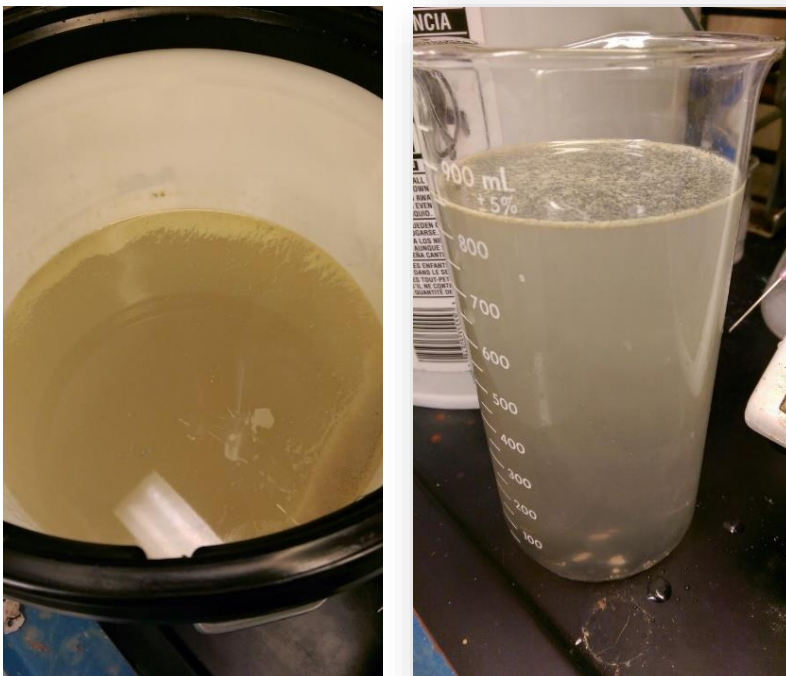


Figure 7.3 Unfiltered condensate water from the landfill methane production site

The hypothesis that most of the total arsenic was methylated was quickly rejected due to repeated attempts at extracting the condensate with organic solvents (acetonitrile and ethyl acetate) with no conclusive determinations of expected alkyl substituted arsine species with HPLC. The extracted organic phase and aqueous phase were quantified for total As (Table 7.2). This concentration of total As, 2.09 ppm, is representative of some of the worst groundwater contaminated locations.⁴⁴ Early attempts at removal with both BDTH₂ and ABDTH₂ with quantitative molar ratios resulted in low removal of total arsenic. These assumptions were based on the concentration of total As being under reported by the methane gas production facility by 1.64 ppm. However, with excess 500 mol equivalents of BDTH₂ and ABDTH₂, there was significant removal at pH 7. The extracted aqueous phase retained > 99 % of the total As present in the original condensate. The retention of total As in the aqueous phase led to the conclusion that

either there were low concentrations of alkyl substituted arsines or the As species was tightly associated with ions present in the aqueous solution. Acidification with As species present in biogas improves sequestration due to the oxidation of alkyl substituted As(III) to As(V) in nitric acid solutions. Protonation of potential species containing hydroxogroups in these solutions was unsuccessful. Acidification resulted in lower removal of total As even at increased 1000 mol equivalents of BDTH₂.

Table 7.2 ICP-OES results for the BDTH₂ batch at pH 7

| Sample | As (ppm) | % Removal |
|-------------------------------------|-------------|-----------|
| Condensate Tank 1 raw | 2.09 ± 0.02 | - |
| Condensate Tank 1 aq. ext. | 2.06 ± 0.02 | < 1 |
| BDTH ₂ 500 mol eq. | 1.34 ± 0.01 | 36 |
| ABDTH ₂ 500 mol eq. | 1.64 ± 0.06 | 22 |
| BDTH ₂ 1000 mol eq. pH 2 | 1.55 ± 0.06 | 28 |

Due to the increased difficulties encountered with the condensate solutions a batch study was conducted as a function of pH. Both pH extremes were tested for the removal efficiency with BDTH₂ and ABDTH₂ as chemical precipitation agents. Table 7.3 lists the ICP-OES results for the removal of total arsenic as a function of pH with excess BDTH₂ and ABDTH₂. The removal efficiency at pH 10 was much greater than the results at pH 2. These results highlight the pK_a of the sulfhydryl group at 9.2. Increased

reactivity is commonly observed at pH levels where S^- exist as the predominate species.⁹⁷ For comparison, i-ABDTH₂-Si₆₀ stabilized as the ammonium carboxylate salt showed very little total As removal from the condensate (Tank 1). The solid support method was used to evaluate any increase in removal resulting from adsorption to the silica surface. However, the mol equivalent of S, 46 eq., was much lower and silica is not a highly selective adsorbent for either As(III & V) species. It should be noted this removal efficiency with BDTH₂, 55%, had not been reached with the condensate even after contacting three separate unnamed commercial sources known for containment in the methane gas industry by the firm representing the landfill production site.

Table 7.3 ICP-OES results for total As removal with BDTH₂ and ABDTH₂ as a function of pH (500 mol eq.; only the batch studies at pH 10 were run in triplicate)

| Sample | Total As (ppm) | pH | % Removal |
|--------------------------------------|----------------|----|-----------|
| BDTH ₂ | 1.73 | 2 | 36 |
| BDTH ₂ | 0.942 ± 0.002 | 10 | 55 |
| ABDTH ₂ | 1.61 | 2 | 23 |
| ABDTH ₂ | 1.388 ± 0.001 | 10 | 34 |
| ABDTH ₂ -Si ₆₀ | 1.62 | 2 | 22 |
| ABDTH ₂ -Si ₆₀ | 1.78 ± 0.02 | 10 | 15 |

A different approach to removal was considered due to the very high ratios of BDTH₂ and ABDTH₂ required for the condensate solutions. Failed attempts at oxidation with acid were reevaluated with peroxide treatment open to air. Also, due to the lack of S-As(V) bonding with BDTH₂ and ABDTH₂, the MNPs were used as the main target for sequestration. Here the MNPs were stabilized in aqueous solution with ABDTH₂ as ABDTH₂@MNPs. As(III & V) can form As-O-Fe type bonds at the surface of MNPs in both monodentate and bidentate form.^{164,49} Highly efficient removal of As in both oxidation states is rare for a typical metal oxide or adsorbent materials. Typically As(V) removal greatly exceeds As(III) due to the charge of the oxyanion in aqueous solution.⁴² Also, filtration is enhanced by the magnetic properties of the MNPs. A detailed description of the ABDTH₂@MNPs is given in Chapter 4.

Table 7.4 lists the performance of ABDTH₂@MNPs for the removal of total As from the condensate solutions. Different loadings were used for the condensate batch study. Also, the solutions were diluted due to the turbidity as either 2x or 10x. Hydrogen peroxide was used in several batch studies in an attempt to oxidize any potential alkyl substituted forms to As(V) where surface complex formation at the magnetite surface would occur.¹⁷⁹

The concentration of total arsenic from the undiluted condensate solution was 1.396 ppm. This concentration was lower in comparison to the other condensate (Tank 1), 2.09 ppm As. The removal of arsenic was low for both the 0.15 and 0.3g loadings. For example, the 2X diluted solution retained 62% of total arsenic. Increased loadings of ABDTH₂@MNPs showed no significant relationship to increased removal capacity with the diluted solutions. The attempt to oxidize potential methylated species to As(V) did

not show any increase in removal efficiency. Interestingly, the 2X-diluted solutions had better removal efficiency compared to the 10X-diluted solutions. The condensate solution was analyzed for other anions that may be interfering with removal due to the low removal efficiency of ABDTH₂@MNPs. Table 7.5 lists the ion chromatography (IC) results for the condensate solution.

Table 7.4 ICP-OES results for total As removal with ABDTH₂@MNPs

| Sample ID | As (total) (ppb) | % Removal |
|---|------------------|-----------|
| 2x Dilution Stock Condensate | 698 ± 2 | - |
| 10x Dilution Stock Condensate | 322 ± 5 | - |
| 0.15g ABDTH ₂ @MNPs 2x | 430 ± 11 | 38 |
| 0.3g ABDTH ₂ @MNPs 2x | 444 ± 2 | 36 |
| 0.15g ABDTH ₂ @MNPs 10x | 283 ± 4 | 12 |
| 0.3g ABDTH ₂ @MNPs 10x | 276.3 ± 2.6 | 14 |
| 0.3g ABDTH ₂ @MNPs 2x H ₂ O ₂ | 466 ± 1 | 33 |
| 0.3g ABDTH ₂ @MNPs 10x H ₂ O ₂ | 225 ± 3 | 30 |

Table 7.5 Results for common anions in condensate tank 2

| Sample | Chloride (ppm) | Phosphate (ppm) | Sulfate (ppm) |
|-------------------|----------------|-----------------|---------------|
| Condensate Tank 2 | 0.92 ±0.02 | 2.74 ± 0.09 | 201.5 ± 0.2 |

The total carbonate concentration in the condensate solution was not determined due to the carbonate buffer used as an eluent for the column. The concentration of sulfate was very high at 201.5 ppm. For example, only 3% of drinking water in the US contains sulfate concentrations >250 ppm. In comparison, the concentrations of both phosphate and chloride were much lower and near the range evaluated with As(III) and ABDTH₂@MNPs with 100% removal (Chapter 5). The high concentration of sulphate may be a contributing factor for the low removal efficiency. For example, iron hydroxide affinities (single ion) for various anions decreased in the order arsenate > phosphate > arsenite > silicate > bicarbonate.⁵⁰ However, when anions were combined interference of both As(III) and As(V) occurred. On the other hand, ferric hydroxide binding to both As(III) and As(V) was unaffected when the sulfate concentration was increased to 300 ppm.⁴⁸ The condensate likely contains other possible interferences that were not evaluated by IC. For example, dissolved organic solids and other ions in the solution are capable of interference with adsorption.

Table 7.6 lists the concentrations of other toxic metals in the condensate solution. The condensate contained significant concentrations of Cd, Cu, and Pb. The limit of detection for all metals was 10 ppb. Competitive adsorption of Cd(II) and Pb(II) may interfere with the potential As-O-Fe bond formations at the MNP surface.¹⁸⁰ Both Cd(II)

and Pb(II) complex formation with similar bare MNPs increased in alkaline solutions.¹⁸⁰ Preference in alkaline media between the two ions was inconclusive. However, in more acidic solutions MNPs showed increased preference of Pb(II) ions. Both ions are capable of inner-sphere complex formation as Fe-O-Pb⁺ and Fe-O-Cd⁺, respectively. Sulfur was also very high in the condensate. Here, removal is complicated both by the additional “soft” metals that form covalent S-M(II) bonds and by the high sulfur concentration. Elemental analysis of the treated ABDTH₂@MNPs by ICP-OES for S is unreliable and includes error from physically bound ions containing S from the condensate. Interestingly, the concentrations of Cd, Pb, and Cu were mostly unaffected after treatment with ABDTH₂@MNPs. These results compare to the low removal efficiency for total arsenic with the same loading of ABDTH₂@MNPs (300mg).

Table 7.6 ICP-OES results for other metals in condensate (concentrations listed as ppm; 300 mg ABDTH₂@MNPs)

| ID | S | Cd | Cu | Pb |
|--------------------------|-------------|--------------|--------------|--------------|
| Raw Condensate | 62.5 ±0.2 | 0.077 ±0.001 | 0.281 ±0.003 | 0.380 ±0.008 |
| ABDTH ₂ @MNPs | 39.12 ±0.04 | 0.084 ±0.003 | 0.270 ±0.005 | 0.351 ±0.03 |
| Treated Condensate | | | | |

7.2.2 Arsenic Removal from Redissolved Aqueous Condensate

The most common alkyl substituted arsines in biogas (Table 9.1) are volatile low-boiling compounds. Due to their volatility, the condensate solution was evacuated under vacuum at >100 °C for 6 hours until no filtrate remained to determine the remaining total

As. The darkish oily residue was then redissolved using DI H₂O back to the original volume.

Table 7.7 lists the ICP-OES results for the redissolved condensate solutions. The total As removal was evaluated with an increased loading of ABDTH₂@MNPs (1g) with the original condensate. The total As concentration of the redissolved condensate solution was 982 ppb As. This concentration represents 70.34% of total As remaining after removal of the filtrate under heat and vacuum treatment compared to the stock condensate, 1,396 ppb total As. Interestingly, the 1g ABDTH₂@MNPs batch results with the stock condensate had a concentration of 584 ppb total As. This concentration represents 58% total As removal compared to the stock condensate, 1,396 ppb total As. Also, this represents 83 % removal for total inorganic As. This calculation was made by the assumption that the remaining 70.34 % total arsenic is inorganic due to the volatility of the alkyl substituted arsines. There is some error involved in this yield due to the assumption that all As mainly consists of volatile low boiling compounds.

Table 7.7 ICP-OES results for total arsenic

| Sample ID | As (total) (ppb) | % Removal |
|---|------------------|-----------|
| Condensate Stock | 1,396 ± 4 | - |
| 1g ABDTH ₂ @MNP Condensate Tank 2 | 584 ± 8 | 58 |
| Condensate Evap-Refill | 982 ± 5 | 30 |

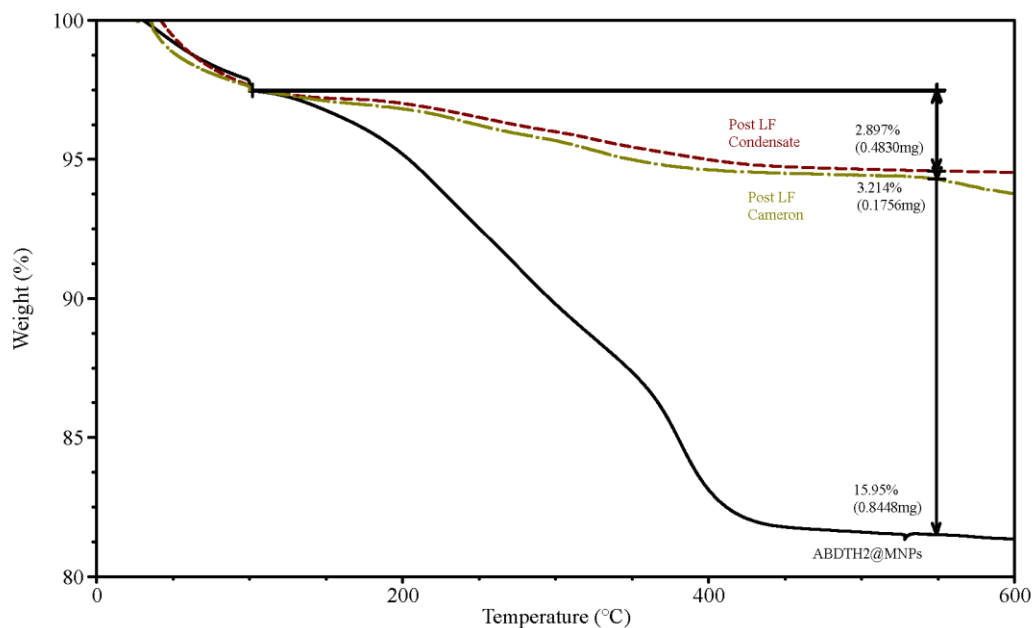
The solution from the redissolved solids was further investigated for the presence of arsenite, arsenate, and dimethylarsinate or cacodylic acid with IC. The 29.66% loss of total As likely resulted from the evaporation of alkylarsenic species however the exact identification was not made. The remaining As species was assumed to be some form of inorganic arsenic. Arsenite was not identifiable with IC with a carbonate buffer eluent due to the high first pK_a of 9.2. Arsenate and dimethylarsinate were below the detection limit of the lowest standard on the calibration curve (0.4 ppm). The redissolved condensate solution was condensed to both 5X and 10X concentrations to evaluate the increase in arsenate. However, the concentrated solutions resulted in a significant increase in total sulfate area that broadened into the expected retention time (24 min) for arsenate. Due to these complications, the concentration of arsenite, arsenate, and dimethylarsinate were not determined for the redissolved condensate.

Table 7.8 ICP-OES results for the 1g scale Cameron LF solution

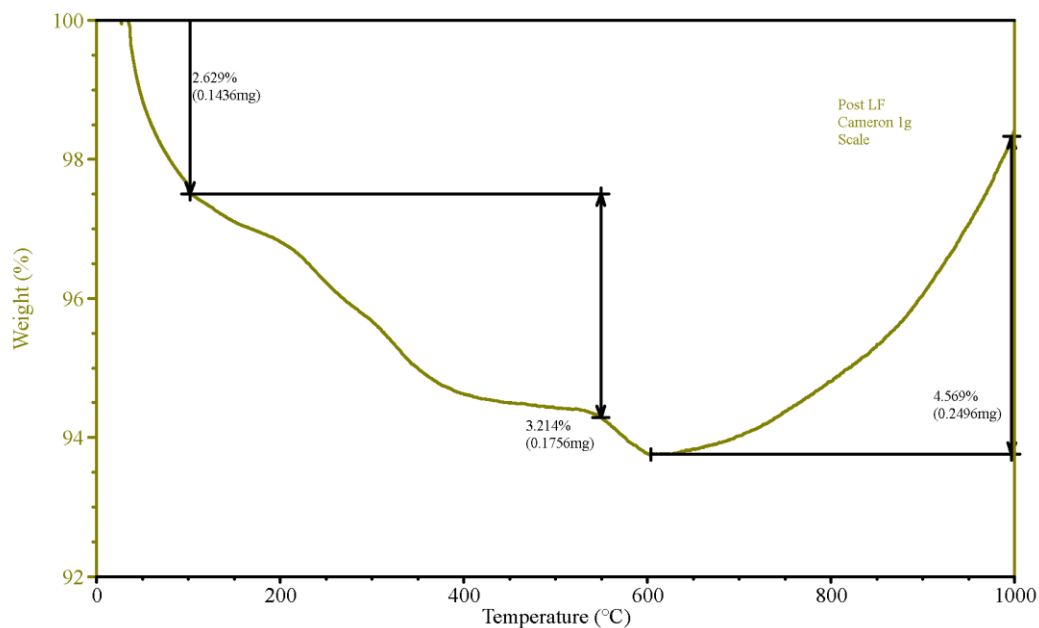
| Sample ID | As (total) (ppb) | % Removal |
|--------------------|------------------|-----------|
| Cameron Stock | 8,016 | - |
| 1g AB9@MNP Cameron | 7,578 | 5.5 |

Table 7.8 lists the ICP-OES results for the Cameron solutions. These solutions consist of water collected from scrubber blow down during the removal of sulfide.¹⁷⁶ The Cameron stock concentration was extremely high, 8,016 ppb total As, and representative of a very difficult industrial waste solution for remediation. Even 1g loadings of ABDTH₂@MNPs resulted in little removal of total As. However, the removal was similar to the large-scale loading with the redissolved condensate solution. Interference in

sequestration from of other sulfhydryl compounds from the production of sulfur, sulfate, and thiosulphate represents a serious challenge to the design of As removal strategies for these solutions. Aqueous solutions derived from the Cameron process have not been fully characterized in the literature. There is a large gap in the detailed analysis of these solutions that contain high levels of total As.



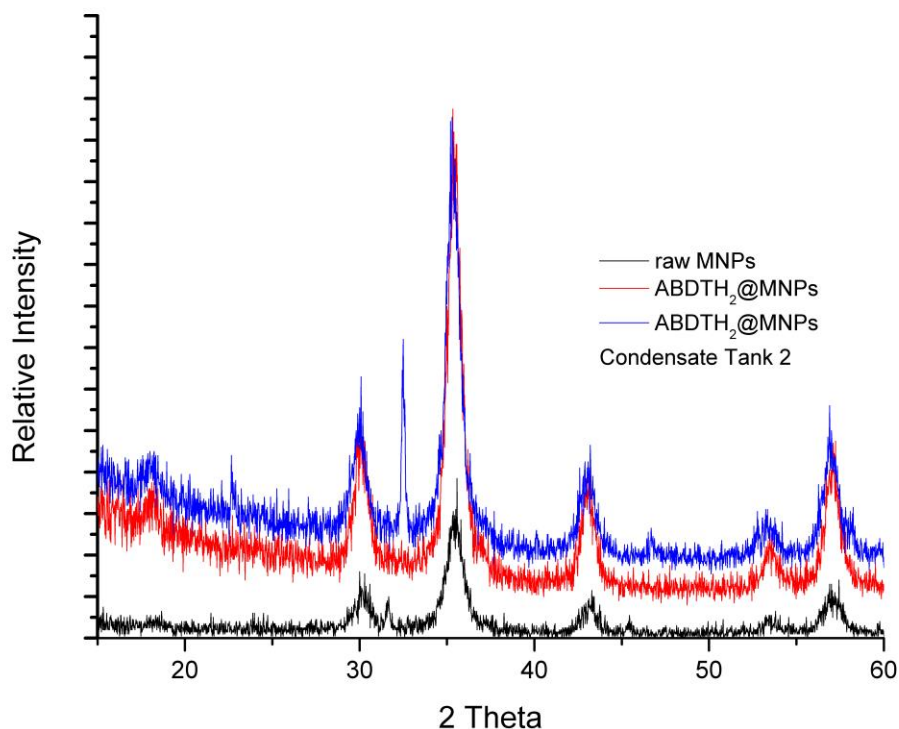
Graph 7.1 TGA results for ABDTH₂@MNPs (black solid), condensate treated MNPs (maroon, short dash), and Cameron treated MNPs (brown, long short dash)



Graph 7.2 TGA results for the 1g scale Cameron treated LF solution

The TGA shown in Graph 7.1 displays the typical result of treatment with ABDTH₂@MNPs after each sequential batch study. The pungent water completely removed all traces of passivated ABDTH₂ from the surface of the MNPs. ABDTH₂ was filtered off as a white precipitate. Moreover, the TGA for the Cameron treated ABDTH₂@MNPs gained significant mass after heating past 600 °C indicative of oxide bond formation to the MNP surface. Ligand exchange at the MNP surface is reversible with the carboxylate of ABDTH₂ as demonstrated with other surface passivated groups such as oleic and citric acid.¹⁸¹ Anionic interference of As(III) and As(V) with MNPs occurs in the combined presence of other ions.¹⁸² These results highlight the large discrepancy of benchtop removal strategies. Dissolved organic solids and high ionic strength solutions over broad ranges should be a strategic focus for As removal strategies moving forward.

Graph 7.3 shows the XRD results for the treated and untreated ABDTH₂ MNPs. The main diffraction peaks were retained after treatment of ABDTH₂@MNPs with the condensate solution. There were additional peaks at $2\theta = 23, 33,$ and 47 not present in ABDTH₂@MNPs. The most likely anion responsible for these peaks is silicate. However, peak assignment was not determined after scanning many potential adsorbed anions and potential oxidation products with database searches.



Graph 7.3 XRD results for raw MNPs (black), ABDTH₂@MNPs (red), and ABDTH₂@MNPs condensate tank 2 (blue)

7.3 Experimental

7.3.1 Reagents

The synthesis of BDTH₂, ABDTH₂, and ABDTH₂@MNPs was covered in Chapter 2.2 and 4.2. The condensate and Cameron solutions were provided by a private chemical engineering firm representing the interests of an active biogas mining facility in New Jersey. The following reagents and solvents were obtained commercially and used as received: hydrogen peroxide (30 %) from Sigma Aldrich; Omnitrace hydrochloric acid (HCl), ammonium hydroxide (NH₄OH), and nitric acid (HNO₃) from EMD; solvents from PHARMCO-AAPER; water was distilled and deionized (18 MΩ cm).

7.3.2 Analytical Techniques

In general, the condensate and Cameron solutions were repeatedly filtered with normal filter paper until no solids remained on the filter media. Thermogravimetric analysis (TGA) was obtained on a TA instrument 2950 TGA HR V5.4A from 30°C to 1000°C under nitrogen. A custom method was developed: a ramp of 5°C per minute until 100 °C, isothermal for 30 minutes, then an additional ramp of 5 °C to 1000 °C. The concentrations of arsenic (188.9 nm) were obtained using a Varian Vista-Pro CCD Simultaneous ICP-OES. Yttrium internal standard was used (371.029 nm) to evaluate and/or correct for matrix effects. Laboratory control samples (LCS) were produced with diluted elemental standards in 1% HNO₃. Digestions were done with 1% HNO₃, and heated if necessary to remove organics. Before ICP-OES analysis each sample was repeatedly filtered by micro-syringe filtration (0.45 and 0.2 μm). X-ray powder diffraction (XRD) was obtained using a Bruker-AXS D8 Discover Diffractometer from

10° to 80° (2θ) with step increments of 0.100° in 6s at 25 °C. Ion chromatography was performed on a Dionex ICS 2500 using an IonPac AS18 column preceded by an AS18 guard column with a 28 mM sodium carbonate eluent solution.

7.4 Synthesis

7.4.1 Determination of Arsenic in Condensate Solutions

The solutions were acidified with 1% HNO₃ and repeatedly filtered to remove white precipitates. The final volume was diluted with water to the original volume. For the extraction, condensate solution (500 mL) was extracted with either ethyl acetate (1L) or acetonitrile (1L).

7.4.2 Arsenic Removal from Condensate Solutions with BDTH₂ and ABDTH₂

The condensate (50 mL) was combined with both BDTH₂ (500 eq: 200 mg, 0.703 mmol; 1000 eq: 400 mg, 1.41 mmol) and ABDTH₂ (500 eq: 262 mg, 0.703 mmol; 1000 eq: 524 mg, 1.41 mmol) in EtOH (50 mL). After each addition both solutions precipitated white solids. The solutions were stirred for 12 h, filtered by vacuum filtration, and acidified with 1% HNO₃.

7.4.3 Arsenic Removal from Condensate Solutions with BDTH₂ and ABDTH₂ as a Function of pH

The pH was adjusted with either dilute HNO₃ or NH₄OH. The condensate (50 mL) was combined with both BDTH₂ (200 mg, 0.703 mmol) and ABDTH₂ (262 mg, 0.703 mmol) in EtOH (50 mL). After each addition both solutions precipitated white solids. The

solutions were stirred for 12 h, filtered by vacuum filtration, and acidified with 1% HNO₃.

7.4.4 Arsenic Removal from Condensate Solutions with ABDTH@MNPs

The stock solutions were diluted with deionized water to the required volume and the pH was adjusted to 9.0. Hydrogen peroxide (0.1 μL) was added for several batch studies. The condensate solutions (50 mL) were combined with ABDTH₂@MNPs (150 mg or 300 mg) and stirred for 12 h. The suspension was isolated by magnetic filtration.

7.4.5 Arsenic Removal from Redissolved Condensate – Large Scale ABDTH₂@MNP

The filtered solution (500 mL) was evacuated under vacuum at >100 °C for 6 h until total evaporation of the filtrate. A dark oily residue remained after evacuation. The solid was redissolved to the original volume with DI water (500 mL) and sonicated until no precipitate remained. The redissolved condensate (50 mL) was combined with ABDTH₂@MNPs (1g) and stirred for 12 h. The suspension was isolated by magnetic filtration.

7.4.6 Arsenic Removal from Cameron Solutions with ABDTH₂@MNPs

The Cameron solution (50 mL) was combined with ABDTH₂@MNPs (1g) and stirred for 12 h. The suspension was isolated by magnetic filtration.

7.5 Conclusions

The presence of alkyl substituted arsines complicates an effective approach to the removal process. Here, BDTH₂ and ABDTH₂ were capable of arsenic removal from these industrial solutions. However, removal required a large excess of ligand compared to

total arsenic. The low solubility in organic solvents and high solubility in water complicates arsenic identification. The ability of BDTH₂ and ABDTH₂ to remove any arsenic suggests that significant amounts consist of As(III). BDTH₂ and ABDTH₂ are very ineffective for the removal of As(V) from aqueous solution. Similar increases in loadings were required with ABDTH₂@MNPs. Neither bonding modes present for ABDTH₂@MNP are effective for removal of alkyl substituted arsines. Thiolate bond formation to As(III) and surface complex formation with As-O-Fe type bonds do not replace CH_X-As bonds. These solutions represent true challenges to the design of technologies for As remediation and highlight the discrepancies often reported without such complex intangible variables (lab quality solutions).

Chapter 8 Conclusions

There have been advancements in the number of different materials with high binding affinities for various toxic ions in aqueous solutions. However, the threat to humans from exposure remains a serious challenge for implementing a system that incorporates low-cost, mitigates environmental impact, and incorporates ease in the recycling of spent filtration media. A “one size fits all” approach seems misguided regarding filtration design. Multistage filtration solutions that average together to cover a broad spectrum of potential toxins are better suited for applications in areas such as southeastern Asia. This was the rationale behind the SONOS and KanchanTM filter designs. Unfortunately, these sequestration solutions are still not 100% safe and reliable.⁵³⁻⁵⁴

This research sought to address these issues by establishing a series of methods that operate based on the reactivity of sulfhydryl groups to remove various forms of arsenic from aqueous solutions. Both bidentate sulfhydryl compounds BDTH₂ and ABDTH₂ demonstrated high affinities for As(III). Each precipitate As(III) from solution as an insoluble product with yields from 82-87%. The insoluble product is a requirement for their use as precipitation chelates for the treatment of high-risk solutions containing As(III). Unfortunately, this also increases the difficulties of structure determination with routine characterization techniques. Moving forward with this project several different approaches should be considered to increase solubility in common organic solvents for a complete characterization. For example, sulfhydryl exchange chemistry is a dynamic equilibrium for a broad range of substrates. Exchange with dithiols and other metal ions function biologically for several different critical processes. This equilibrium can be exploited to incorporate different properties into the BDT-As(III) and ABDT-As(III) products. This transformation could be accessed either during or post-precipitation of As(III). Both precipitation products contained stable S-As(III) bonds, but other “soft” metal ions in solution could be incorporated in the product per trends in HSAB theory. The reverse process with sulfhydryl groups replacing S-As(III) bonds from the ABDT-As(III) product may result in enhanced solubility in common organic solvents. For example, long chain alkyl sulfhydryl compounds could be introduced to increase solubility in solvents such as toluene. The inability of both BDTH₂ and ABDTH₂ to bind As(V) was also demonstrated. Neither was an effective active redox reactant for the reduction to As(III).

After establishing that ABDTH₂ was an effective remediation chelate for As(III) through S-As(III) bond formation, the ligand was bound to solid support media to offer increased removal compared to normal adsorption. Various derivatives of ABDTH₂ MNPs were effective in removing As(III) in a broad pH range and when mixed with other anions in solution. The sulfhydryl groups in ABDTH₂ interacted with As(III) in accordance with HSAB theory. The inclusion of sulfhydryl based strategies offers an enhancement to effective remediation of As(III) in a range of ionic strengths compared to adsorption with metal oxides. However, oxidation of typical sulfhydryl groups is an issue regarding long-term stability in solution, but here dithiol formation was not an issue. The ability to quickly filter ABDTH₂ MNPs was demonstrated with computer hard drive magnets. Interestingly, ABDTH₂ bound directly to the surface of bare MNPs compared to the silica core-shell variants was nearly twice as magnetic. Silica core-shell formation was the limiting step in the formation of ABDTH₂ MNPs regarding magnetic saturation. The thermodynamics of the S-As(III) bond formation were also evaluated using flow cell calorimetry. ABDTH₂ had exothermic enthalpies when mixed with As(III) and compared similarly to other bidentate sulfhydryl arsenite complexes measured with potentiometric titrations. Thus the covalent removal through stable S-As(III) bonds was demonstrated with ABDTH₂ bound to solid media.

The performance of filtration media in laboratory solutions that lack multiple variables can be impractical regarding real applications. Here this system was evaluated with crude industrial solutions from the production of biogas from an active landfill. These solutions were difficult to work with due to the elaborate matrix. However, both BDTH₂, ABDTH₂, and ABDTH₂@MNPs demonstrated arsenic removal from batch

studies with these solutions. High loadings of the chelates and MNPs removed more arsenic from the solutions than had previously been measured with activated carbon and alumina. The difficulties encountered with these industrial solutions represent serious challenges to arsenic remediation strategies. The ability of these materials to remove arsenic is a testament to the high binding affinity seen with arsenic and sulfur. This system mimics the abundance of natural chemistry observed between the two elements in both biologic and geologic environments.

This research will hopefully inspire new technologies based on the design of novel molecular architectures with multidentate sulfhydryl groups and other hybrid solid-state media. For example, derivatives of ABDTH₂ could be synthesized through amide bond formation with reagents such as cysteamine. The tetradentate ligand would be capable of increased removal capacity. Transformations that incorporate low-cost and mitigate environmental impact will be a necessity moving forward with hybrid filtration media. As an example, native chemical ligation (NCL) is an emerging pathway for functionalizing solid-state media with sulfhydryl groups. NCL is an elegant route for overcoming the difficulties associated with amide bond formation that excludes the need for traditional coupling reagents. MNPs could easily be functionalized with this method and benefit from the low-cost of synthetic transformations in addition to the ease of filtration due to the magnetic properties. These examples illustrate only a few of the total possibilities that exist for engineering solutions to the complex problems associated with exposure to toxins in aqueous solutions. There is a critical need for increased research in these areas due to the magnitude of people affected and the burdens of remediation.

References

1. Lau, K. H.; Brittain, R. D.; Hildenbrand, D. L., Vaporization of As_2S_3 and the Dissociation Energy of AsS. *J. Phys. Chem.* **1982**, *86*, 4429-4432.
2. Cullen, W. R.; Reimer, K. J., Arsenic speciation in the environment. *Chem. Rev.* **1989**, *89* (4), 713-764.
3. Smedley, P. L.; Kinniburgh, D. G., A review of the source, behaviour and distribution of arsenic in natural waters. *Appl. Geochem.* **2002**, *17* (5), 517-568.
4. Masscheleyn, P. H.; Delaune, R. D.; Patrick, W. H., Effect of redox potential and pH on arsenic speciation and solubility in a contaminated soil. *Environ. Sci. Technol.* **1991**, *25* (8), 1414-1419.
5. Kolozsi, A.; Lakatos, A.; Galbács, G.; Madsen, A. Ø.; Larsen, E.; Gyurcsik, B., A pH-Metric, UV, NMR, and X-ray Crystallographic Study on Arsenous Acid Reacting with Dithioerythritol. *Inorg. Chem.* **2008**, *47* (9), 3832-3840.
6. Ezeh, V. C.; Patra, A. K.; Harrop, T. C., Four-Coordinate As^{III}-N,S Complexes: Synthesis, Structure, Properties, and Biological Relevance. *Inorg. Chem.* **2010**, *49* (6), 2586-2588.
7. Miodragović, Đ. U.; Quentzel, J. A.; Kurutz, J. W.; Stern, C. L.; Ahn, R. W.; Kandela, I.; Mazar, A.; O'Halloran, T. V., Robust Structure and Reactivity of Aqueous Arsenous Acid-Platinum(II) Anticancer Complexes. *Angew. Chem. Int. Ed.* **2013**, *52* (41), 10749-10752.
8. Gupta, R. K.; Rai, A. K.; Mehrotra, R. C.; Jain, V. K.; Hoskins, B. F.; Tiekink, E. R. T., Phenylarsenic(III) and phenylantimony(III) bis(dialkyl dithiophosphates): synthesis and multinuclear (proton, carbon-13, phosphorus-31) NMR and mass spectral studies.

Crystal and molecular structures of $C_6H_5M[S_2P(OCHMe_2)_2]_2$ [$M = Sb(III)$ and $As(III)$]. *Inorg. Chem.* **1985**, *24* (20), 3280-3284.

9. Norrby, L. J., Why is mercury liquid? Or, why do relativistic effects not get into chemistry textbooks? *J. Chem. Educ.* **1991**, *68* (2), 110.
10. Scott, N.; Hatlelid, K. M.; MacKenzie, N. E.; Carter, D. E., Reactions of arsenic(III) and arsenic(V) species with glutathione. *Chem. Res. Toxicol.* **1993**, *6*, 102.
11. Rey, N. A.; Howarth, O. W.; Pereira-Maia, E. C., Equilibrium characterization of the $As(III)$ -cysteine and the $As(III)$ -glutathione systems in aqueous solution. *J. Inorg. Biochem.* **2004**, *98* (6), 1151-1159.
12. Ajees, A. A.; Marapakala, K.; Packianathan, C.; Sankaran, B.; Rosen, B. P., Structure of an $As(III)$ S-Adenosylmethionine Methyltransferase: Insights into the Mechanism of Arsenic Biotransformation. *Biochemistry* **2012**, *51* (27), 5476-5485.
13. Shaikh, T. A.; Bakus II, R. C.; Parkin, S.; Atwood, D. A., Structural characteristics of 2-halo-1,3,2-dithiarsenic compounds and tris-(pentafluorophenylthio)-arsen. *J. Organomet. Chem.* **2006**, *691* (9), 1825-1833.
14. DeGraffenreid, A. J.; Feng, Y.; Wycoff, D. E.; Morrow, R.; Phipps, M. D.; Cutler, C. S.; Ketring, A. R.; Barnes, C. L.; Jurisson, S. S., Dithiol Aryl Arsenic Compounds as Potential Diagnostic and Therapeutic Radiopharmaceuticals. *Inorg. Chem.* **2016**, *55* (16), 8091-8098.
15. Farrer, B. T.; McClure, C. P.; Penner-Hahn, J. E.; Pecoraro, V. L., Arsenic(III)-Cysteine Interactions Stabilize Three-Helix Bundles in Aqueous Solution. *Inorg. Chem.* **2000**, *39* (24), 5422-5423.

16. Cline, D. J.; Thorpe, C.; Schneider, J. P., Effects of As(III) Binding on α -Helical Structure. *J. Am. Chem. Soc.* **2003**, *125* (10), 2923.
17. Naranmandura, H.; Suzuki, N.; Suzuki, K. T., Trivalent Arsenicals Are Bound to Proteins during Reductive Methylation. *Chem. Res. Toxicol.* **2006**, *19* (8), 1010-1018.
18. Ramadan, D.; Cline, D. J.; Bai, S.; Thorpe, C.; Schneider, J. P., Effects of As(III) Binding on β -Hairpin Structure. *J. Am. Chem. Soc.* **2007**, *129* (10), 2981-2988.
19. Shen, S.; Li, X. F.; Cullen, W. R.; Weinfeld, M.; Le, X. C., Arsenic Binding to Proteins. *Chem. Rev.* **2013**, *113* (10), 7769-7792.
20. Zhao, L.; Wang, Z.; Xi, Z.; Xu, D.; Chen, S.; Liu, Y., The Reaction of Arsenite with Proteins Relies on Solution Conditions. *Inorg. Chem.* **2014**, *53* (6), 3054-3061.
21. Wilson, P.; Anastasaki, A.; Owen, M. R.; Kempe, K.; Haddleton, D. M.; Mann, S. K.; Johnston, A. P. R.; Quinn, J. F.; Whittaker, M. R.; Hogg, P. J.; Davis, T. P., Organic Arsenicals As Efficient and Highly Specific Linkers for Protein/Peptide-Polymer Conjugation. *J. Am. Chem. Soc.* **2015**, *137* (12), 4215-4222.
22. Ajees, A. A.; Marapakala, K.; Packianathan, C.; Sankaran, B.; Rosen, B. P., The structure of an As(III) S-adenosylmethionine methyltransferase: insights into the mechanism of arsenic biotransformation. *Biochemistry* **2012**, *51* (27), 5476-5485.
23. Hill, N. J.; Levason, W.; Reid, G., Arsenic(III) Halide Complexes with Acyclic and Macrocyclic Thio- and Selenoether Coligands: Synthesis and Structural Properties. *Inorg. Chem.* **2002**, *41* (8), 2070-2076.
24. Adams, E.; Jeter, D.; Cordes, A. W.; Kolis, J. W., Chemistry of organometalloid complexes with potential antidotes: structure of an organoarsenic(III) dithiolate ring. *Inorg. Chem.* **1990**, *29* (8), 1500-1503.

25. Shaikh, T. A.; Parkin, S.; Atwood, D. A., Synthesis and characterization of a rare arsenic trithiolate with an organic disulfide linkage and 2-chloro-benzo-1,3,2-dithiastibole. *J. Organomet. Chem.* **2006**, *691* (20), 4167-4171.
26. Dollen, A. V.; Strasdeit., H., Models for the Inhibition of Dithiol-Containing Enzymes by Organoarsenic Compounds: Synthetic Routes and the Structure of [PhAs(HlipS₂)] (HlipS₂⁻ = Reduced Lipoic Acid). *Eur. J. Inorg. Chem* **1998**, *1998* (1), 61-66.
27. Cullen, W. R., Chemical Mechanism of Arsenic Biomethylation. *Chem. Res. Toxicol.* **2014**, *27* (4), 457-461.
28. Suzuki, K. T.; Katagiri, A.; Sakuma, Y.; Ogra, Y.; Ohmichi, M., Distributions and chemical forms of arsenic after intravenous administration of dimethylarsinic and monomethylarsonic acids to rats. *Toxicol. Appl. Pharmacol.* **2004**, *198* (3), 336-344.
29. Lin, S.; Cullen, W. R.; Thomas, D., Methylarsenicals and Arsinothiols Are Potent Inhibitors of Mouse Liver Thioredoxin Reductase. *J. Chem. Res. Toxicol.* **1999**, *12* (10), 924-930.
30. Wang, Q. Q.; Thomas, D. J.; Naranmandura, H., Importance of Being Thiomethylated: Formation, Fate, and Effects of Methylated Thioarsenicals. *Chem. Res. Toxicol.* **2015**, *28* (3), 281-289.
31. Kala, S. V.; Neely, M. W.; Kala, G.; Prater, C. I.; Atwood, D. W.; Rice, J. S.; Lieberman, M. W., The MRP2/cMOAT Transporter and Arsenic-Glutathione Complex Formation Are Required for Biliary Excretion of Arsenic. *J. Biol. Chem.* **2000**, *275*, 33404.

32. Bellomo, G.; Vairetti, M.; Stivala, L.; Mirabelli, F.; Richelmi, P.; Orrenius, S., Demonstration of nuclear compartmentalization of glutathione in hepatocytes. *Proceedings of the National Academy of Sciences of the United States of America* **1992**, *89* (10), 4412-4416.
33. Scott, N.; Hatlelid, K. M.; MacKenzie, N. E.; Carter, D. E., Reactions of Arsenic(III) and Arsenic(V) Species with Glutathione. *Chem. Res. Toxicol.* **1993**, *6*, 102-106.
34. Delnomdedieu, M.; Basti, M. M.; Otvos, J. D.; Thomas, D. J., Transfer of arsenite from glutathione to dithiols: A model of interaction. *Chem. Res. Toxicol.* **1993**, *6* (5), 598-602.
35. Dill, K.; Adams, E. R.; O'Connor, R. J.; Chong, S.; McGown, E. L., One-dimensional and two-dimensional nuclear magnetic resonance studies of the reaction of phenyldichloroarsine with glutathione. *Arch. Biochem. Biophys.* **1987**, *257* (2), 293-301.
36. Pereira, F. J.; Vázquez, M. D.; Debán, L.; Aller, A. J., Spectrometric characterisation of the solid complexes formed in the interaction of cysteine with As(III), Th(IV) and Zr(IV). *Polyhedron* **2014**, *76*, 71-80.
37. Moggach, S. A.; Allan, D. R.; Clark, S. J.; Gutmann, M. J.; Parsons, S.; Pulham, C. R.; Sawyer, L., High-pressure polymorphism in l-cysteine: the crystal structures of l-cysteine-III and l-cysteine-IV. *Acta Crystallogr. B.* **2006**, *62* (2), 296-309.
38. Cruse, W. B. T., James M. N. G. , The crystal structure of arsenite complex with dithiothreitol. *Acta. Crystallogr.* **1972**, *B28*, 1325-1331.

39. Ezeh, V. C.; Harrop, T. C., Synthesis and Properties of Arsenic(III)-Reactive Coumarin-Appended Benzothiazolines: A New Approach for Inorganic Arsenic Detection. *Inorg. Chem.* **2013**, *52* (5), 2323-2334.
40. Sokolov, M. N.; Virovets, A. V.; Dybtsev, D. N.; Chubarova, E. V.; Fedin, V. P.; Fenske, D., Phosphorous Acid and Arsenious Acid as Ligands. *Inorg. Chem.* **2001**, *40* (19), 4816-4817.
41. Hernández-Molina, R.; Sokolov, M. N.; Clausen, M.; Clegg, W., Synthesis and Structure of Nickel-Containing Cuboidal Clusters Derived from $[W_3Se_4(H_2O)_9]^{4+}$. Site-Differentiated Substitution at the Nickel Site in the Series $[W_3NiQ_4(H_2O)_{10}]^{4+}$ (Q = S, Se). *Inorg. Chem.* **2006**, *45* (26), 10567-10575.
42. Ali, I., New Generation Adsorbents for Water Treatment. *Chem. Rev.* **2012**, *112* (10), 5073-5091.
43. Chen, B.; Lu, X.; Arnold, L. L.; Cohen, S. M.; Le, X. C., Identification of Methylated Dithioarsenicals in the Urine of Rats Fed with Sodium Arsenite. *Chem. Res. Toxicol.* **2016**, *29* (9), 1480-1487.
44. Mohan, D.; Pittman Jr, C. U., Arsenic removal from water/wastewater using adsorbents—A critical review. *J. Hazard. Mater.* **2007**, *142* (1–2), 1-53.
45. Nordstrom, D.; Archer, D., Arsenic thermodynamic data and environmental geochemistry. Arsenic in Ground Water. Welch, A. H.; Stollenwerk, K. G., Eds. Springer US: 2003; pp 1-25.
46. Stollenwerk, K., Geochemical Processes Controlling Transport of Arsenic in Groundwater: A Review of Adsorption. Arsenic in Ground Water. Welch, A. H.; Stollenwerk, K. G., Eds. Springer US: 2003; pp 67-100.

47. Dixit, S.; Hering, J. G., Comparison of Arsenic(V) and Arsenic(III) Sorption onto Iron Oxide Minerals: Implications for Arsenic Mobility. *Environ. Sci. Technol.* **2003**, *37* (18), 4182-4189.
48. Meng, X.; Bang, S.; Korfiatis, G. P., Effects of silicate, sulfate, and carbonate on arsenic removal by ferric chloride. *Water Res.* **2000**, *34* (4), 1255-1261.
49. Sabur, M. A.; Goldberg, S.; Gale, A.; Kabengi, N.; Al-Abadleh, H. A., Temperature-Dependent Infrared and Calorimetric Studies on Arsenicals Adsorption from Solution to Hematite Nanoparticles. *Langmuir* **2015**, *31* (9), 2749-2760.
50. Meng, X.; Korfiatis, G. P.; Bang, S.; Bang, K. W., Combined effects of anions on arsenic removal by iron hydroxides. *Toxicol. Lett.* **2002**, *133* (1), 103-111.
51. Peryea, F.; Kammereck, R., Phosphate-enhanced movement of arsenic out of lead arsenate-contaminated topsoil and through uncontaminated subsoil. *Water Air Soil Pollut.* **1997**, *93* (1), 243-254.
52. Daus, B.; Wennrich, R.; Weiss, H., Sorption materials for arsenic removal from water:: a comparative study. *Water Res.* **2004**, *38* (12), 2948-2954.
53. Giles, D. E.; Mohapatra, M.; Issa, T. B.; Anand, S.; Singh, P., Iron and aluminium based adsorption strategies for removing arsenic from water. *J. Environ. Manage.* **2011**, *92* (12), 3011-3022.
54. Singh, A.; Smith, L. S.; Shrestha, S.; Maden, N., Efficacy of arsenic filtration by Kanchan Arsenic Filter in Nepal. *J. Water Health* **2014**, *12* (3), 596.
55. Deliyanni, E. A. B., D. A.; Zouboulis, Al, Matis, K. A., Sorption of As(V) ions by akaganéite-type nanocrystals. *Chemosphere* **2003**, *50* (1), 155-163.

56. Kim, Y.; Kim, C.; Choi, I.; Rengaraj, S.; Yi, J., Arsenic Removal Using Mesoporous Alumina Prepared via a Templating Method. *Environ. Sci. Technol.* **2003**, *38* (3), 924-931.
57. Borah, D.; Satokawa, S.; Kato, S.; Kojima, T., Surface-modified carbon black for As(V) removal. *J. Colloid Interf. Sci.* **2008**, *319* (1), 53-62.
58. Ladeira, A. C. Q.; Ciminelli, V. n. S. T., Adsorption and desorption of arsenic on an oxisol and its constituents. *Water Res.* **2004**, *38* (8), 2087-2094.
59. Yoshitake, H.; Yokoi, T.; Tatsumi, T., Adsorption Behavior of Arsenate at Transition Metal Cations Captured by Amino-Functionalized Mesoporous Silicas. *Chem. Mater.* **2003**, *15* (8), 1713-1721.
60. Bang, S.; Patel, M.; Lippincott, L.; Meng, X., Removal of arsenic from groundwater by granular titanium dioxide adsorbent. *Chemosphere* **2005**, *60* (3), 389-397.
61. Gu, Z.; Fang, J.; Deng, B., Preparation and Evaluation of GAC-Based Iron-Containing Adsorbents for Arsenic Removal. *Environ. Sci. Technol.* **2005**, *39* (10), 3833-3843.
62. Lenoble, V.; Bouras, O.; Deluchat, V.; Serpaud, B.; Bollinger, J.-C., Arsenic Adsorption onto Pillared Clays and Iron Oxides. *J. Colloid Interf. Sci.* **2002**, *255* (1), 52-58.
63. Kanel, S. R.; Manning, B.; Charlet, L.; Choi, H., Removal of Arsenic(III) from Groundwater by Nanoscale Zero-Valent Iron. *Environ. Sci. Technol.* **2005**, *39* (5), 1291-1298.

64. Yavuz, C. T.; Mayo, J. T.; Yu, W. W.; Prakash, A.; Falkner, J. C.; Yean, S.; Cong, L.; Shipley, H. J.; Kan, A.; Tomson, M.; Natelson, D.; Colvin, V. L., Low-Field Magnetic Separation of Monodisperse Fe₃O₄ Nanocrystals. *Science*. **2006**, *314* (5801), 964-967.
65. Viraka Nellore, B. P.; Kanchanapally, R.; Pedraza, F.; Sinha, S. S.; Pramanik, A.; Hamme, A. T.; Arslan, Z.; Sardar, D.; Ray, P. C., Bio-Conjugated CNT-Bridged 3D Porous Graphene Oxide Membrane for Highly Efficient Disinfection of Pathogenic Bacteria and Removal of Toxic Metals from Water. *ACS Appl. Mater. Inter.* **2015**, *7* (34), 19210-19218.
66. Tong, R.; Tang, L.; Ma, L.; Tu, C.; Baumgartner, R.; Cheng, J., Smart chemistry in polymeric nanomedicine. *Chem. Soc. Rev.* **2014**, *43* (20), 6982-7012.
67. Yilmaz, E.; Garipcan, B.; Patra, H.; Uzun, L., Molecular Imprinting Applications in Forensic Science. *Sensors* **2017**, *17* (4), 691.
68. Fan, H.-T.; Fan, X.; Li, J.; Guo, M.; Zhang, D.; Yan, F.; Sun, T., Selective Removal of Arsenic(V) from Aqueous Solution Using A Surface-Ion-Imprinted Amine-Functionalized Silica Gel Sorbent. *Ind. Eng. Chem. Res.* **2012**, *51* (14), 5216-5223.
69. Moghimi, N.; Mohapatra, M.; Leung, K. T., Bimetallic Nanoparticles for Arsenic Detection. *Anal. Chem.* **2015**.
70. Feng, Z.; Zhu, S.; Martins de Godoi, D. R.; Samia, A. C. S.; Scherson, D., Adsorption of Cd²⁺ on Carboxyl-Terminated Superparamagnetic Iron Oxide Nanoparticles. *Anal. Chem.* **2012**, *84* (8), 3764-3770.

71. He, F.; Wang, W.; Moon, J.-W.; Howe, J.; Pierce, E. M.; Liang, L., Rapid Removal of Hg(II) from Aqueous Solutions Using Thiol-Functionalized Zn-Doped Biomagnetite Particles. *ACS Appl. Mater. Inter.* **2012**, *4* (8), 4373-4379.
72. Fauconnier, N.; Pons, J. N.; Roger, J.; Bee, A., Thiolation of Maghemite Nanoparticles by Dimercaptosuccinic Acid. *J. Colloid Interf. Sci.* **1997**, *194* (2), 427-433.
73. Zhang, L.; Wang, X.; Zou, J.; Liu, Y.; Wang, J., DMSA-Coated Iron Oxide Nanoparticles Greatly Affect the Expression of Genes Coding Cysteine-Rich Proteins by Their DMSA Coating. *Chem. Res. Toxicol.* **2015**, *28* (10), 1961-1974.
74. Yang, J.; Zhang, Y.; Gautam, S.; Liu, L.; Dey, J.; Chen, W.; Mason, R. P.; Serrano, C. A.; Schug, K. A.; Tang, L., Development of aliphatic biodegradable photoluminescent polymers. *Proceedings of the National Academy of Sciences of the United States of America* **2009**, *106* (25), 10086-10091.
75. Karim, M. M., Arsenic in groundwater and health problems in Bangladesh. *Water Res.* **2000**, *34* (1), 304-310.
76. Guan, X.; Dong, H.; Ma, J.; Jiang, L., Removal of arsenic from water: Effects of competing anions on As(III) removal in KMnO₄-Fe(II) process. *Water Res.* **2009**, *43* (15), 3891-3899.
77. Chauhan, K.; Singh, P.; Kumari, B.; Singhal, R. K., Synthesis of new benzothiazole Schiff base as selective and sensitive colorimetric sensor for arsenic on-site detection at ppb level. *Anal. Meth.* **2017**, *9* (11), 1779-1785.
78. Lohar, S.; Pal, S.; Sen, B.; Mukherjee, M.; Banerjee, S.; Chattopadhyay, P., Selective and Sensitive Turn-on Chemosensor for Arsenite Ion at the ppb Level in Aqueous Media Applicable in Cell Staining. *Anal. Chem.* **2014**, *86* (22), 11357-11361.

79. Tian, X.; Chen, L.; Li, Y.; Yang, C.; Nie, Y.; Zhou, C.; Wang, Y., Design and synthesis of a molecule with aggregation-induced emission effects and its application in the detection of arsenite in groundwater. *J. Mater. Chem. C* **2017**, *5* (15), 3669-3672.
80. Baglan, M.; Atlgan, S., Selective and sensitive turn-on fluorescent sensing of arsenite based on cysteine fused tetraphenylethene with AIE characteristics in aqueous media. *Chem. Commun.* **2013**, *49* (46), 5325-5327.
81. Takeda, N.; Tokitoh, N.; Okazaki, R., Synthesis, Structure, and Reactions of the First Rotational Isomers of Stable Thiobenzaldehydes, 2,4,6-Tris[bis(trimethylsilyl)methyl]thiobenzaldehydes. *Chem. Eur. J.* **1997**, *3* (1), 62-69.
82. Huber, K. P.; Herzberg, G., *Molecular Spectra and Molecular Structure Constants of Diatomic Molecules*. Van Nostrand: New York, 1979.
83. Bach, R. D.; Ayala, P. Y.; Schlegel, H. B., A Reassessment of the Bond Dissociation Energies of Peroxides. An ab Initio Study. *J. Am. Chem. Soc.* **1996**, *118* (50), 12758-12765.
84. Lumb, I.; Hundal, M. S.; Hundal, G., Copper(II)-Catalyzed Disulfide Scission—Stepwise Aerobic Oxidative Cleavage to Sulfinic and Sulfonic and Reductive Anaerobic Cleavage to Thiols. *Inorg. Chem.* **2014**, *53* (14), 7770-7779.
85. Esmieu, C.; Orio, M.; Le Pape, L.; Lebrun, C.; Pécaut, J.; Ménage, S.; Torelli, S., Redox-Innocent Metal-Assisted Cleavage of S–S Bond in a Disulfide-Containing Ligand. *Inorg. Chem.* **2016**, *55* (12), 6208-6217.
86. West, K. R.; Bake, K. D.; Otto, S., Dynamic Combinatorial Libraries of Disulfide Cages in Water. *Org. Lett.* **2005**, *7* (13), 2615-2618.

87. Winkel, L. B., M.; Amini, M.; Hug, S. J.; Johnson, C. A., Predicting groundwater arsenic contamination in Southeast Asia from surface parameters. *Nat. Geosci.* **2008**, *1* (8), 536-542.
88. Zou, W.; Filatov, M.; Atwood, D.; Cremer, D., Removal of Mercury from the Environment: A Quantum-Chemical Study with the Normalized Elimination of the Small Component Method. *Inorg. Chem.* **2013**, *52* (5), 2497-2504.
89. Matlock, M. M.; Howerton, B. S.; Atwood, D. A., Irreversible precipitation of mercury and lead. *J. Hazard. Mater.* **2001**, *84* (1), 73-82.
90. Matlock, M. M.; Howerton, B. S.; Atwood, D. A., Chemical precipitation of heavy metals from acid mine drainage. *Water Res.* **2002**, *36* (19), 4757-4764.
91. Matlock, M. M.; Howerton, B. S.; Van Aelstyn, M. A.; Nordstrom, F. L.; Atwood, D. A., Advanced Mercury Removal from Gold Leachate Solutions Prior to Gold and Silver Extraction: A Field Study from an Active Gold Mine in Peru. *Environ. Sci. Technol.* **2002**, *36* (7), 1636-1639.
92. Atwood, D. A.; Howerton, B. S.; Matlock, M., Multidentate sulfur-containing ligands. Google Patents: 2003.
93. Bharara, M. S.; Parkin, S.; Atwood, D. A., Mercury(II) 2-Aminoethanethiolate Clusters: Intramolecular Transformations and Mechanisms. *Inorg. Chem.* **2006**, *45* (18), 7261-7268.
94. Burriss, D.; Zou, W.; Cremer, D.; Walrod, J.; Atwood, D., Removal of Selenite from Water Using a Synthetic Dithiolate: An Experimental and Quantum Chemical Investigation. *Inorg. Chem.* **2014**, *53* (8), 4010-4021.

95. Guerrero, M.; Pons, J.; Ros, J.; Font-Bardia, M.; Branchadell, V., Anion Influence on the Structure of N,O-Hybrid Pyrazole ZnII, CdII, and HgII Complexes. Synthesis, Characterization, and Theoretical Studies. *Cryst. Growth Des.* **2012**, *12* (7), 3700-3708.
96. Matlock, M. M.; Howerton, B. S.; Henke, K. R.; Atwood, D. A., A pyridine-thiol ligand with multiple bonding sites for heavy metal precipitation. *J. Hazard. Mater.* **2001**, *82* (1), 55-63.
97. Lukesh, J. C.; Palte, M. J.; Raines, R. T., A Potent, Versatile Disulfide-Reducing Agent from Aspartic Acid. *J. Am. Chem. Soc.* **2012**, *134* (9), 4057-4059.
98. Pearson, R. G., Hard and soft acids and bases, HSAB, part 1: Fundamental principles. *J. Chem. Educ.* **1968**, *45* (9), 581.
99. Chaudhari, S.; Tare, V., Analysis and evaluation of heavy metal uptake and release by insoluble starch xanthate in aqueous environment. *Water Sci. Technol.* **1996**, *34* (10), 161-168.
100. Matlock, M. M.; Howerton, B. S.; Aelstyn, M. V.; Henke, K. R.; Atwood, D. A., Soft metal preferences of 1,3-benzenediamidoethanethiol. *Water Res.* **2003**, *37* (3), 579-584.
101. Ding, X.; Hua, Y.; Chen, Y.; Zhang, C.; Kong, X., Heavy Metal Complexation of Thiol-Containing Peptides from Soy Glycinin Hydrolysates. *Int. J. Mol. Sci.* **2015**, *16* (4), 8040-8058.
102. Matlock, M. M.; Howerton, B. S.; Robertson, J. D.; Atwood, D. A., Gold Ore Column Studies with a New Mercury Precipitant. *Ind. Eng. Chem. Res.* **2002**, *41* (21), 5278-5282.

103. Hoffmann, M.; Mikutta, C.; Kretzschmar, R., Arsenite Binding to Sulfhydryl Groups in the Absence and Presence of Ferrihydrite: A Model Study. *Environ. Sci. Technol.* **2014**, *48* (7), 3822-3831.
104. Raab, A.; Wright, S. H.; Jaspars, M.; Meharg, A. A.; Feldmann, J., Pentavalent Arsenic Can Bind to Biomolecules. *Angew. Chem. Int. Ed.* **2007**, *46* (15), 2594-2597.
105. Chen, B.; Cao, F.; Yuan, C.; Lu, X.; Shen, S.; Zhou, J.; Le, X. C., Arsenic speciation in saliva of acute promyelocytic leukemia patients undergoing arsenic trioxide treatment. *Anal. Bioanal. Chem.* **2013**, *405* (6), 1903-1911.
106. Contreras-Acuña, M.; García-Barrera, T.; García-Sevillano, M. A.; Gómez-Ariza, J. L., Arsenic metabolites in human serum and urine after seafood (*Anemonia sulcata*) consumption and bioaccessibility assessment using liquid chromatography coupled to inorganic and organic mass spectrometry. *Microchem. J.* **2014**, *112*, 56-64.
107. Cleland, W. W., Dithiothreitol, a New Protective Reagent for SH Groups*. *Biochemistry* **1964**, *3* (4), 480-482.
108. Mirzahosseini, A.; Noszál, B., Species-Specific Standard Redox Potential of Thiol-Disulfide Systems: A Key Parameter to Develop Agents against Oxidative Stress. *Sci. Rep.* **2016**, *6*, 37596.
109. Lees, W. J.; Whitesides, G. M., Equilibrium constants for thiol-disulfide interchange reactions: a coherent, corrected set. *J. Org. Chem.* **1993**, *58* (3), 642-647.
110. Bell, I. M.; Clark, R. J. H.; Gibbs, P. J., Raman spectroscopic library of natural and synthetic pigments (pre- \approx 1850 AD). *Spectrochimica Acta Part A: Molecular and Biomolecular Spectroscopy* **1997**, *53* (12), 2159-2179.

111. Teixeira, M. C.; Ciminelli, V. S. T.; Dantas, M. S. S.; Diniz, S. F.; Duarte, H. A., Raman spectroscopy and DFT calculations of As(III) complexation with a cysteine-rich biomaterial. *J. Colloid Interf. Sci.* **2007**, *315* (1), 128-134.
112. Bazylewski, P.; Divigalpitiya, R.; Fanchini, G., In situ Raman spectroscopy distinguishes between reversible and irreversible thiol modifications in l-cysteine. *RSC Advances* **2017**, *7* (5), 2964-2970.
113. Daigle, K., Death In The Water. *Sci. Am.* **2016**, *314* (1), 34-41.
114. Ording-Wenker, E. C. M.; van der Plas, M.; Siegler, M. A.; Bonnet, S.; Bickelhaupt, F. M.; Fonseca Guerra, C.; Bouwman, E., Thermodynamics of the CuII μ -Thiolate and CuI Disulfide Equilibrium: A Combined Experimental and Theoretical Study. *Inorg. Chem.* **2014**, *53* (16), 8494-8504.
115. Laurent, S.; Forge, D.; Port, M.; Roch, A.; Robic, C.; Vander Elst, L.; Muller, R. N., Magnetic Iron Oxide Nanoparticles: Synthesis, Stabilization, Vectorization, Physicochemical Characterizations, and Biological Applications. *Chem. Rev.* **2008**, *108* (6), 2064-2110.
116. Reddy, L. H.; Arias, J. L.; Nicolas, J.; Couvreur, P., Magnetic Nanoparticles: Design and Characterization, Toxicity and Biocompatibility, Pharmaceutical and Biomedical Applications. *Chem. Rev.* **2012**.
117. Ling, D.; Lee, N.; Hyeon, T., Chemical Synthesis and Assembly of Uniformly Sized Iron Oxide Nanoparticles for Medical Applications. *Acc. Chem. Res.* **2015**, *48* (5), 1276-1285.

118. Mahmoudi, M.; Hofmann, H.; Rothen-Rutishauser, B.; Petri-Fink, A., Assessing the In Vitro and In Vivo Toxicity of Superparamagnetic Iron Oxide Nanoparticles. *Chem. Rev.* **2011**, *112* (4), 2323-2338.
119. Lu, A.-H.; Salabas, E. L.; Schüth, F., Magnetic Nanoparticles: Synthesis, Protection, Functionalization, and Application. *Angew. Chem. Int. Ed.* **2007**, *46* (8), 1222-1244.
120. Ghosh Chaudhuri, R.; Paria, S., Core/Shell Nanoparticles: Classes, Properties, Synthesis Mechanisms, Characterization, and Applications. *Chem. Rev.* **2011**, *112* (4), 2373-2433.
121. Keller, A. A.; Wang, H.; Zhou, D.; Lenihan, H. S.; Cherr, G.; Cardinale, B. J.; Miller, R.; Ji, Z., Stability and Aggregation of Metal Oxide Nanoparticles in Natural Aqueous Matrices. *Environ. Sci. Technol.* **2010**, *44* (6), 1962-1967.
122. Panda, R. N.; Gajbhiye, N. S.; Balaji, G., Magnetic properties of interacting single domain Fe₃O₄ particles. *J. Alloys Compd.* **2001**, *326* (1-2), 50-53.
123. Gong, W.; Li, H.; Zhao, Z.; Chen, J., Ultrafine particles of Fe, Co, and Ni ferromagnetic metals. *J. Appl. Phys.* **1991**, *69* (8), 5119-5121.
124. Berkowitz, A. E.; Schuele, W. J.; Flanders, P. J., Influence of Crystallite Size on the Magnetic Properties of Acicular γ -Fe₂O₃ Particles. *J. Appl. Phys.* **1968**, *39* (2), 1261-1263.
125. Tang, Z. X.; Sorensen, C. M.; Klabunde, K. J.; Hadjipanayis, G. C., Size-dependent Curie temperature in nanoscale particles. *Phys. Rev. Lett.* **1991**, *67* (25), 3602-3605.

126. Rajendran, M.; Pullar, R. C.; Bhattacharya, A. K.; Das, D.; Chintalapudi, S. N.; Majumdar, C. K., Magnetic properties of nanocrystalline CoFe_2O_4 powders prepared at room temperature: variation with crystallite size. *J. Magn. Magn. Mater.* **2001**, *232* (1–2), 71-83.
127. Mahdavi, M.; Ahmad, M.; Haron, M.; Namvar, F.; Nadi, B.; Rahman, M.; Amin, J., Synthesis, Surface Modification and Characterisation of Biocompatible Magnetic Iron Oxide Nanoparticles for Biomedical Applications. *Molecules.* **2013**, *18* (7), 7533.
128. Yang, D.; Hu, J.; Fu, S., Controlled Synthesis of Magnetite–Silica Nanocomposites via a Seeded Sol–Gel Approach. *J. Phys. Chem. C.* **2009**, *113* (18), 7646-7651.
129. Milonjić, S. K.; Kopečni, M. M.; Ilić, Z. E., The point of zero charge and adsorption properties of natural magnetite. *J. Radioanal. Chem.* **1983**, *78* (1), 15-24.
130. Wang, P.; Keller, A. A., Natural and Engineered Nano and Colloidal Transport: Role of Zeta Potential in Prediction of Particle Deposition. *Langmuir* **2009**, *25* (12), 6856-6862.
131. Chapter 3 The surface chemistry of silica. In *Stud. Surf. Sci. Catal.*, E.F. Vansant, P. V. D. V.; Vrancken, K. C., Eds. Elsevier: 1995; Vol. 93, 59-77.
132. Rahman, I. A.; Vejayakumaran, P.; Sipaut, C. S.; Ismail, J.; Chee, C. K., Size-dependent physicochemical and optical properties of silica nanoparticles. *Mater. Chem. Phys.* **2009**, *114* (1), 328-332.
133. Cheng, Y.; Tan, R.; Wang, W.; Guo, Y.; Cui, P.; Song, W., Controllable synthesis and magnetic properties of Fe_3O_4 and $\text{Fe}_3\text{O}_4@ \text{SiO}_2$ microspheres. *J. Mater. Sci.* **2010**, *45* (19), 5347-5352.

134. Ek, S.; Root, A.; Peussa, M.; Niinistö, L., Determination of the hydroxyl group content in silica by thermogravimetry and a comparison with ^1H MAS NMR results. *Thermochim. Acta* **2001**, 379 (1–2), 201-212.
135. Li, S.; Wan, Q.; Qin, Z.; Fu, Y.; Gu, Y., Understanding Stöber Silica's Pore Characteristics Measured by Gas Adsorption. *Langmuir* **2015**, 31 (2), 824-832.
136. Sindorf, D. W.; Maciel, G. E., Silicon-29 nuclear magnetic resonance study of hydroxyl sites on dehydrated silica gel surfaces, using silylation as a probe. *J. Phys. Chem.* **1983**, 87 (26), 5516-5521.
137. Qiao, B.; Wang, T.-J.; Gao, H.; Jin, Y., High density silanization of nano-silica particles using γ -aminopropyltriethoxysilane (APTES). *Appl. Surf. Sci.* **2015**, 351, 646-654.
138. Pasternack, R. M.; Rivillon Amy, S.; Chabal, Y. J., Attachment of 3-(Aminopropyl)triethoxysilane on Silicon Oxide Surfaces: Dependence on Solution Temperature. *Langmuir* **2008**, 24 (22), 12963-12971.
139. Chapter 9 Modification with silicon compounds: mechanistic studies. In *Stud. Surf. Sci. Catal.*, E.F. Vansant, P. V. D. V.; Vrancken, K. C., Eds. Elsevier: 1995; Vol. Volume 93, pp 193-297.
140. Parks, G. A., The Isoelectric Points of Solid Oxides, Solid Hydroxides, and Aqueous Hydroxo Complex Systems. *Chem. Rev.* **1965**, 65 (2), 177-198.
141. Zhu, M.; Lerum, M. Z.; Chen, W., How To Prepare Reproducible, Homogeneous, and Hydrolytically Stable Aminosilane-Derived Layers on Silica. *Langmuir* **2011**, 28 (1), 416-423.

142. Deschner, T.; Liang, Y.; Anwander, R., Silylation Efficiency of Chorosilanes, Alkoxysilanes, and Monosilazanes on Periodic Mesoporous Silica. *J. Phys. Chem. C* **2010**, *114* (51), 22603-22609.
143. Sangvanich, T.; Morry, J.; Fox, C.; Ngamcherdtrakul, W.; Goodyear, S.; Castro, D.; Fryxell, G. E.; Addleman, R. S.; Summers, A. O.; Yantasee, W., Novel Oral Detoxification of Mercury, Cadmium, And Lead with Thiol-Modified Nanoporous Silica. *ACS Appl. Mater. Inter.* **2014**, *6* (8), 5483-5493.
144. Yuan, Y.; Rende, D.; Altan, C. L.; Bucak, S.; Ozisik, R.; Borca-Tasciuc, D.-A., Effect of Surface Modification on Magnetization of Iron Oxide Nanoparticle Colloids. *Langmuir* **2012**, *28* (36), 13051-13059.
145. Kokate, M.; Garadkar, K.; Gole, A., One pot synthesis of magnetite-silica nanocomposites: applications as tags, entrapment matrix and in water purification. *J. Mater. Chem. A* **2013**, *1* (6), 2022-2029.
146. Rebodos, R. L.; Vikesland, P. J., Effects of Oxidation on the Magnetization of Nanoparticulate Magnetite. *Langmuir* **2010**, *26* (22), 16745-16753.
147. Morel, A.-L.; Nikitenko, S. I.; Gionnet, K.; Wattiaux, A.; Lai-Kee-Him, J.; Labrugere, C.; Chevalier, B.; Deleris, G.; Petibois, C.; Brisson, A.; Simonoff, M., Sonochemical Approach to the Synthesis of Fe₃O₄@SiO₂ Core–Shell Nanoparticles with Tunable Properties. *ACS Nano* **2008**, *2* (5), 847-856.
148. Tombacz, E. M., Z. S.; Horvat, E. Illes, Magnetite In Aqueous Medium: Coating Its Surface and Surface Coated With It. *Rom. Rep. Phys.* **2006**, *58* (3), 281-286.
149. Gajbhiye, N. S.; Prasad, S., Thermal decomposition of hexahydrated nickel iron citrate. *Thermochim. Acta* **1996**, *285* (2), 325-336.

150. Lee, J.; Lee, Y.; Youn, J. K.; Na, H. B.; Yu, T.; Kim, H.; Lee, S.-M.; Koo, Y.-M.; Kwak, J. H.; Park, H. G.; Chang, H. N.; Hwang, M.; Park, J.-G.; Kim, J.; Hyeon, T., Simple Synthesis of Functionalized Superparamagnetic Magnetite/Silica Core/Shell Nanoparticles and their Application as Magnetically Separable High-Performance Biocatalysts. *Small* **2008**, *4* (1), 143-152.
151. Lin, Y.-S.; Haynes, C. L., Impacts of Mesoporous Silica Nanoparticle Size, Pore Ordering, and Pore Integrity on Hemolytic Activity. *J. Am. Chem. Soc.* **2010**, *132* (13), 4834-4842.
152. Deng, Y.; Qi, D.; Deng, C.; Zhang, X.; Zhao, D., Superparamagnetic High-Magnetization Microspheres with an Fe₃O₄@SiO₂ Core and Perpendicularly Aligned Mesoporous SiO₂ Shell for Removal of Microcystins. *J. Am. Chem. Soc.* **2007**, *130* (1), 28-29.
153. Varganici, C.-D.; Durdureanu-Angheluta, A.; Rosu, D.; Pinteala, M.; Simionescu, B. C., Thermal degradation of magnetite nanoparticles with hydrophilic shell. *J. Anal. Appl. Pyrolysis* **2012**, *96* (0), 63-68.
154. Bahde, R. J.; Appella, D. H.; Trenkle, W. C., A one-pot preparation of N-2-mercaptobenzoyl-amino amides. *Tetrahedron Lett.* **2011**, *52* (32), 4103-4105.
155. Chouhan, R. S.; Qureshi, A.; Niazi, J. H., Quantum dot conjugated *S. cerevisiae* as smart nanotoxicity indicators for screening the toxicity of nanomaterials. *J. Mater. Chem. B.* **2014**, *2* (23), 3618-3625.
156. Kato, M.; Toshima, K.; Matsumura, S., Direct Enzymatic Synthesis of a Polyester with Free Pendant Mercapto Groups. *Biomacromolecules* **2009**, *10* (2), 366-373.

157. Nobs, L.; Buchegger, F.; Gurny, R.; Allémann, E., Surface modification of poly(lactic acid) nanoparticles by covalent attachment of thiol groups by means of three methods. *Int. J. Pharm.* **2003**, *250* (2), 327-337.
158. Wu, W.; He, Q.; Jiang, C., Magnetic Iron Oxide Nanoparticles: Synthesis and Surface Functionalization Strategies. *Nano. Res. Lett.* **2008**, *3* (11), 397.
159. Gradmann, U., Surface magnetism. *J. Magn. Magn. Mater.* **1991**, *100* (1), 481-496.
160. Larumbe, S.; Gómez-Polo, C.; Pérez-Landazábal, J. I.; Pastor, J. M., Effect of a SiO₂ coating on the magnetic properties of Fe₃O₄ nanoparticles. *J. Phys.: Condens. Matter* **2012**, *24* (26), 266007.
161. Mazo-Zuluaga, J.; Restrepo, J.; Mejía-López, J., Effect of surface anisotropy on the magnetic properties of magnetite nanoparticles: A Heisenberg–Monte Carlo study. *J. Appl. Phys.* **2008**, *103* (11), 113906.
162. Xu, H.; Tong, N.; Cui, L.; Lu, Y.; Gu, H., Preparation of hydrophilic magnetic nanospheres with high saturation magnetization. *J. Magn. Magn. Mater.* **2007**, *311* (1), 125-130.
163. Zeng, L., A method for preparing silica-containing iron(III) oxide adsorbents for arsenic removal. *Water Res.* **2003**, *37* (18), 4351-4358.
164. Wang, Y.; Morin, G.; Ona-Nguema, G.; Juillot, F.; Calas, G.; Brown, G. E., Distinctive Arsenic(V) Trapping Modes by Magnetite Nanoparticles Induced by Different Sorption Processes. *Environ. Sci. Technol.* **2011**, *45* (17), 7258-7266.
165. Liu, C.-H.; Chuang, Y.-H.; Chen, T.-Y.; Tian, Y.; Li, H.; Wang, M.-K.; Zhang, W., Mechanism of Arsenic Adsorption on Magnetite Nanoparticles from Water:

- Thermodynamic and Spectroscopic Studies. *Environ. Sci. Technol.* **2015**, *49* (13), 7726-7734.
166. Kabengi, N. J.; Daroub, S. H.; Rhue, R. D., Energetics of arsenate sorption on amorphous aluminum hydroxides studied using flow adsorption calorimetry. *J. Colloid Interf. Sci.* **2006**, *297* (1), 86-94.
167. Rhue, R. D.; Appel, C.; Kabengi, N., Measuring Surface Chemical Properties of Soil Using Flow Calorimetry 1. *Soil Sci.* **2002**, *167* (12), 782-790.
168. Spuches, A. M.; Kruszyna, H. G.; Rich, A. M.; Wilcox, D. E., Thermodynamics of the As(III)-Thiol Interaction: Arsenite and Monomethylarsenite Complexes with Glutathione, Dihydrolipoic Acid, and Other Thiol Ligands. *Inorg. Chem.* **2005**, *44* (8), 2964-2972.
169. Patwardhan, S. V.; Emami, F. S.; Berry, R. J.; Jones, S. E.; Naik, R. R.; Deschaume, O.; Heinz, H.; Perry, C. C., Chemistry of Aqueous Silica Nanoparticle Surfaces and the Mechanism of Selective Peptide Adsorption. *J. Am. Chem. Soc.* **2012**, *134* (14), 6244-6256.
170. Slavov, S. V.; Chuang, K. T.; Sanger, A. R., Modification of the Surfaces of Silica, Silica-Alumina, and Aluminum Silicate with Chlorotrimethylsilane. *J. Phys. Chem.* **1996**, *100* (40), 16285-16292.
171. Staley, B. F.; Barlaz, M. A., Composition of Municipal Solid Waste in the United States and Implications for Carbon Sequestration and Methane Yield. *J. Environ. Eng.* **2009**, *135* (10), 901-909.

172. Wang, X.; Nagpure, A. S.; DeCarolis, J. F.; Barlaz, M. A., Using Observed Data To Improve Estimated Methane Collection from Select U.S. Landfills. *Environ. Sci. Technol.* **2013**, *47* (7), 3251-3257.
173. Wang, X.; Nagpure, A. S.; DeCarolis, J. F.; Barlaz, M. A., Characterization of Uncertainty in Estimation of Methane Collection from Select U.S. Landfills. *Environ. Sci. Technol.* **2015**, *49* (3), 1545-1551.
174. Clancy, T. M.; Hayes, K. F.; Raskin, L., Arsenic Waste Management: A Critical Review of Testing and Disposal of Arsenic-Bearing Solid Wastes Generated during Arsenic Removal from Drinking Water. *Environ. Sci. Technol.* **2013**, *47* (19), 10799-10812.
175. Webster, T. M.; Reddy, R. R.; Tan, J. Y.; Van Nostrand, J. D.; Zhou, J.; Hayes, K. F.; Raskin, L., Anaerobic Disposal of Arsenic-Bearing Wastes Results in Low Microbially Mediated Arsenic Volatilization. *Environ. Sci. Technol.* **2016**, *50* (20), 10951-10959.
176. Janssen, A. J.; Ruitenber, R.; Buisman, C. J., Industrial applications of new sulphur biotechnology. *Water Sci. Technol.* **2001**, *44* (8), 85-90.
177. Phan, T. T.; Capo, R. C.; Stewart, B. W.; Graney, J. R.; Johnson, J. D.; Sharma, S.; Toro, J., Trace metal distribution and mobility in drill cuttings and produced waters from Marcellus Shale gas extraction: Uranium, arsenic, barium. *Appl. Geochem.* **2015**, *60*, 89-103.
178. Powell, J. T.; Jain, P.; Smith, J. L.; Townsend, T. G.; Tolaymat, T. M., Does Disposing of Construction and Demolition Debris in Unlined Landfills Impact

Groundwater Quality? Evidence from 91 Landfill Sites in Florida. *Environ. Sci. Technol.* **2015**, *49* (15), 9029-9036.

179. Parris, G. E.; Brinckman, F. E., Reactions which relate to environmental mobility of arsenic and antimony. II. Oxidation of trimethylarsine and trimethylstibine. *Environ. Sci. Technol.* **1976**, *10* (12), 1128-1134.

180. Komárek, M.; Koretsky, C. M.; Stephen, K. J.; Alessi, D. S.; Chrastný, V., Competitive Adsorption of Cd(II), Cr(VI), and Pb(II) onto Nanomaghemite: A Spectroscopic and Modeling Approach. *Environ. Sci. Technol.* **2015**, *49* (21), 12851-12859.

181. Bixner, O.; Lassenberger, A.; Baurecht, D.; Reimhult, E., Complete Exchange of the Hydrophobic Dispersant Shell on Monodisperse Superparamagnetic Iron Oxide Nanoparticles. *Langmuir* **2015**, *31* (33), 9198-9204.

182. Chowdhury, S. R.; Yanful, E. K., Arsenic and chromium removal by mixed magnetite–maghemite nanoparticles and the effect of phosphate on removal. *J. Environ. Manage.* **2010**, *91* (11), 2238-2247.

Vita

Education:

BS- Cum Laude, Chemistry, Virginia Commonwealth University (Richmond, VA), 2010.

Experience:

2010-2017: Dissertation Research, UK

- Collaborated, designed, and increased arsenic removal from methane gas production at an active landfill site.
- Measured the utility of magnetic separations with hybrid composite materials with high affinity for aqueous arsenic.
- Scaled up the design and fabrication of magnetic iron oxide nanoparticles coated with thin monodisperse layers of silica.
- Grafted linkers to silica substrates utilized as coupling reactions for amide bond formation.
- Synthesized various organic ligands designed for selective removal of toxic metals and metalloids from aqueous solutions.
- Demonstrated safe and reliable working habits in the presence of toxic and pyrophoric materials.
- Helped develop and design a series of upper level undergraduate laboratory experiments based on dissertation research.

2009-2010: Undergraduate Research VCU

- Fabricated polycarbonate microchips and circuits coated with small molecules and proteins to measure microfluidic streaming potentials.
- Synthesized various organic molecules, metal-organic-frameworks, and precious metal nanoparticles.
- Measured antibacterial properties with silver nanoparticles loaded on metal-organic-frameworks.
- Explored catalyst efficiency for certain epoxidations, reductions, and Suzuki coupling reactions with gold nanoclusters loaded on metal-organic-frameworks.

Research Awards

University of Kentucky Graduate School Steckler Fellowship 2016

Kentucky Water Resources Research Grant 2011

National Science Foundation(REU) summer research grant Summer 2009

VCU Chemistry Department KAPP Scholarship Fall 2009

VCU Dean's List: 2007- 2010

Publications

Walrod, J. H.; Atwood, D. A. Rare Earth Heterogeneous Catalysis. *Rare Earth Elements: Fundamentals and Applications*. Wiley: New York, 2012; pp 385-389.

Walrod, J. H.; Atwood, D. A. Rare Earth Metal Organic Frameworks. *Rare Earth Elements: Fundamentals and Applications*. Wiley: New York, 2012; pp 475-481.

Walrod, J. H.; Atwood, D. A. Aqueous Toxic Metal Removal with Functionalized Magnetic Nanoparticles. *Handbook of Functional Nanomaterials - Properties and Commercialization*, Nova Science Publishers, LTD: New York, 2013; Vol. 4.

Burriss, D.; Zou, W.; Cremer, D.; Walrod, J. H.; Atwood, D. A. Removal of Selenite from Water Using a Synthetic Dithiol: Experimental and Quantum Chemical Investigation. *Inorg. Chem.* 2014, 53 (8), 4010-4021.

Walrod, J. H.; Beck, G. E.; Burriss, D.; Blue, L.; Atwood, D. A. Arsenic Mobility in Karnak Soils after Multi-Year Application of Poultry Litter Containing Roxarsone. *Main Group Chem.* 2016, 15 (4), 365-373.

Planned Publications from Dissertation Research

Walrod, J. H.; Burriss, D.; Atwood, D. A. Use of Superparamagnetic Nanoparticles to Remove Arsenite from Water. TBA.

Walrod, J. H.; Burriss, D.; Atwood, D. A. Thermodynamics of Arsenite Removal from Water with a Solid-Supported Dithiolate. TBA.

Walrod, J. H.; Burriss, D.; Atwood, D. A. The Challenges of Arsenic Removal from Biogas Production. TBA.

Burriss, D.; Walrod, J. H.; Atwood, D. A. A Rare Crystal Structure with Cadmium(II)-Cysteine Covalent Bonding. TBA.

Butala, R.; Parkin, S.; Walrod, J. H.; Atwood, D. A. Salen Supported Aluminum Phosphates. TBA